Advanced Manufacturing and Processing of Ceramics and Ceramic Composites

by

Mohammadreza Mahmoudi

A Dissertation Presented in Partial Fulfillment
of the Requirements for the Degree
Doctor of Philosophy

Approved October 2022 by the
Graduate Supervisory Committee:

Majid Minary-Jolandan, Chair
Jagannathan Rajagopalan
Corson L. Cramer
Wonmo Kang
Dhruv Bhate

ARIZONA STATE UNIVERSITY

December 2022

ABSTRACT

Achieving a viable process for advanced manufacturing of ceramics and metal-ceramic composites is a sought-after goal in a wide range of fields including electronics and sensors for harsh environments, microelectromechanical devices, energy storage materials, and structural materials, among others. In this dissertation, the processing, and manufacturing of ceramics and ceramic composites are addressed, specifically, a process for three-dimensional (3D) printing of polymer-derived ceramics (PDC), and a process for low-cost manufacturing as well as healing of metal-ceramic composites is demonstrated.

Three-dimensional printing of ceramics is enabled by dispensing the preceramic polymer at the tip of a moving nozzle into a gel that can reversibly switch between fluid and solid states, and subsequently thermally cross-linking the entire printed part "at once" while still inside the same gel was demonstrated. The solid gel converts to fluid at the tip of the moving nozzle, allowing the polymer solution to be dispensed and quickly returns to a solid state to maintain the geometry of the printed polymer both during printing and the subsequent high-temperature (160 °C) cross-linking. After retrieving the cross-linked part from the gel, the green body is converted to ceramic by high-temperature pyrolysis. This scalable process opens new opportunities for low-cost and high-speed production of complex three-dimensional ceramic parts and will be widely used for high-temperature and corrosive environment applications, including electronics and sensors, microelectromechanical systems, energy, and structural applications.

Metal-ceramic composites are technologically significant as structural and functional materials and are among the most expensive materials to manufacture and repair. Hence, technologies for self-healing metal-ceramic composites are important. Here, a concept to

fabricate and heal co-continuous metal-ceramic composites at room temperature were demonstrated. The composites were fabricated by infiltration of metal (here Copper) into a porous alumina preform (fabricated by freeze-casting) through electroplating; a low-temperature and low-cost process for the fabrication of such composites. Additionally, the same electroplating process was demonstrated for healing damages such as grooves and cracks in the original composite, such that the healed composite recovered its strength by more than 80%. Such technology may be expanded toward fully autonomous self-healing structures.

To my mom and dad

ACKNOWLEDGMENTS

First of all, I would like to express my sincere gratitude to my advisor, Dr. Majid Minary for his investing in me and letting me be a part of his research team, for his endless support, invaluable guidance, and always giving me the insight about the big picture. His passion, motivation, insightful ideas were the driving force for my research and his hands-on advising style greatly helped me overcome the challenges. I learned a lot from Dr. Minary and owe him for giving me the opportunity.

I was very fortunate to have Dr. Jagannathan Rajagopalan, Dr. Corson Cramer, Dr. Wonmo Kang, and Dr. Dhruv Bhate on my graduate committee. Their valuable suggestions and advice strengthened this work considerably. Particularly, I would like to thank Dr. Cramer and his research team in Oak Ridge National Laboratory because of their valuable contribution and constructive comments in my research.

In addition, I would like thank individuals who supported my graduate studies. My colleagues Dr. Mohammad Naraghi (TAMU), Dr. Fatemeh Hassanipour (UTD), Dr. Diana Alatalo, Dr. Salvador Moreno, Dr. Chao Wang, Dr. Reza Morsali, Scott Burlison, Amirhossein Shafieizad, Moein Khakzad, Saman Ebrahimibasabi, Ashley Myles, Faisal Riyad, Eyring Materials Center particularly Sisouk Phrasavath and all UTD cleanroom especially Alexandra Joshi .

My graduate studies would not have been possible without the endless support from my family. For almost four years, my parents put up with my absence, and I wish I could have been there for them every moment they needed me. There are not enough words of gratitude to thank them, and I will always be indebted to them. My mother's unending affection has

always been a sustaining force for our family particularly when my dad works abroad. My father has taught me so much. He gave me the life that every child deserves and encouraged me throughout my lifetime. His insightful guidance put me in the right direction in life that I am very grateful for. He worked so hard to send me to the US for graduate studies, which means a world to me. I am grateful to have a lovely sister, Parisa, for her constant care and support. Her voice on the phone always motivated me for the past years. Going away and being apart from family has made me appreciate that they are the most important people in my life, and I love them more than anything. I would like to thank them, and I promise that I will work hard to make them proud.

TABLE OF CONTENTS

LIST OF TABLES

Table Page

LIST OF FIGURES

Figure Page

Figure Page

Figure Page

Figure Page

Figure Page

1 INTRODUCTION

1.1 Embedded 3D Printing of Ceramics Using Polymer-Derived SiOC Ceramics

Scientists across several fields including electronics and sensors for harsh environments, microelectromechanical devices, energy storage materials, and structural materials are interested in a viable process for three-dimensional (3D) printing of ceramics. This is because of several factors: the traditional method of ceramic manufacturing based on powder consolidation and sintering is costly, casting and machining ceramics is nontrivial as opposed to metals and polymers;[1], [2] additionally, the extremely high melting point of most ceramics, in addition to their low laser absorption, renders available additive manufacturing (AM) technologies for metals nonapplicable to or not suitable for ceramics.

Various methods for AM of ceramics have been reported such as photolithography, binder jetting, and laser sintering. The photolithography process involves selective curing of a photosensitive resin containing ceramic particles [3], [4]. In the binder jetting process, a liquid binder agent is selectively deposited onto ceramic particles [5]. In the laser sintering process, ceramic powder is selectively fused using a laser beam [6], [7]. These processes are all layer-by-layer, powder-based, and face several challenges such as porosity after removal of the binder or resin, which makes the consolidation step to achieve a dense 3D-printed part difficult. Most ceramics have low laser absorption, which makes laser-based processes challenging. In addition, laser-based processes generate a large thermal gradient in the 3D-printed part, which is the driving force for crack formation. Porosity and cracks in 3D-printed ceramics result in low strength. These processes are often slow and require a binder removal post processing step. Free- form extrusion of ceramic particle-based slurries is another method

for AM of ceramics [8]. This process prints a composite of a binder and ceramic particles and requires binder removal post-processing, which often leaves behind a porous structure. The polymer-derived ceramics (PDCs), a class of ceramics that are obtained by pyrolysis of polymer precursors [9] lend themselves to AM processes. This is because in their polymer state they are suitable for shaping such as printing, and the subsequent cross-linking locks the printed geometry [10]–[12]. PDCs were introduced in the 1960s and include SiC, SiOC, Si_3N_4, BN, AlN, SiCN, BCN, among others. PDCs are mostly used for the infiltration of ceramic matrix composites and ceramic fiber synthesis. In addition, their electrical conductivity, luminescence, and piezoresistivity make them attractive for functional applications [13]. By having Si-rich and C-rich nanosized domains, PDCs are stable against creep, oxidation, crystallization, or phase separation up to 1500 °C or higher temperature . The pyrolysis temperature of PDCs is in the range of 1000−1300 °C, which is lower than temperatures (>1600 °C) typically used in classic ceramic powder-based sintering.

Layer-by-layer, selective curing of a photosensitive slurry via a dynamic mask exposure was reported for AM of dense alumina ceramics by Schwentenwein et al. [14]. This process uses a photocurable ceramic suspension comprises high-purity alumina powder dispersed in a light-sensitive organic matrix. The organic matrix consists of a photoinitiator, monomers based on methacrylate chemistry, and additives. After the debinding and sintering process, the printed parts showed a density corresponding to 99.3% of the theoretical density of alumina, which is an indication of excellent densification. In 2015, Zanchetta et al. reported layer-by-layer stereolithography of SiOC ceramic microcomponents using an engineered photosensitive methyl-silsesquioxane preceramic polymer [13]. This report was the first direct fabrication of 3D high- performance ceramics from preceramic polysiloxanes with high

ceramic yield. The engineered preceramic precursor started from a commercially available silicone (SILRES MK) and an organically modified silicon alkoxide 3-(trimethoxysilyl) propyl methacrylate. In 2015, Eckel et al. reported AM of PDCs via stereolithography (SLA) and self-propagating photopolymerization techniques [15]. Ultraviolet (UV)-active preceramic monomers were obtained by the incorporation of UV-sensitive side groups (photoinitiators) to the backbone of the precursor polymer. Cross-linked polymer patterns were generated by scanning using a UV beam, which were subsequently postcured by thermal treatment or additional UV exposure. The printed and cured polymer was pyrolyzed to obtain virtually pore-free solid ceramic parts. The unpolymerized resin was recycled and reused. These processes based on photosensitive slurry or UV- sensitive resin require specialized chemistry. Additionally, SLA is rather slow since at each scan 30−100 μm slices are built. The ridges generated from the layer-by-layer scanning process on the surface of the printed ceramic part are surface flaws and may result in stress concentrations, which is detrimental for ceramics given their low fracture toughness. On the other hand, self-propagating photopolymerization is limited to structures with linear features extending from the exposure surface (such as lattices and honeycombs). Recently, 3D nanofabrication of SiOC ceramic structures using two-photon lithography (2PL) with an engineered printing configuration by starting from a selected preceramic formulation was demonstrated to achieve 3D complex architectures with a size on the order of 100 μm in the z-direction, with 450 nm resolution [16].

Here, a new approach for high-speed 3D printing of PDCs that does not require UV or photocuring or rheology modifiers and results in binder-free printed parts is demonstrated. In this process, the 3D-printed precursor ceramic polymer is thermally cured in a single step at the end of the printing process, as opposed to layer-by-layer curing. In recent studies, 3D

printing of polymers with the aid of a viscoplastic liquid sacrificial support has emerged as a viable method to generate spatially structured soft matters [17]–[19]. This method relies on controllable interactions between two liquids, the precursor of the main structure (such as a resin) and the liquid support bath. While the former can be considered as a Newtonian fluid, the latter is a so-called "yield stress fluid," which switches reversibly from a semisolid to a liquid when subjected to sufficiently high shear stress to allow for extrusion of the liquid precursor and retains the printed part shape in the wake of the nozzle when shear stress is removed. In this printing process, the shear stress is provided by the nozzle motion. The liquid precursor is then cured inside the support bath and retrieved for subsequent processing steps. While printing in yield stress fluids has been used for biological systems and soft materials that can be cured at low temperatures,[17]–[19] PDCs require thermally induced curing at elevated temperatures (>120 °C) and are much more sensitive to surface defects compared to biological materials. AM of SiOC (silicon oxycarbide) ceramics in a yield stress fluid support bath that is based on mineral oil and silica nanoparticles, which makes it suitable for high-temperature curing required for SiOC and can further be applied to other PDC types including SiC, SiCN, and Si_3N_4 is presented.

1.2 Investigation of the Process Parameters for In Bath Print and Cure (IBPC) Process

The three-dimensional printing (3D printing) of polymeric materials has disrupted how complex and customized structures are built [20]–[28]. The ease in the processing of thermoplastic polymers, which involves melting and depositing molten plastics, has resulted in widely available low-cost 3D printers for the general public. However, thermoplastics suffer from several disadvantages: the temperature gradient between the previous layer and the deposited one results in thermal gradient and residual stress, which leads to warping, and the

interlayer interface in thermoplastics relies on the partial diffusion of polymer chains, which results in weak interfaces. On the other hand, thermosetting (TS) polymers do not require thermal energy input to process and can be processed at room temperature (or slightly elevated temperature), eliminating the thermal gradient issue; the interlayer interface in thermosetting polymers is based on cross-linking, which results in stronger interfaces. In addition, TS polymers are generally cheaper than thermoplastics. Furthermore, the superior thermal stability and mechanical properties and excellent chemical resistance make TS polymers and their composites desirable for aerospace, energy, and automotive applications [29], [30]. Except for highly reactive thermosets, [29], [31] the majority of TS polymers require several hours of high-temperature curing, which is not compatible with the requirement of 3D printing processes that the material should hold its shape for successive layers to build up. Unless cross-linked, TS polymers generally cannot retain their shape, and once cross-linked, they are not extrudable. This remains a formidable challenge for the 3D printing of TS polymers. So far, 3D printing of TS polymers has been mainly limited to photocurable processes, which require specialized resins [20], [23], [27], [32]–[34]. One solution to mediate this problem has been to use rheology modifiers or thickeners such as nanoclay and silica nanoparticles to obtain the required shear-thinning behavior for the ink for the direct ink writing (DIW) process [30], [35], [36]. However, the need for a substantial weight fraction (up to 20 wt. %) of rheology modifiers is still a limiting factor. So far, 3D printing of pure commercial TS polymers without rheology modifiers or photoinitiators has not been achieved.

A rheology-modifier- and photoinitiator-free approach to 3D printing of TS polymers, which is capable of the continuous and high-speed printing of off-the-shelf commercial TS polymers using conventional extrusion printers is demonstrated. The process is low-cost and

can print objects of several centimeters in size in a few minutes. Moreover, the cure-after-print (as opposed to layer-by-layer cross-linking) results in strong interlayers and isotropic mechanical properties (independent of the print direction). Specifically, strength, elastic modulus, strain to failure, and tensile toughness were found to be independent from the print direction. The presence of the sacrificial support bath also eliminates the need to print and remove support structures.

1.3 Processing and 3D Printing of Polymer-Derived SiCN Ceramics for High Temperature Applications

Additive manufacturing (AM) or 3D printing of ceramics has attracted considerable attention in the last decade or so. Mostly driven by the high cost of traditional ceramic manufacturing methods based on powder consolidation and sintering, as well as the nontrivial nature of ceramic machining [37], [38]. Among various methods for AM of ceramics including photolithography, binder jetting, laser sintering, and free-form extrusion of ceramic particle-based slurries,[39]–[44], AM of polymer-derived ceramics [45] is notable, since in their polymer state they are suitable for printing, and the subsequent cross-linking maintains the printed geometry in a net shape [46]–[48]. Various methods such as lithography [49]–[53] and direct extrusion in the air or a yield-stress bath [54]–[57] have been used for AM of PDCs.

A PDC is produced by pyrolysis of an organosilicon polymer at temperatures ~900°C–1400°C [58]. PDCs include SiC, BN, Si_3N_4, BCN, SiOC, SiCN, among others. Particularly, the focus in this manuscript is on the processing and 3D printing of SiCN PDC because of its broad application in many cutting-edge technologies such as bioengineering, microwave absorption devices, high-temperature sensors, structural applications, and energy storage

devices [59]–[66]. This route eliminates the need for sintering additives required in the traditional manufacturing of ceramics resulting in the creation of high oxidation and corrosion resistance, good thermal stability along good mechanical properties [45], [50]. The overall ceramic manufacturing costs are independent of design complexity rather it depends on many factors such as materials, production volume, and lead time among others. In terms of material preparation, mass production of PDCs is challenging for industrial applications, which may lead to high costs. However, for small-volume productions, the PDC route may be more economical than traditional methods. During the pyrolysis, the volatile organometallic species are released, which can drastically decrease the ceramic yield. This loss of volatile species originates from depolymerization reactions or the extraction of low molecular oligomers [67]. The crosslinking step, prior to pyrolysis, is a crucial step in the manufacturing of PDCs because of several reasons [68]. First, crosslinking increases the ceramic yield, because crosslinking prevents the loss and fragmentation of low molecular weight parts of the precursor polymer during ceramization. Second, crosslinking at low temperature (100–400°C) leads to infusible organic/inorganic networks, which prevents melting and helps retaining geometry/shape upon pyrolysis.

In particular, for polysilazanes preceramic polymers, thermal crosslinking or crosslinking using a chemical reagent (such as catalyst or peroxide) in various concentrations is used [57], [69]–[72]. Comparatively, less attention has been paid to the effects of the catalyst concentration and crosslinking duration on the ceramic yield, crosslinking temperature, and ceramic density. These factors become increasingly important in particular for the case of AM of PDCs. In the current research, the effects of the catalyst concentration and curing (crosslinking) duration on the ceramic yield, ceramic density, and the glass transition

temperature of the cured polysilazane resin was explored. The thermal behavior and crosslinking mechanisms were analyzed using differential scanning calorimetry (DSC), thermogravimetric analysis (TGA), and Fourier-Transform Infrared Spectroscopy (FTIR). Bulk PDC samples were also demonstrated using molds and the best conditions were selected for 3D printing.

1.4 Manufacturing and Self-Healing of Co-Continuous Ceramic-Metal Composites using Electrodeposition

The concept of self-healing, primarily inspired by biological materials, has been mostly studied in polymeric materials. Generally, for self-healing polymers a curing agent, catalyst, or monomers are embedded inside the polymer matrix [73], [74]. Once the crack is initiated and propagated the embedded healing material flows inside the crack and reacts with the base polymer to solidify and heal the crack. Various self-healing mechanisms such as chain re-entanglement [74], noncovalent bonding [75], and reversible chemical reactions [76] have demonstrated for polymers.

Self-healing in metals have been studied to much less extent compared to polymers. Although self-healing in metals may results in full strength recovery, it requires high energy input to heat up the material near or above the melting temperature to enable atomic diffusion [77]–[79]. For example, self-healing in metallic materials was enabled by embedding a low melting temperature metal into a high melting temperature metal. As the crack initiated and propagated inside the high melting temperature metal, by heating the component the embedded phase melts and fills the crack [80], [81]. In another work, joule heating was utilized to locally heat up the fractured sample to heal the crack [82]. Recently, room temperature and

low-cost healing of metallic components was introduced by electrochemical healing. In this process, desired metal structures were coated with a polymer layer, and after fracture, they were submerged into an electrolyte bath to deposit metal at cracked regions to heal the samples [83], [84].

Metal-ceramic composites are advanced composites that consist of a metallic matrix reinforced with materials including ceramic materials most commonly alumina and silicon carbide in continuous fiber, short fiber, whisker, and micro-platelets forms, as well as carbon fibers [85], [86]. Because of high specific strength, stiffness, and elastic modulus, in addition to remarkable fracture toughness, metal-ceramic composites are used in aircraft structures such as landing gears, high-performance and light-weight structural composites, engine components, wear-resistance parts, and cutting tools for advanced manufacturing of aerospace parts. They are also used in armors in some tanks, in high-power and high-density power electronics and multi-chip modules because of their high thermal conductivity, as well as in space systems. Currently, metal-ceramic composites are generally much more expensive than alloys and polymer matrix composites, largely due to high cost of manufacturing, and repair. As such, they are often over-designed to prevent or reduce failure possibilities, which results in an increased weight. Possibility of self-healing, hence lowering their weight, along with their low-cost manufacturing processes will substantially increase their applications. Very few publications are available on self-healing metals, and metal-ceramic composites. These materials face the challenge of high temperature requirement for healing. Additional challenges include precise chemistries for alloys, and oxidation of surfaces exposed to air. These challenges require alternative mechanisms for metal healing compared to polymers.

A concept to fabricate and heal co-continuous metal-ceramic composites at room temperature is demonstrated. The composites are fabricated by infiltration of metal (here Copper) into a porous alumina preform (fabricated by freeze-casting) through electroplating; a low-temperature and low-cost (by ~ 60-times lower cost compared to traditional molten metal infiltration) process for fabrication of such composites. Additionally, the same electroplating process is demonstrated for healing damages such as grooves and cracks in the original composite, such that the healed composite recovers its strength by more than 80%.

1.5 Scalable Manufacturing of Ceramic Sheets via Freeze Casting using a Cold Plate

Porous ceramics are promising candidates for energy storage and conversion devices, filters, catalyst support, insulators, bio-scaffolds, among others [87]. Because of their low density, high strength and toughness, thermal shock resistance, excellent high temperature stability, and thermal insulation capability, they are attractive materials [88]–[90]. They are also versatile preforms for material infiltration processes to fabricate composite materials [91]–[95].

There are several techniques to fabricate porous ceramics including replica templating [96], partial sintering [97], sacrificial templating [98], [99], and direct foaming [100], [101]. Replica templating involves the impregnation of a sponge, or polymeric scaffold using a ceramic slurry. Partial sintering is the most convenient method of fabrication of porous ceramics because it lowers either the processing temperature or pressure to increase the porosity of the ceramic. Sacrificial templating involves an appropriate inclusion of a pore former in ceramic slurry. Ice templating is another sacrificial templating technique that involves a sublimation process to remove the ice content of the frozen ceramic slurry [91], [102]–[104]. The rheological properties of the ceramic slurry play an important role in the pore

structure of the porous ceramic fabricated by ice templating. Direct foaming enables manufacturing of porous ceramics by passing a gaseous phase into the ceramic slurry. The pore structure of porous ceramics is mostly determined by the material processing and manufacturing. The pore structure directly affects the structural and functional properties of porous ceramics. The particle shape of the ceramic powder plays an important role in ceramic processing. Different particle shapes include platelets, spherical nanoparticles, whiskers, fibers, irregular shape nanopowders, among others [105], [106].

Here, freeze casting technique was used to manufacture porous ceramics. Bimodal alumina spherical nanoparticles were used to make ceramic slurry. Ceramic slurries with two size nanoparticles at different compositions were prepared and frozen using a thermoelectric cold plate. The flexural bending experiment was chosen to characterize the mechanical performance of the fabricated porous ceramics. Incorporating a smaller diameter ceramic nanoparticle into the slurry enhances the packing density, which results in better consolidation. The morphology and pore structure of the ceramics was investigated by scanning electron microscopy (SEM). Statistical analysis of the flexural strength of the ceramics were performed using two parameter Weibull analysis.

1.6 Mechanical Characterization of Intact and Healed Metal-Ceramic Composites

Metal-ceramic composite materials are technologically important because of their desirable properties such as high temperature stability, high specific strength, and remarkable fracture toughness, [107] among others. Because of their wide applications in many arears such as structural applications in landing gear of aircrafts, engine components, wear resistance parts, high power electronics [108], [109] etc., several manufacturing techniques are used to make

them. Metal-ceramic composites are perhaps among the most expensive materials to manufacture, and repair. As such, they are often over-designed to prevent or reduce failure possibilities. Existing concepts for self-healing metals such as embedding of low melting point metals require high temperature, and high energy [110]–[114]. Similarly, the concepts for healing of ceramics such as oxidation of reactive fillers require high temperature and specialized technology.

A low cost and low energy technique for healing of co-continuous metal-ceramic composites was introduced in chapter five, which works based on electrodeposition [91], [115], [116]. In this process by applying a constant current to the cathode, which is the conductive portion of the metal-ceramic composite, the copper ions reduce to solid copper on the conductive part of the damaged piece. In a similar research, pure steel wires were healed using electrochemical healing [116]. Since the wires were made of steel, the interfacial strength of the healing process was determined by tensile experiments. However, in the above study the over-deposited metal was not removed before the tensile experiment as the samples were thin wires. This could cause a variation in the sample-to-sample evaluation of the mechanical performance.

Here, the interfacial strength of the metal-ceramic composites manufactured by freeze casting of an aqueous alumina slurry is investigated followed by metal infiltration using the electrodeposition technique. To fabricate the ceramic sheets, a systematic study was performed to find a composition of alumina nanoparticles with two different diameters. Details of the study is presented in chapter five. After the fabrication of metal-ceramic composite, rectangular beams were cut out from the composite sheets. Three-point bending was chosen to extract the interfacial properties of the composite material.

.

2 THREE-DIMENSIONAL PRINTING OF CERAMICS THROUGH "CARVING" A GEL AND "FILLING IN" THE PRECURSOR POLYMER

Achieving a viable process for three-dimensional (3D) printing of ceramics is a sought-after goal in a wide range of fields including electronics and sensors for harsh environments, microelectromechanical devices, energy storage materials, and structural materials, among others. Low laser absorption of ceramic powders renders available additive manufacturing (AM) technologies for metals not suitable for ceramics. Polymer solutions that can be converted to ceramics (preceramic polymers) offer a unique opportunity to 3D-print ceramics; however, due to the low viscosity of these polymers, so far, their 3D printing has only been possible by combining them with specialized light-sensitive agents and subsequently cross-linking them layer by layer by rastering an optical beam. The slow rate, lack of scalability to large specimens, and specialized chemistry requirements of this optical process are fundamental limitations. 3D printing of ceramics enabled by dispensing the preceramic polymer at the tip of a moving nozzle into a gel that can reversibly switch between fluid and solid states, and subsequently thermally cross-linking the entire printed part "at-once" while still inside the same gel is demonstrated. The solid gel, which is composed of mineral oil and silica nanoparticles, converts to fluid at the tip of the moving nozzle, allows the polymer solution to be dispensed, and quickly returns to a solid state to maintain the geometry of the printed polymer both during printing and the subsequent high-temperature (160 °C) cross-linking. After retrieving the cross-linked part from the gel, the green body is converted to ceramic by high-temperature pyrolysis. This scalable process opens up new opportunities for low-cost and high-speed production of complex three-dimensional ceramic parts and will be

widely used for high temperature and corrosive environment applications, including electronics and sensors, microelectromechanical systems, energy, and structural applications.

2.1 Materials and Methods

2.1.1 Support Bath Preparation

The support bath was prepared by mixing 5 wt. % fumed silica with an average particle size in the range of ~200–300 nm (Sigma Aldrich) in 95 wt. % light mineral oil (VWR). The bath was hand mixed until it turned into a clear gel. The air bubbles generated by mixing in the support bath were removed by exposing the bath to 2 h vacuum followed by resting at room temperature for 24 h.

2.1.2 Preceramic Polymer Solution Preparation

A solution was prepared by mixing dicumyl peroxide (Sigma Aldrich) and toluene (Fisher Chemical) at 1:1 ratio. The solution was stirred for at least 2 min using a vortex mixer until all dicumyl peroxide particles completely dissolved in toluene. This solution was added to Polyramic SPR-036 (Starfire Systems) at 2:98 wt. % ratio. The solution was homogenously mixed using a magnetic stirrer for 5 min at 400 rpm. To prevent bubble formation during the curing process, the preceramic polymer solution was placed inside vacuum for 2 h.

2.1.3 Ceramic 3D Printing in Support Bath

Three-dimensional printing was performed using a delta-type 3D printer designed and built at UTD. The preceramic polymer solution was loaded into a syringe and injected by a NE-300 Just Infusion syringe pump. A sharp needle with an inner diameter of 0.024 inch was used as

the nozzle. The nozzle motion was controlled via custom-written script functions and trajectory files. After printing, the precursor polymer was cured thermally at ~160 °C for 2 h inside the same bath. After curing, the printed parts were readily retrieved from the bath. The parts were rinsed with running ethanol before pyrolysis. The pyrolysis process was performed using a tube furnace (ThermoScientific Lindberg/Blue M Mini-Mite) inside a nitrogen gas environment. The pyrolysis time–temperature cycle was as following: room temperature to 450 °C at 2 °C/min heating rate, 450–900 °C at 0.5 °C/min heating rate, followed by hold at 900 °C for 1 h.

2.1.4 Measurement of Rheological Properties

The rheological measurements were performed using an Anton Paar rheometer using a 50 mm cone with an apex angle of 0.5° and a 50 mm diameter bottom plate. Frequency sweeps were taken at 1% strain from 10^{-3} to 102 Hz. The yield stress of the material was determined by applying a shear rate sweep from 4×10^{-3} to 500 s^{-1}. The viscosity value for the preceramic polymer solution was obtained from the vendor (Starfire Systems).

2.1.5 Mechanical Characterization

The three-point flexural tests were performed using an MTI/Fullam SEMTester (MTI Instruments, Inc.). The span length of the beam was 9.8 mm. The displacement speed of the head was set to 0.05 mm/min. Specimen dimension was according to the ASTM standard (C1684-18). Based on the ASTM standard, the aspect ratio (length to width) of the test specimen should be more than three. For three-point bending tests, specimens were ~1 mm in diameter and ~15 mm in length.

2.1.6 DSC Analysis

The polymer-to-ceramic transformation was investigated by differential scanning calorimetry/thermal gravimetric analysis (DSC/TGA) performed using a STA449/F5 Netzsch instrument. The thermal analysis was performed from room temperature up to 1000 °C with a heating rate of 20 °C/min in a nitrogen gas environment.

2.1.7 SEM Imaging

A Zeiss Supra 40 SEM was utilized to observe the cross section of the ceramic specimens. Since a good electrical conductivity is required to obtain high-quality SEM images, a gold–palladium film was sputtered on the ceramic specimens. The composition of the pyrolyzed SiOC ceramic was measured by the EDAX material analysis system.

2.1.8 Casting

Since the precursor polymer was in the solution phase, a mold was used to prepare casting specimens. Molds were prepared by making several cylindrical holes in PTFE (poly(tetrafluoroethylene)), which can withstand high temperatures up to ~200 °C (≥ cross-linking temperature).

2.2 Results and Discussion

The schematic in Figure 2-1A shows the overall process flow, which includes printing the preceramic polymer inside the support bath at room environment, cross-linking the printed part while still inside the support bath in an oven at temperature ~160 °C, followed by retrieval of the cured specimen, and finally pyrolysis in a furnace at ~900 °C. The magnified

view of the nozzle and bath is shown in Figure 2-1B. The in-house designed printer consists of an injection system that controls the flow rate of the precursor polymer solution and a delta-type XYZ positioning system. The trajectory and nozzle translational speed are controlled by G-code.

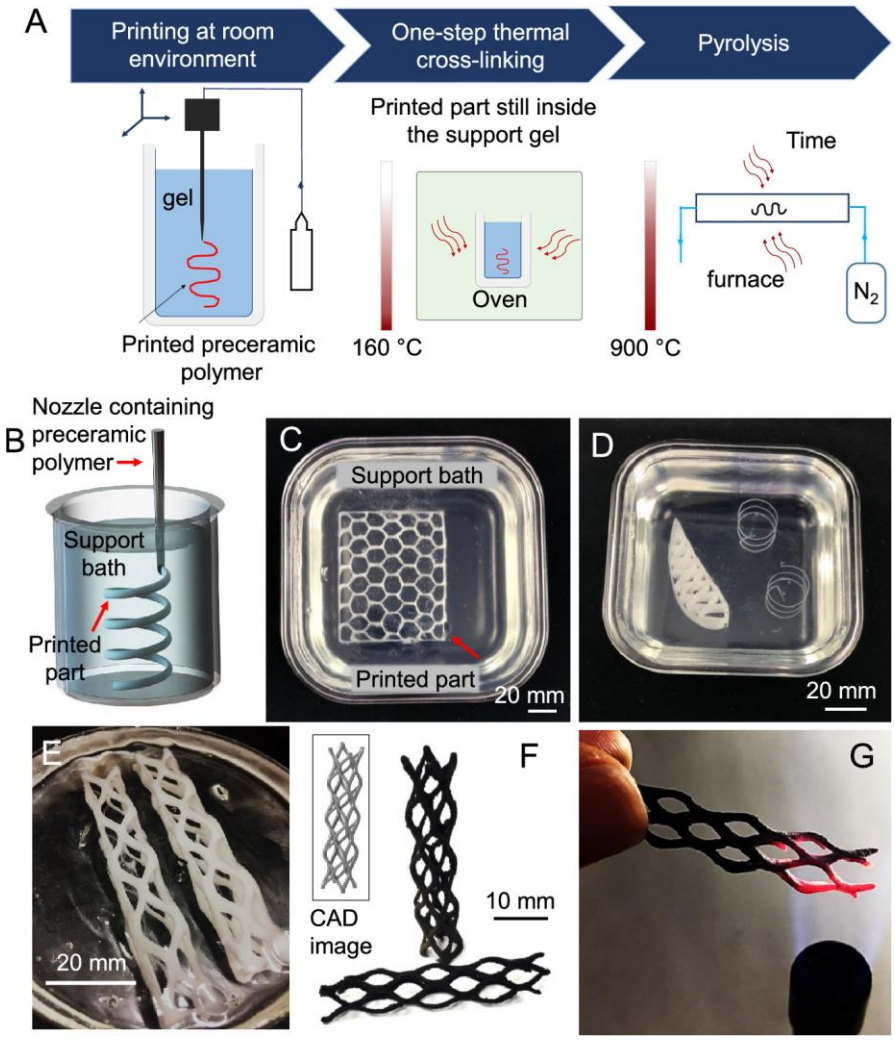

Figure 2-1 Three-dimensional-printing polymer-derived ceramics inside a support gel. (A) Process flow including printing a preceramic polymer inside the support gel and "one-step" cross-linking, while the printed part is still inside the gel, followed by retrieval of the cross-linked polymer from the gel and pyrolysis inside the furnace. (B) Schematic shows a close-up view of the polymer dispensing from the nozzle tip into the gel. (C)–(E) Photos of the several printed geometries including a honeycomb, an airfoil, two helical springs, and two truss-beams inside the gel. (F) CAD image and photo of the

truss-beam structure after pyrolysis. (G) Final printed specimen shown over a flame with T ~ 1400 °C. The change in the sample weight was ~0.6% for 2 min hold on the flame.

A yield stress support bath that can sustain its required rheological properties to support the printed geometry both at the room environment and at the temperature required for cross-linking (~160 °C) is designed. This temperature limit excludes aqueous yield stress bath due to water boiling, which will break up printed parts. Details of the materials for the bath and the preceramic polymer solution are presented in the Materials and Methods section. The support bath is composed of mineral oil and silica nanoparticles. The silica nanoparticles are rheology modifiers in this bath, given their network structure. Pure mineral oil does not have the required property to switch between the solid and fluid states, without the addition of silica nanoparticles. The capability of switching between the solid and liquid states is the key in this 3D printing process, since otherwise the printed preceramic polymer cannot be extruded, or its shape cannot be maintained. The reported bath composition was determined by an iterative process. Rheological properties of the supporting bath were tuned by changing the volume fraction of the silica nanoparticles. Increasing the volume fraction of the fumed silica in the suspension led to the formation of sol, pregel, and gel. One important consideration in this process was to avoid gravitational instability, which required the support bath to be viscous enough to keep the preceramic polymer in the desired shape and to be stable during the cross-linking at a higher temperature. The rheological properties of the bath are discussed later in the manuscript. The thermogravimetric analysis confirmed that the oil bath was stable up to ~200 °C (the boiling point of the mineral oil is ~310 °C).

Figure 2-1C−E shows photos of the several printed geometries including a honeycomb, an airfoil, two helical springs, and two truss-beams inside the gel. One advantage

of this bath is its transparency, such that the printing process can be monitored in situ. After curing, printed parts are readily retrieved from the support bath and rinsed with running ethanol for subsequent processing. Figure 2-1F shows the truss-beams after pyrolysis. During pyrolysis at ~900 °C in a nitrogen environment, polymer-to-ceramic transformation occurs. The polymer-to- ceramic transformation is accompanied by the release of volatile species (CH_4, H_2, CO_2, H_2O, and hydrocarbons) and results in shrinkage in the dimensions of the printed part, which is typical of all preceramic polymers. The linear shrinkage percentage was estimated, by image analysis of before and after pyrolysis, to be ~15%. Figure 2-1G shows a pyrolyzed part held over a flame, which demonstrates potential application of the process to print structures for the harsh environment. The temperature of the flames was ~1400 °C. The change in the sample weight was ~0.6% for 2 min hold on the flame.

Figure 2-2 shows several 3D-printed geometries after curing and pyrolysis. These samples include a helix, a hollow vase, a cone helix, a 3D grid structure, and "UTD" letters. The printing durations for these parts are provided in Table 2-1, which range from ~8 to 115 s, showing the rapid printing speed of the process. Subsequent curing and pyrolysis can be done at once for all parts.

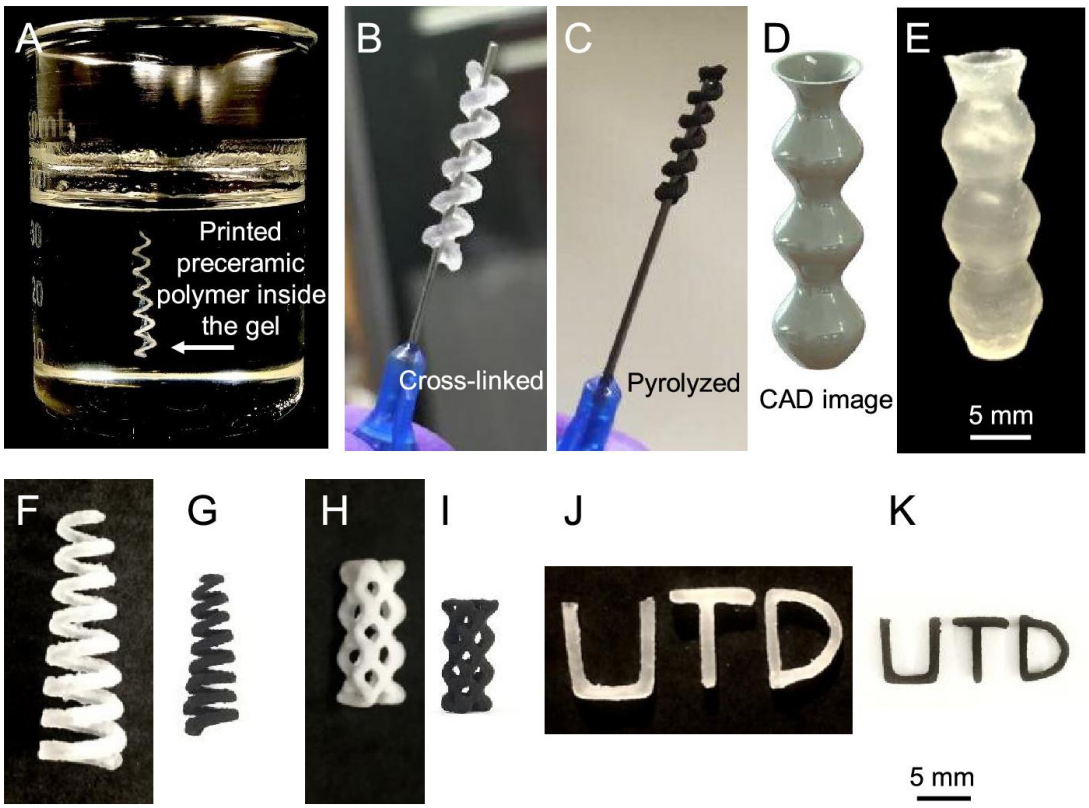

Figure 2-2 Sample 3D-printed geometries. (A–C) Helix inside the gel, after cross-linking and after pyrolysis, respectively. (D, E) CAD image and a photo of a printed hollow vase, (F)–(J) cross-linked, and (G)–(K) pyrolyzed samples. Printing durations for the parts ranged within ~8–115 s (provided in Table S1).

Table 2-1 Printing duration of selected geometries shows in Figure 2-2.

Geometry	**Printing time (s)**
Tiny helix	8
Sin pattern	115
Grid 2D	55
Cone helix	28
Vase	90
Tiny sin pattern	30
Grid 3D	55
9 pillars	50

The inset in Figure 2-3A shows the preceramic polymer in a vial. The viscosity of the polymer is ~790 cP (1 cP = 10^{-3} Pa.s). In Figure 2-3A, this viscosity is compared to other fluids such as engine oil and honey to show the rather low viscosity of the preceramic polymer. As an example, the preceramic polymer solution is more than 13 times less viscous than honey. The polymer solution used in this study does not contain any rheology modifiers or additives as opposed to all other previously reported methods for such low-viscosity polymers [13], [117]. Due to its low viscosity, it cannot be directly extruded without support, as it cannot maintain its shape. As such the two most common methods for 3D printing of preceramic polymers are using layer-by-layer photocuring and mixing with other additives and rheology modifiers to increase the viscosity. Noted that the interfacial tension and other rheological properties of the preceramic polymer and bath are important in the 3D printing process. In this work, a commercially available preceramic polymer, without changing the chemistry or composition was used. The properties of the preceramic polymer during the printing process are not controlled, and the polymer is physically extruded through the nozzle and dispensed into the bath. The support bath is shown in the inset in Figure 2-3C. It is transparent and free of any visible bubbles. When held upside down, the gel holds its shape without flowing, which shows its solid like behavior in the absence of shear stress.

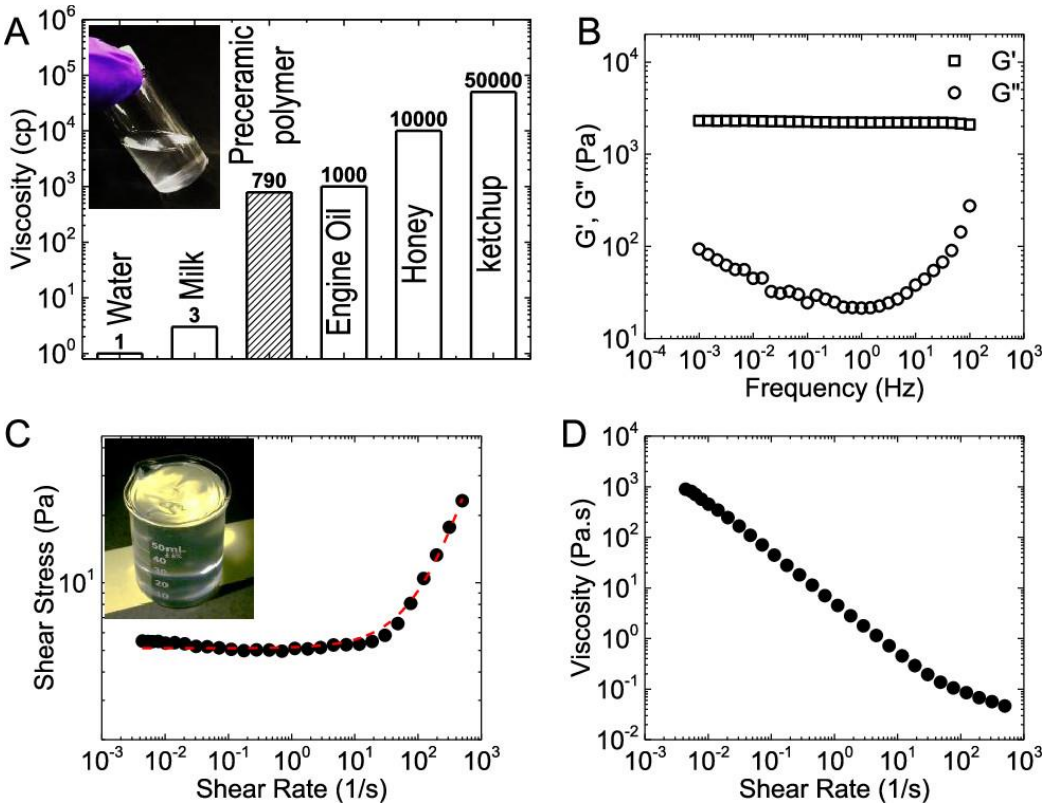

Figure 2-3 Rheological properties of the preceramic polymer and the support gel. (A) Comparison of the preceramic polymer viscosity to other common liquids. The inset shows a bottle of the ceramic polymer solution. (B–D) Rheological properties of the support gel (B) storage and loss moduli vs frequency; (C) shear stress vs shear rate; and (D) viscosity vs shear rate. The inset in C shows a container of the support gel (1 cP = 10^{-3} Pa.s).

Figure 2-3B−D shows the rheological properties of the support bath. As mentioned above, the support bath was prepared by adding silica nanoparticles (with an average size of ~200−300 nm) to the mineral oil to form a yield stress fluid. An ideal support bath should have characteristics of a solid to support the printed structure (during printing and also during thermal curing), as well as the characteristics of a fluid to enable nozzle movement with different speeds with minimal resistance. The yield stress fluid here serves as a support material that switches reversibly from a solid to a liquid when subjected to sufficiently high shear stress. During printing, the shear stress is provided by the nozzle motion. In the vicinity of the nozzle,

the liquid phase precursor polymer is dispensed from the nozzle. In the wake of the nozzle, the bath is designed to turn into a "solid" state (after removal of the nozzle shear stress), maintaining the shape of the liquid precursor.

Figure 2-3B shows the storage modulus (G') and the loss modulus (G") vs frequency for the bath. G' vs frequency remains flat and separated from the G", which is a characteristic of soft elastic solids with damping. The shear stress vs shear rate shows a plateau for low shear rate (< ~10 s^{-1}) (Figure 2-3C), which corresponds to the yield stress of the bath. For stress above this yield stress, the bath fluidizes or behaves like a fluid. The plateau region corresponds to shear rate independent stress dominated by elasticity. When the bath fluidizes for shear rate larger than the plateau region, its behavior is dominated by viscous loss. The Herschel−Bulkley model is commonly used to describe the behavior of yield stress fluids: $\sigma = \sigma_y + k\dot{\gamma}n$ in which σ_y is the yield stress, k is the consistency factor, and n is the flow index. For shear-thinning fluids, $n < 1$. Based on this model fitted to the data in Figure 3C, the yield stress of the bath is ~5.1 Pa, and the flow index and the consistency factors are 0.9 and 0.05, respectively. Given the low-yield stress of the bath compared to the hydrostatic pressure at reasonable bath depth (ρgh), there is no concern of static crevasse formation, since the hydrostatic pressure easily refills the fluid behind the nozzle. This is important to prevent the flow of the preceramic polymer into this space, which will result in skewed printing geometries. The support bath gel composition can be tuned by changing the silica nanoparticle concentration and the mineral oil type.

Figure 2-3D shows the apparent steady-state shear viscosity of the support bath calculated from the ratio of the steady-state shear stress and shear rate. The response shows a

shear- thinning behavior. The viscosity decreases from ~10^3 Pa·s to < 10^{-1} Pa.s over a shear rate range of 4×10^{-3} to 500 s^{-1}.

In this work, a commercially available preceramic polymer, without changing the chemistry or composition is used. Noted that the rheological properties of the bath and the preceramic polymer, the interfacial tension between the preceramic polymer and the bath, as well as the printing rate (nozzle travel speed), and the flow rate of the preceramic polymer in the nozzle overall determine the resolution and precision of the printing process. The cross-sectional area (A) of the extruded polymer from the nozzle is mostly determined by the flow rate (Q) and the travel velocity (V) of the nozzle ($A = Q/V$). The flow rate is controlled by a syringe pump. For these experiments, a flow rate of ~ 1 mL/min with a nozzle speed of ~15 mm/s was used. This results in a cross-sectional area of ~1.1 mm^2, which assuming a circular cross section yields a diameter of d ~ 1.2 mm. The diameter of the nozzle was ~0.6 mm. To prevent transient recirculating wake behind the nozzle, which can intermix the support bath material and the preceramic polymer, the nozzle speed must be kept below $V \sim \rho g L d$, in which ρ is the density of the bath, L is the nozzle length immersed in the bath, d is the nozzle diameter, and η is the bath viscosity [118]. In these experiments, the nozzle speed was well below the critical speed that would cause recirculating wake (~250 mm/s).

The instability caused by gravitational forces that result from density mismatch ($\Delta\rho$) between the support bath and the preceramic polymer solution may result in the sink or rise of the printed structures in the bath. For a sphere with diameter d, the rise/sink speed (V) can be found using $V_{rs} \sim \frac{\Delta\rho g d^2}{18\eta}$ [118].

Assuming a spherical geometry with the typical print cross-sectional area in this work (~1.2 mm), the sinking speed is estimated to be ~0.096 mm/s, which is rather small considering to the total printing duration. Given that the viscosity of the support bath depends on the shear rate (Figure 2-3D), in this calculation, a viscosity under the printing shear rate (~2 Pa·s) was used. In the absence of shear stress, the viscosity of the bath is more than 103 Pa·s, and hence the sinking speed would be nearly zero, as expected for solid behavior of the bath. Obvious sinking or rising of the printed object in the support bath was not observed during printing or after curing. The minimum stable feature size (I_c) to prevent the Rayleigh instability that will cause breakup of the printed preceramic polymer in the bath can be estimated using $I_c = \frac{\gamma_{oil-polymer}}{\sigma_y}$ [118], in which $\gamma_{oil-polymer}$ is the interfacial tension between the bath and the preceramic polymer solution and the σ_y is the yield stress of the bath ($\sim 5.1\ Pa$). However, the smallest stable feature size in this work was experimentally found ($\sim 0.7\ mm$), without break up of the printed polymer, and this is more attributed to the limitations of the printer and not to the process itself.

The thermogravimetric analysis (TGA/DTG) combined with differential scanning calorimetry (DSC) was used to obtain insight into the thermally induced chemical changes of the material during processing [119]. The thermal analysis (TGA/DSC/DTG) was conducted at a heating rate of 20 °C/min under a flowing N_2 atmosphere (see Figure 2-4A,B). In order to prevent any damages or depreciation to the DSC unit, the experiments were performed at 20°C/min. Because at lower heating rate the entire experiments would take several hours and could damage the DSC unit. Also, at this heating rate the nitrogen gas cylinder would be able to continuously supply the gas required for the experiments. According to thermal analysis

experiments, the total mass loss of the preceramic polymer during ceramization (the process of turning into a ceramic) up to 1000 °C was 16.4%. The thermally driven chemical cross-linking and pyrolysis lead to the observed mass loss through outgassing, which is also accompanied by material consolidation. The majority of the observed mass loss occurs at temperatures below 700 °C mainly within two temperature ranges. The first major mass loss occurs between 127 and 233 °C (by ~2.9%, the peak rate at ~158 °C). This mass loss is accompanied by a strong exothermic peak at ~168 °C in the DSC spectra. This mass loss is attributed to chemical cross-linking during which the precursor is transformed into an infusible organic/inorganic molecular network. Generally, hydrosilylation, hydrolysis, and condensation reactions are involved in the cross-linking stage of polymer-derived ceramics. The cross-linking is crucial to the formation of a 3D structure of ceramic at higher heat treatment temperatures as it prevents the melting of the material during later stages. The cross-linking process also increases the ceramic yield since it prevents the loss and fragmentation of low-molecular-weight components of the precursor. In this work, cross-linking was achieved using dicumyl peroxide [120]. The second major mass loss occurs in the temperature range of 593−933 °C (by an additional ~3.9%, the peak rate at ~623°C). Ceramization happens within this temperature range. Considerable bond cleavages and redistribution reactions between Si−H, Si−C, and Si−O occurs in this temperature range [120], [121]. The broad endothermic peak observed in the DSC response at this temperature range represents the energy intake for bonds cleavage. The mass loss in this temperature range is due to the formation of a variety of hydrocarbons such as CH_4 and hydrogen, which are released from the material [120]. As a result of the cross-linking and pyrolysis reactions, the ceramic material consisting of an amorphous SiOC network and free carbon (turbostratic domains) form. Various catalysts can

be used for cross-linking of the preceramic polymer. Type and the content of the added catalyst can affect the cross-linking process. This is because the cross-linking helps to preserve the precursor components with lower-molecular-weight during the ceramization step [120]. According to the recommendation of the supplier (Starfire), dicumyl peroxide is used as the catalyst. The mass loss of 16.4% in this experiment is much lower than the previous study (30%) by Kulkarni on the same polymer (SPR-036), in which 100 mL/g of the Pt catalyst was used [122]. Different mass loss ratios for the same precursor type can be attributed to different degrees of cross-linking during the early stages of heat treatment, as mediated for instance by the catalyst content.

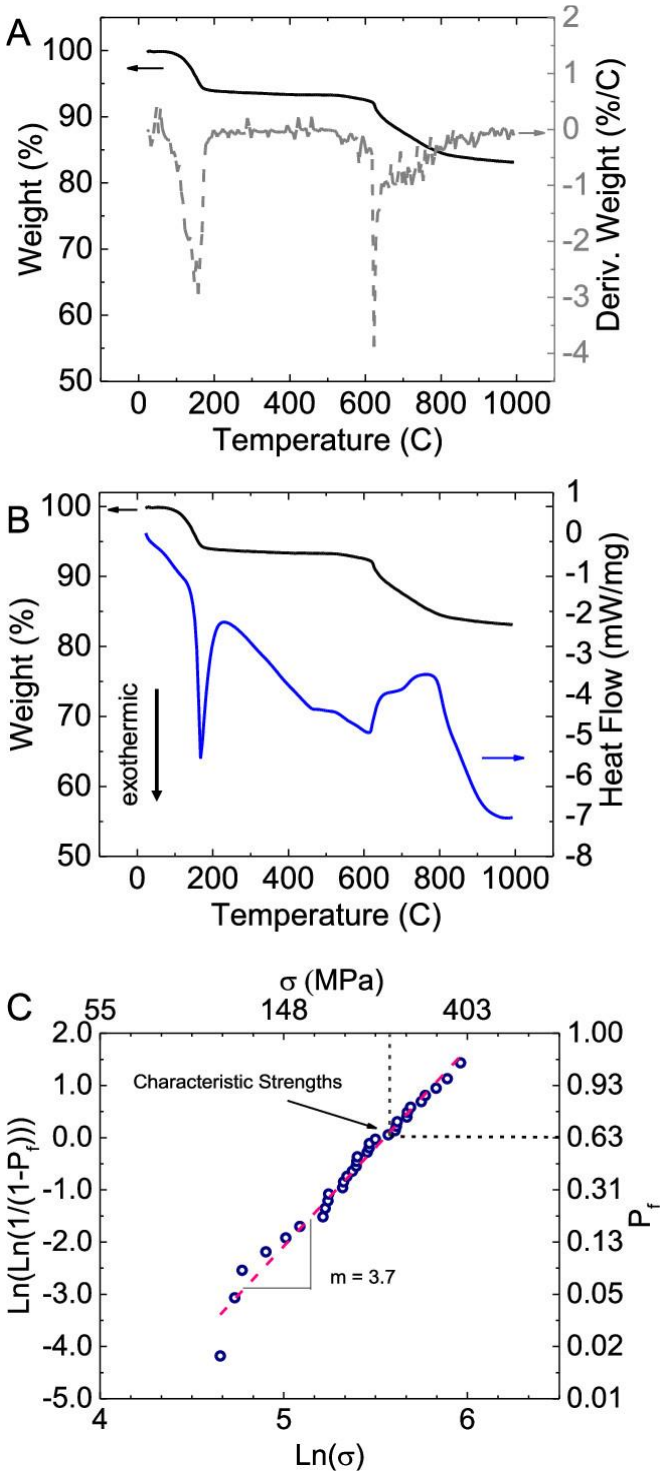

Figure 2-4 Thermal and mechanical properties. (A) Thermogravimetric analysis (TGA/DTG) response and (B) differential scanning calorimetry (DSC) response for the preceramic polymer. (C) Weibull plot for the strength of 3D-printed ceramic. n = 33.

Based on the thermal analysis results, a pyrolysis temperature–time profile was designed (Figure 2-5). The mass loss during ceramization is due to the release of gasses from the precursor polymer. Rapid heat-up during the ceramization may lead to the formation of defects and large pores. Hence, the heating rate in the temperature range of 450–900 °C was chosen to be several times slower than the initial rate. The pyrolysis temperature–time cycle was as follows: from room temperature to 450 °C at a heating rate of 2 °C/min, and from 450 to 900 °C at a heating rate of 0.5 °C/min, followed by a hold at 900 °C for 1 h.

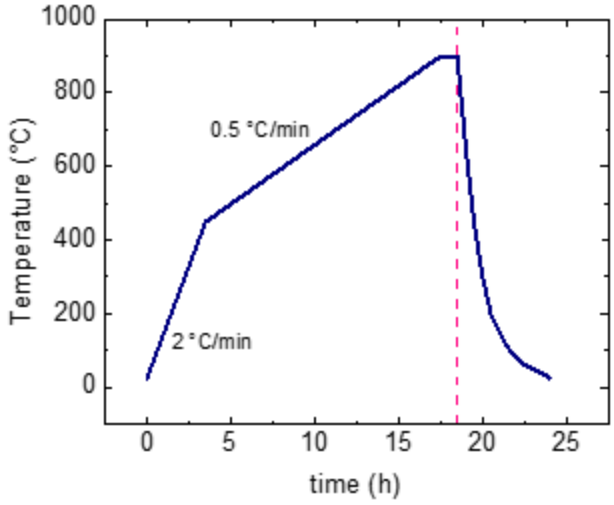

Figure 2-5 Pyrolysis temperature – time profile.

A separate thermal analysis was conducted on the support bath, and cross-linked cast preceramic (as opposed to 3D-printed inside a support bath) and cross-linked 3D-printed preceramic. The difference in the mass change between the cast and printed samples shows that even after rinsing with ethanol, a layer of mineral oil and silica nanoparticles remained on the surface of the printed parts. As it is shown in the TGA response of the bath (Figure 2-6), the mineral oil almost entirely evaporates during pyrolysis, leaving behind the condensed silica nanoparticles that coat the surface of the pyrolyzed specimens. This is also confirmed by

scanning electron microscopic (SEM) images and energy-dispersive spectrometry (EDS) analysis in Figure 2-7 and Figure 2-8 and Table 2-2.

The cured-cast specimen does not show noticeable mass loss for temperature ~ 600 °C. For higher temperature, up to 1000 °C, there is a total mass loss of ~ 11.5%, which corresponds to ceramization. The cured-printed specimen shows an initial mass loss at similar temperature to the support bath, an indication that some residues of the support bath (mineral oil and silica nanoparticles) are left on the printed specimen after retrieval from the bath. The mineral oil part of this residue is evaporated in the process, leaving behind a coating of consolidated silica nanoparticles on the specimen. This is also confirmed by SEM images and EDS analysis in Figure 2-7 and Figure 2-8 and Table 2-2. The thickness of this coating was estimated to be ~ 115 microns. For this estimation, a number of helices were printed, and the mass of the extruded polymer was calculated based on the printing time and the flow rate in the nozzle. After curing, the mass of each printed-cured specimen was again measured. This was repeated for the pyrolyzed specimens. Given the density of the preceramic polymer solution (1.1g/cm3) and the density of the mineral oil (0.85 g/cm3), the volume of the polymer and volume of the support bath residue was estimated, and the thickness of the oil coating on the cured sample was obtained.

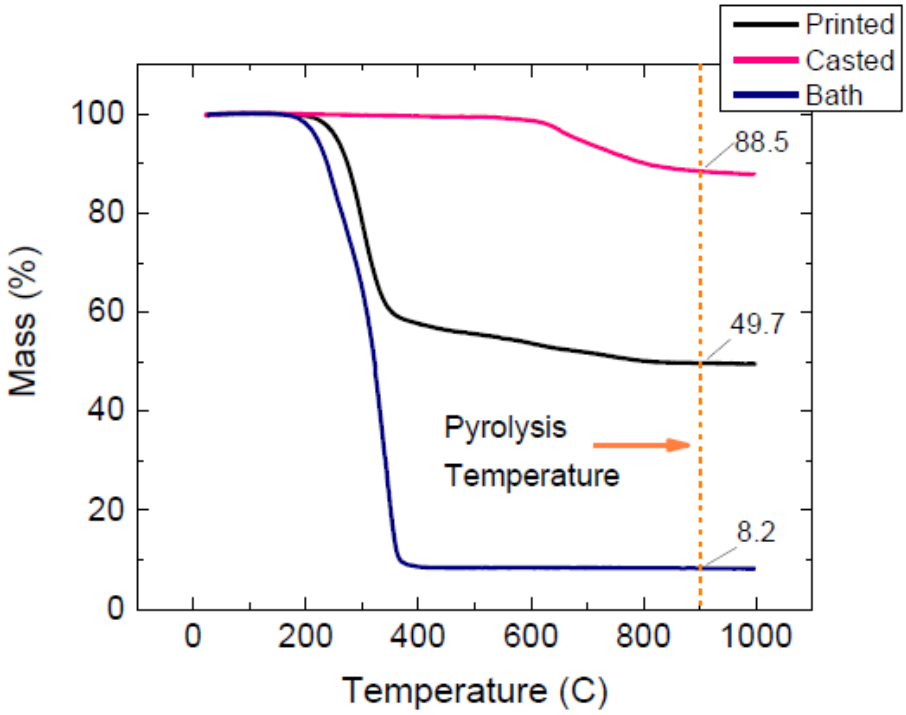

Figure 2-6 TGA response for the support bath, cross-linked cast material, and cross-linked printed-material.

The mechanical properties of the pyrolyzed 3D-printed ceramic were obtained by three-point flexure (bending) experiment. Details of the specimen preparation and testing procedure are presented in the Materials and Method section. For ceramics, the three-point bending test is preferred to the commonly used compression test [123]–[125]. This is because the compression test tends to close the processing flaws (such as microcrack and pores) in the material. However, during real-life applications, these processing flaws can be subjected to tensile loading. The compression test for ceramics does not truly examine such mechanical properties. A total of 33 3D-printed specimens were prepared according to the ASTM standard (C1684-18) [126].

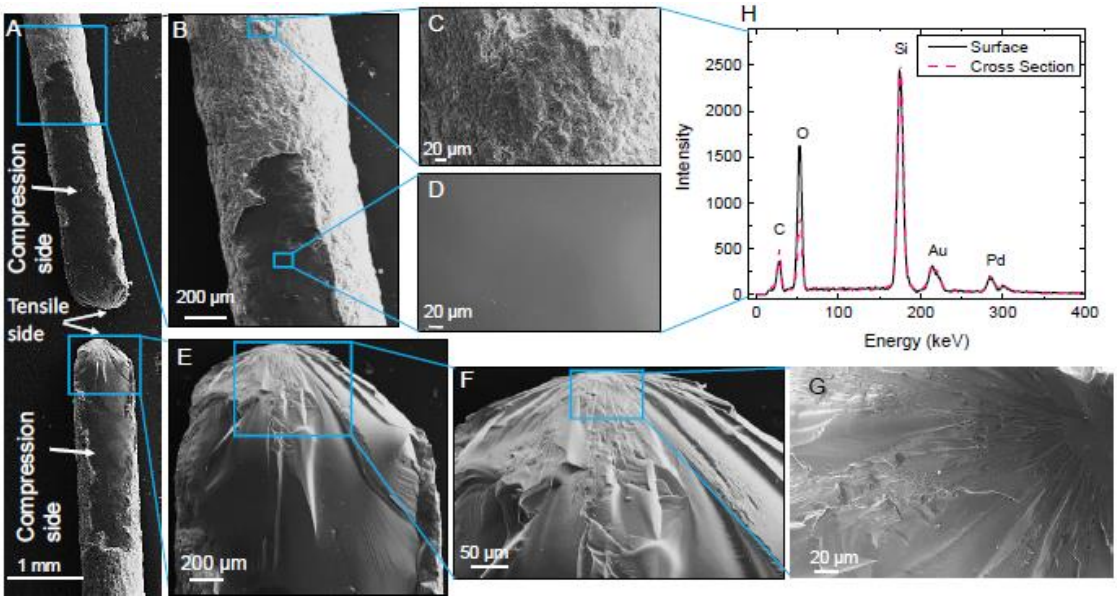

Figure 2-7 (A) - (G) SEM images of the three-point bending specimen after failure. (H) EDS spectra acquired from the cross-section and surface of the specimen.

Figure 2-7 shows SEM images of a 3D-printed specimen after three-point bending experiment. Figure 2-7A shows the two halves of the specimen after failure. Figure 2-7B-D show the surface and the cross-section of the specimen. The image of the cross-section shows that the specimen is dense, without any noticeable pores and cracks at SEM image resolution. The rough surface morphology can be attributed to the residual silica and oil burn-out on the specimen, as discussed above, and also revealed in the EDS spectra in Figure 2-7H. The gold and palladium peaks were because of the sputtering process needed to enhance the electrical conductivity of the specimen before SEM/EDS analysis. Figure 2-7A shows that the specimen failed on the tension-dominated side as expected for 3-point bending experiment. Magnified SEM images in Figure 2-7 E-G show the brittle nature of the fracture with shiny and smooth surfaces covered with hackle lines radiating from the fracture origin.

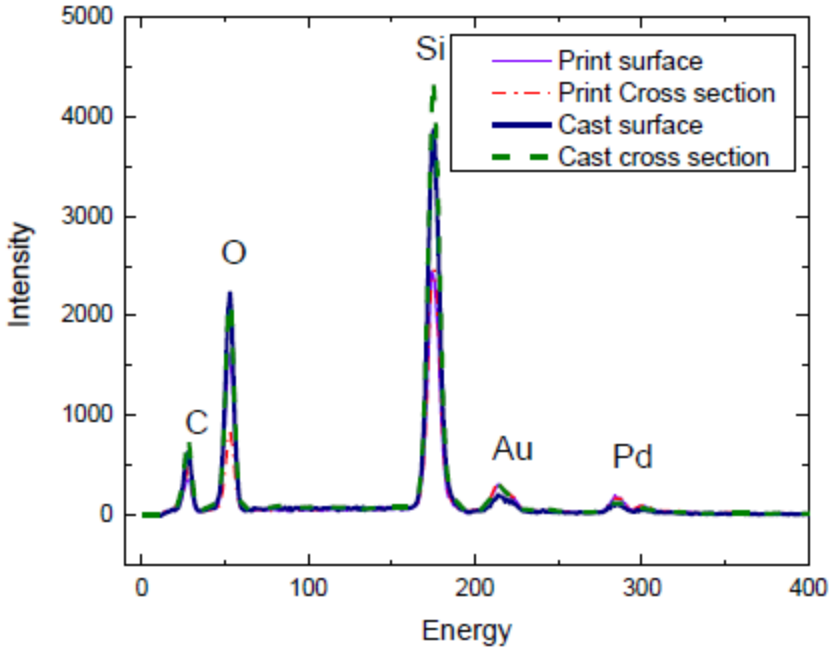

Figure 2-8 EDS spectra of surface and cross-section of both 3D-printed and cast ceramic.

The approximate composition of the 3D-printed specimens was obtained from EDS spectra (Figure 2-8) and presented in Table 2-2. For comparison, EDS spectra of the cast specimens are also presented. There is a minor difference in the elemental composition between the surface and cross-section of the cast specimen, which can be attributed to minor oxidation on the surface. The much larger oxygen content on the printed specimen surface is attributed to the residual silica nanoparticles, as discussed above.

Table 2-2 EDS elemental analysis and composition for the cast and printed specimens.

Element (at. %)	C	O	Si	Au	Pd	**Composition**
Cast surface	35	48.04	16.12	0.47	0.37	$SiO_3C_{2.2}$
Print surface	32.17	54.59	11.80	0.77	0.68	$SiO_{4.6}C_{2.7}$
Cast cross-section	39.15	44.38	15.58	0.49	0.39	$SiO_{2.8}C_{2.5}$
Print cross-section	44.64	39.45	14.01	0.98	0.93	$SiO_{2.8}C_{3.18}$

Figure 2-9 A 3D printed beam under 3-point bending test.3 shows a photograph of the ceramic beam under a three-point bending experiment mounted on an SEM Tensile Tester (tensile machine). tester. Figure S4 shows SEM images of typical fracture surfaces of the ceramic. Brittle nature of the fracture can be observed in the smooth and "shiny" surfaces.

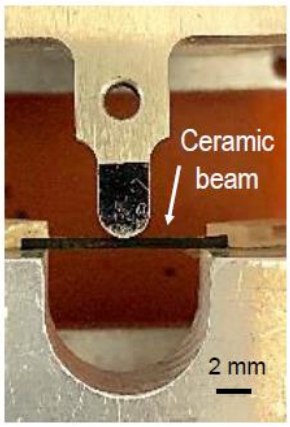

Figure 2-9 A 3D printed beam under 3-point bending test.

For the 3D-printed specimens, a strength of 232 ± 69 MPa (n = 33) was obtained. For ceramic materials, the ASTM standard [127] calls reporting statistical data based on Weibull distribution parameters. This is because the mechanical properties of the brittle materials largely depend on the distribution of flaws, and hence, deterministic approaches to analyze the data from the experiments are not comprehensive. The strength of the ceramic under three-point bending is expressed in terms of two-parameter Weibull distribution, as shown in Figure 2-4C, $P_f = 1 - exp\left(-\frac{\sigma}{\sigma_0}\right)^m$. [128] Such analysis considers the variability in the ceramic strength as a function of flaw population in the material. [129] m is the Weibull modulus, and σ0 is the characteristic strength. The Weibull modulus is the shape parameter that maps a failure probability of a specimen in a range of stress. Specimens' flexural strengths were ranked in ascending order and assigned a probability using $P_f = (i - 0.5)/n$, where n is the total

number of specimens. Probabilities and the flexural strength are presented in terms of $\ln(\ln(1/(1-P_f)))$ and $\ln\sigma$. Based on this analysis, the characteristic strength, which is the value of stress for $P_f = 63.2\%$, for the 3D-printed ceramics was calculated to be ~257 MPa. The linear regression of the flexural strength yields the Weibull modulus of $m = 3.7$ for 3D printed specimens.

The mechanical properties of the ceramics largely depend on the specimen geometry and different processing used, and as such comparison of absolute values with other processes may not be straightforward. For example, specimens made in the thin-film form show larger characteristic strength given their small dimension and consequently smaller probability of flaws. The thickness of the residual silica particles is estimated to be ~115 μm (Supporting Information). This coating is expected to affect the mechanical properties of the specimens, although marginal. This is given its small thickness (~10% of the specimen diameter), and also given that silica has comparable mechanical properties to the polymer-derived ceramic (SiOC). This residual silica layer can be polished from the surface of the printed parts, if the measurement of absolute mechanical properties is intended. For example, a large part can be printed, then the silica coating can be polished, and finally specimens can be cut from the polished material for mechanical property measurements.

Figure 2-10 Side-by-side images of a cured and pyrolyzed helix for shrinkage analysis after pyrolysis. shows side-by-side images of cross-linked and pyrolyzed specimens. The linear shrinkage (difference in the diameter d) was estimated to be ~15%. The shrinkage value was obtained using image analysis by subtracting the thickness of the residual oil. The 3D printed

PDC had the ceramic yield ~ 84%. Using this data, the ratio of the density of the pyrolyzed to the cured ceramic was obtained as following :

$$\frac{\rho_{pyrolyzed}}{\rho_{cured}} = \frac{\left(\frac{m}{v}\right)_{pyrolyzed}}{\left(\frac{m}{v}\right)_{cured}} = \frac{\frac{0.84\,m}{(1-linear\ shrinkage)^3}}{\frac{m}{v}} = \frac{\frac{0.84\,m}{0.85^3\,v}}{\frac{m}{v}} \quad (1)$$

$$= 1.37$$

Given the density of the preceramic polymer solution (1.1 g/cm^3), the final density of the pyrolyzed ceramic is estimated to be ~ 1.6 g/cm^3.

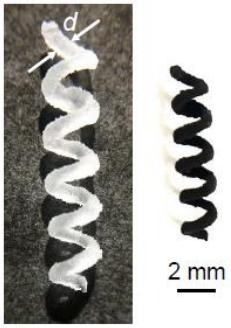

Figure 2-10 Side-by-side images of a cured and pyrolyzed helix for shrinkage analysis after pyrolysis.

2.3 Conclusion

A new process for the additive manufacturing of polymer-derived ceramics using a thixotropic support bath is presented. After printing and cross-linking in the same bath, the printed parts are retrieved from the bath and pyrolyzed to the final ceramic part. The one-step curing process after the printing process is advantageous for mechanical properties since no-

interlayer interfaces are generated in the process. Although this work focused on SiOC, the process can be readily extended to other preceramic polymers. There are many different types of preceramic polymers such as SiOC, SiC, SiCN, SiBCN, among others. The preceramic polymer functions as the precursor to the final ceramic, after it goes through cross-linking and pyrolysis. The properties of the final ceramic depend on the composition and properties of the preceramic polymer. The process can also be easily extended to ceramic composites by adding chopped ceramic fibers and/or functional nanoparticles. This work focused on printing lab-scale components; this process can be readily scaled up. The support gel is made of low-cost and commercially available mineral oil and silica nanoparticles. A large container of the bath can be easily prepared. The nozzle size can be varied to obtain components with smaller or larger sizes as required. Larger ovens and furnaces can be used for curing and pyrolysis steps.

3 INVESTIGATION OF THE PROCESS PARAMETERS FOR IN BATH PRINT AND CURE (IBPC) PROCESS

The democratization of thermoplastic 3D printing is rooted in the ease of processing enabled by economical melting and shaping. Thermosetting polymers, on the other hand, have not enjoyed this advantage given that thermosetting resins cannot hold their shape without cross-linking or excessive fillers, and once cross-linked, they cannot be extruded for printing. Due to this formidable challenge, thus far, 3D printing of thermosetting polymers has been limited to the photopolymerization of specialized photosensitive resins or extrusion of resins loaded with large fractions (as high as 20 wt. %) of rheology modifiers. Here, a rheology-modifier- and photoinitiator-free process for the 3D printing of a pure commercial epoxy polymer, without any resin modification and using a conventional 3D printer is presented. A low-cost non-Newtonian support material that switches between solid–fluid states under a nozzle shear stress enables the printing of complex 3D structures and the subsequent and "one-step" curing. The results show that the one-step curing eliminates the often-compromised interlayer adhesion common in layer-by-layer 3D printing processes and results in unprecedented isotropic mechanical properties (strength, elastic modulus, tensile toughness, and strain to failure). This in-bath print and cure (IBPC) 3D printing process for thermosetting polymers is low-cost, scalable, high-speed (nozzle speeds exceeding 720 cm/min), and high-resolution (down to 220 μm filament size). Potential applications for hobbyists, structural and aerospace components, and fiber-reinforced composites, among others are demonstrated.

3.1 Materials and Methods

3.1.1 Epoxy Preparation

Epoxy solution was prepared by mixing Epon Resin 862 (Hexion) and Epikure curing agent 3234 (Hexion) at a 100:16 weight percent ratio. All chemicals were used as received. The solution was mixed using a vortex mixer for 2 min followed by degassing under a vacuum for 5 min. Epon Resin 862 is a low-viscosity liquid epoxy resin, which is manufactured from epichlorohydrin and bisphenol F. This resin contains no diluents or modifiers. Triethylenetetramine (TETA) is an organic compound with the formula $[CH_2NHCH_2CH_2NH_2]_2$. The reactivity and applications of TETA are similar to the related polyamines ethylenediamine and diethylenediamine. It can be used as a cross-linker or hardener in epoxy. TETA is available as Epikure curing agent 3234, which is an unmodified aliphatic amine.

3.1.2 Carbon Fiber/Epoxy Composite Preparation

Short carbon fibers (Zoltek Corporation) were added to the epoxy at a 5:100 weight percent ratio. The average length and diameter of the carbon fibers were ~100 and 7.2 μm, respectively. The solution was mixed for 2 min using a vortex mixer. The epoxy/CF were degassed under a vacuum for 5 min. Higher loadings of carbon fibers are only possible when fibers are aligned, or the aspect ratio of the fibers is too small. In this process, the fibers aligned partially through the long, small-diameter nozzle by the syringe pump pressure (Figure 3-6). A drastic increase in the fiber volume ratio will result in the nozzle clogging. The fiber/polymer ratio was increased to find the threshold such that the epoxy/CF mix was easily flowable.

3.1.3 Support Bath Preparation

The support bath was prepared by mixing 4 wt. % Laponite RD (BYK Additives and Instruments) in 96 wt. % DI water at room temperature. The Laponite RD was added to DI

water while a magnetic stirrer was used at 1200 rpm until all particles dispersed into DI water, and it turned to a colorless and translucent colloidal dispersion. Subsequently, it sat for approximately 2 h at room temperature to complete the hydration process for the formation of the thixotropic fluid.

3.1.4 3D Printing

Printing was performed using a Delta-type 3D printer designed and built at UT Dallas. The epoxy resin was loaded into a 20 mL syringe and injected by an NE-300 Just Infusion syringe pump. A needle with an inner/outer diameter of 0.8/1.2 mm was used as the nozzle. The nozzle motion was controlled via custom-written script functions and trajectory files. A volumetric rate in the range of 0.4 – 0.8 mL/min was used in most experiments, unless otherwise stated.

After printing, the epoxy was cured at room temperature (~24 °C) for 12 – 20 h inside the same bath. Desirable properties of epoxy resins are obtained by the reaction of the epoxy resin with a curing agent. The curing process directly depends on the type of the curing agent. The curing process is an exothermic reaction, and the generated heat has to be managed to prevent possible thermal degradation. Epikure curing agent 3234 cures at room temperature. After curing, the printed parts were readily retrieved from the bath. Cured parts were washed with running water until all the stuck bath on their surface was completely removed. Thermal post-curing was performed using an oven at 85 °C for 4 h.

3.1.5 Measurement of Rheological Properties

The rheological measurements were performed using an Anton Paar rheometer using a 50-mm upper cone with an angle of 0.5° and a 50 mm in diameter lower plate. Frequency sweeps were taken at 1% strain from 10^2 to 10^{-2} Hz. The yield strength of the material was determined by applying a shear rate sweep from 10^3 to 10^{-3} s^{-1}. A three-interval thixotropy test (3ITT) was performed to study the structural breakup and recovery characteristics of the support bath. This test has three steps. It can be performed in a controlled shear stress (CSS) mode or a controlled shear rate (CSR) mode. In the CSS mode, the shear stress or torque is preset on the rheometer, while in the CSR, the shear rate or rotational speed is preset on the rheometer. This test is performed at two different shear rates. The first and last steps are performed at low shear rates, while the second step is performed at a high shear rate. In this experiment, the time-dependent changes in the bath viscosity can be extracted. In the first interval, which is at a low shear rate, the goal is to obtain a constant viscosity to simulate the performance of the sample at rest or a no-shear condition. In the second interval, a high shear rate is exerted on the sample to simulate the fluid microstructure breakdown. The last step, which is similar to the first step, is performed at a low shear rate similar to the first interval to simulate how the fluid recovers after the high shear removal. In this work, a preshear of 0.1 s^{-1} was applied for 20 s. The low shear rate step was preset to 0.1 s^{-1} for 50 s followed by a high shear rate of 100 s^{-1} for 10 s, and in the last interval, the shear rate was preset to 0.1 s^{-1} for 100 s.

3.1.6 Calculation of the Rheological Properties of the Epoxy

The dynamic viscosity and density of the Epon resin are 25 – 45 P and 1174.3 kg/m^3, and the dynamic viscosity and density of the curing agent TETA are 25 cP and 980 kg/m3, respectively. Note that the relation between dynamic viscosity (μ) and kinematic viscosity is

$\nu = \frac{\mu}{\rho}$. Considering the dynamic viscosity, density (ρ), and mass fraction (x) of the Epon resin and the curing agent TETA, the viscosity of the epoxy was calculated using the Gambill equation ($\nu_E^{0.3} = \nu_R^{0.3} x_R + \nu_C^{0.3} x_C$). The calculated dynamic viscosity of the epoxy mixture was obtained to be 21.9 P.

3.1.7 Mechanical Characterization

The tensile tests were performed using a Lloyd LR5KPlus Universal Materials Testing Machine with a 500 N load cell. Each test was performed at room temperature at a 1 mm/min crosshead speed. Tensile specimens were punched out of the large 3D-printed sheets using an ASTM D638 Type V dogbone die at different directions with respect to the print direction. The cast samples were punched out from the cast sheets. Both sides of the samples were slightly polished before the tensile tests. Tensile specimens were gripped using Lloyd TG22 self-tightening roller grips. At least three specimens for each direction were used to perform the tensile tests.

3.1.8 Statistical Analysis of the Mechanical Properties

To investigate the differences among the mechanical properties of the three groups of tensile tests for different printing layer directions, a statistical analysis was performed. One-way analysis of variance (ANOVA) was used for comparison of the mean value of two or more independent groups of samples. ANOVA tests whether the samples are drawn from populations with the same mean values or not. It calculates an F statistic, which is the ratio of the variance among the means of the groups to the variance within the samples. In the case that the group means are drawn from populations with the same mean values, the variance

between the group means needs to be lower than the variance of the samples. Here, for mechanical properties of the three different layer directions (0, 45, and 90°), one-way ANOVA was performed. The P value corresponding to the F statistic of the one-way ANOVA was calculated to be 0.6, 0.12, 0.46, and 0.66 for the strength, modulus, strain to failure, and tensile toughness, respectively, which are higher than 0.05 (5% significance level). It means that, at this significance level, the mechanical properties of the 3D-printed specimens at different printing layer directions are not significantly different. Even though the data did not show any significant difference in the properties of the 3D-printed specimens in different printing layer directions, a Tukey HSD (honestly significant differences) test was performed to obtain more insight into the possible differences between each pair of data. The Tukey HSD test determines whether the relationship between two groups of data is statistically significant. The calculated Tukey HSD P values are presented in Table S3 and are higher than the significance level, demonstrating that there is no statistically significant difference in the mechanical properties of the tensile specimens prepared at different printing layer directions.

3.1.9 DSC/TGA Analysis

Differential scanning calorimetry (DSC) and thermal gravimetry analysis (TGA) were performed using an STA449/F5 Netzsch DSC/TGA. The sample size was limited between 12 and 14 mg. The measurements were performed from room temperatures up to 700 °C with a heating rate of 20 °C/min in a nitrogen gas environment.

3.1.10 SEM Imaging

A Zeiss Supra 40 SEM was utilized to measure the cross-sectional area of the printed filaments. Since a good electrical conductivity is required to obtain high-quality images, a gold–

palladium film was sputtered on the epoxy parts. The composition of the epoxy was measured by the EDAX material analysis system.

3.1.11 Surface Finish Characterization

The surface finish of the printed samples was characterized using a Veeco Dektak 8 Profilometer. Surface height as a function of stylus scanning distance was recorded. The scanning rate was 6000 μm in 225 s in the direction perpendicular to the printed layers.

3.1.12 Micro-CT Imaging

Micro-CT imaging was performed using a Nikon 225 kV C1 Granite based precision CT system. The voxel size in this equipment is up to 3 μm. Micro-CT imaging was achieved by capturing the changes in attenuation of an X-ray beam through the sample. Cross-sectional images (2D slices) were then reconstructed from attenuation measurements by the detectors. These 2D slices were stacked on each other to create a 3D structure. The micro-CT data were processed using the Dragonfly software to produce 3D rendered models of the printed object and calculate the void fraction in the printed object.

3.2 Results and Discussions

The printer operates on the principle of direct extrusion of a TS resin into a non-Newtonian fluid bath (Figure 3-1). Lewis and co-workers reported the omnidirectional printing of 3D microvascular networks by printing fugitive ink filaments within a photocurable gel reservoir, which physically supports the patterned features [130]. This process was extended to bioprinting applications in which a bath serves as a temporary and biocompatible support to print complex biological samples containing cells and hydrogels [131], [132].

Hinton et al. reported 3D printing of hydrophobic polydimethylsiloxane (PDMS) elastomer in a hydrophilic carbopol gel via freeform reversible embedding (FRE) [133]. This study demonstrated that hydrophobic polymers with low viscosity and long cure times can be 3D printed using a hydrophilic support. O'Bryan et al. reported a method to make micro-organogels swollen in mineral oil using block copolymer self-assembly to enable 3D printing of oil-based materials such as silicone. The results showed that the rheological properties of this micro-organogel material are tunable, leveraging the jamming transition, which facilitates its use in 3D printing of silicone structures [134]. Afghah et al. used a composite pluronic-nanoclay support bath, which resulted in a shear-thinning composite support bath with fast self-recovery behavior, for the bioprinting of cell-laden alginate-based hydrogels [135].

Figure 3-1 The bath is low-cost (<$2/lit), easy and fast to prepare in large quantities, and it is transparent, which facilitates process monitoring.

This process is built on these concepts by leveraging the two-step curing of a pure epoxy ink (epoxy resin and curing agent) extruded inside a thixotropic (time-dependent shear thinning) support bath. The thixotropic bath shows time-dependent microstructure collapse and buildup in the presence and absence of a moving nozzle, respectively. The microstructure

collapse allows for the extrusion of the epoxy ink, and the buildup physically supports the printed ink to print complex 3D structures in a layer-by-layer or omnidirectional fashion. Once the printing process is over, the thermosetting polymer is first "partially cured" inside the bath in a room environment for 12–24 h, "at once". This one-step partial curing eliminates the weak interlayer interface often encountered in layer-by-layer processes such as FDM (fused deposition modeling). This process is called In-Bath Print and Cure (IBPC) for 3D printing of thermosetting polymers.

A thixotropic fluid can switch between a solid behavior and fluid behavior under shear stress (mayonnaise and shaving cream have this property). This property can be observed as the bath can hold its shape when kept upside down, while if it is vigorously shaken, it will flow. When the nozzle moves in a thixotropic fluid, under the nozzle shear stress, the bath fluidizes in the nozzle vicinity. The bath returns to a solid behavior behind the nozzle track. When the low-viscosity epoxy is extruded from the nozzle tip, the printed geometry is maintained stable once the thixotropic fluid returns to its solid behavior. Once printing is finished, the printed epoxy is first partially cured (cross-linked). The partially cross-linked epoxy is retrieved from the bath and fully cured in an oven.

During this partial cure, the cross-link density in the epoxy increases and results in a structure that can be pulled out of the bath and subsequently fully cured in an oven at higher temperatures. Thermal analysis shows that the partially cured epoxy shows a glass transition temperature (Tg), albeit at a much lower temperature compared to the fully cured epoxy, followed by residual curing at higher temperatures. The presence of detectable Tg shows that room temperature curing generates enough cross-linking density in the material such that it can maintain its shape during pullout from the bath, as well as during several hours of

subsequent full cure. Since the partial curing occurs in a room environment, an aqueous thixotropic bath (Laponite in DI water) was used. Hence, the partial curing occurs inside the water, which may also facilitate the heat dissipation during the exothermic curing process.

The IBPC process enables 3D printing of complex 3D structures using "pure" epoxy without any need for rheology modifiers that are required in the direct ink writing (DIW) process [30] or the modification of the resin with specialized photoinitiators for photocurable processes [20], [23]. Because the bath functions as the sacrificial support, there is no need to print support structures even for complex geometries. As an example, a helical spring with a wire diameter of 1.5 mm and a mean diameter of 20 mm using omnidirectional printing inside the bath was printed (Figure 3-2a). The spring is deformable and fully elastic for many cycles given the absence of any additives in the ink (Figure 3-2b). Printing of a tensegrity table (Figure 3-2c), a honeycomb structure with a gradient lattice (Figure 3-2d, Figure 3-3), equilateral triangles (Figure 3-4), and an airfoil (Figure 3-2e) were demonstrated. The tensegrity structure is supported by four threads in which the cotton threads are in tension, while the discontinuous support beams are in compression.

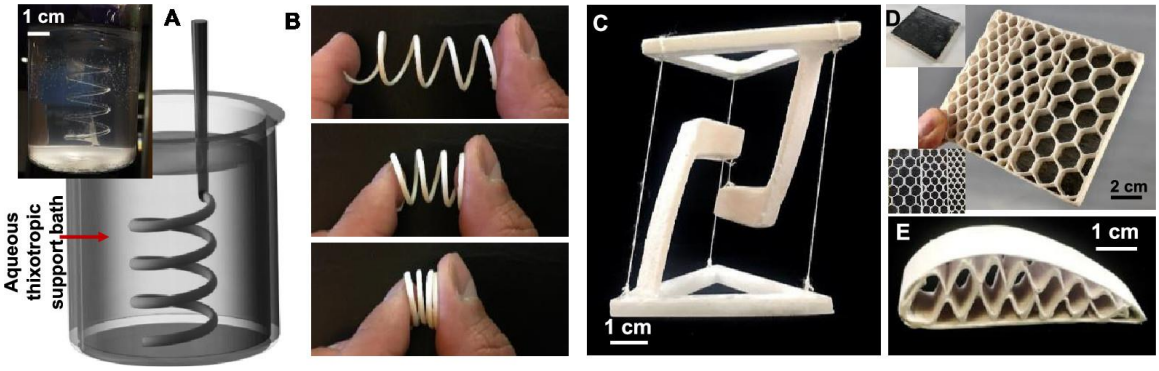

Figure 3-2 The IBPC thermoset 3D printing process and examples of the 3D-printed structures. (A) The schematic illustration and an image show the printing of a helix inside

a thixotropic bath. (B) The 3D-printed epoxy helix shows excellent deformability. (C–E) Images of a 3D-printed tensegrity table, a gradient honeycomb, and an airfoil.

In a sandwich panel, the core transfers the force to the load-carrying skin. The gradient lattice structure generated by 3D printing will allow for the optimization of the lattice size based on the load profile, for example, in beam structures. A carbon fiber (5 wt. %) reinforced epoxy skin was printed on one side of the panel (Figure 3-3). Given their superior mechanical properties, thermosetting polymers may be used for urban air mobility applications.

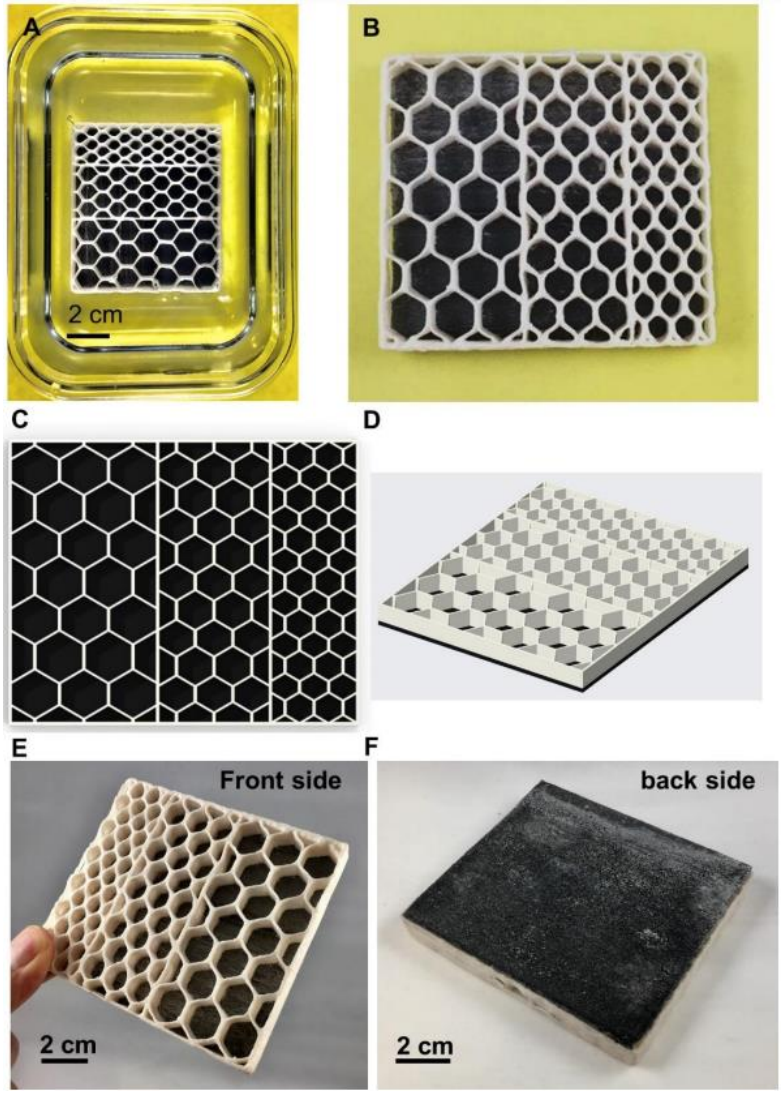

Figure 3-3 Photo of the 3D-printed gradient honeycomb, (A) inside the support bath after curing, and (B) after post-curing. (C) and (D) are the corresponding CAD files. (E) and (F) photos of the front-side and back-side that show the gradient structure, and the carbon-fiber-reinforced skin.

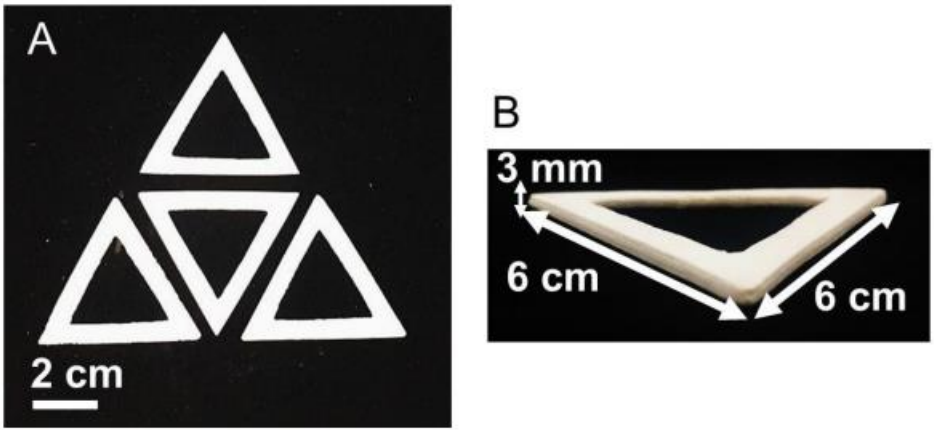

Figure 3-4 (A) Four 3D-printed equilateral triangles. (B) The iso-view of one triangle.

As a proof of concept, a small-scale ducted fan, Figure 3-5a (of an air taxi, inset), in which the propeller (dark color) is a carbon fiber reinforced epoxy (Figure 3-6) was printed. To assess whether the shear stress in the nozzle results in carbon fiber alignment, SEM images from freeze-fractured carbon fiber reinforced filaments were acquired. The SEM images were acquired parallel to the cross section of the filament (Figure 3-6c–e). It can be observed from the SEM images that the fibers are partially aligned along the filament axis. Image analysis was performed to quantify the angle of the carbon fibers with respect to the filament axis, and the results are shown in Figure 3-6f.

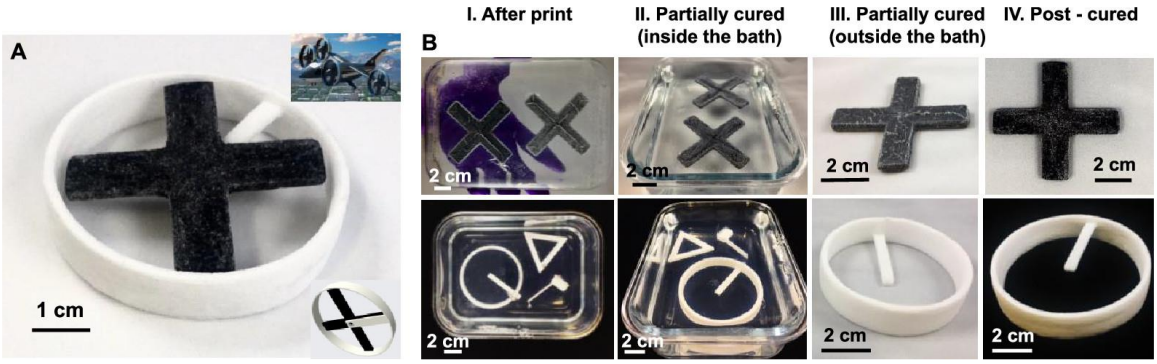

Figure 3-5 The steps in 3D printing carbon fiber reinforced epoxy composite. (A) An image of the 3D-printed ducted fan. The propeller is printed using chopped carbon fiber reinforced epoxy. The insets show the corresponding computer image and an air taxi with four ducted fans. (B) The steps in the IBPC process: print and partially cure inside the thixotropic bath and post-cure inside an oven. The dark-colored material in the images is the 3D-printed carbon fiber reinforced epoxy.

All these structures with several centimeters in size were printed in several minutes, for example, the air foil and the gradient honeycomb took ~3 and ~13 min, respectively (Table 3-1). Different stages of the IBPC process are shown in Figure 2b, which shows parts (i) after printing inside the bath, (ii) after partial curing in the bath and (iii) out of the bath, and finally (iv) after post-curing in an oven. The printed parts are stable and maintain their geometry throughout the process for hours even in the uncured phase inside the bath.

Table 3-1 Printing duration for various structures presented

Geometry	Print duration (min)
Helix	0.4
Honeycomb	7.6
Gradient honeycomb	13
Propeller	7.3
Fan	10
Tensegrity table	14
Tensile test sheets	13.7
Airfoil	3

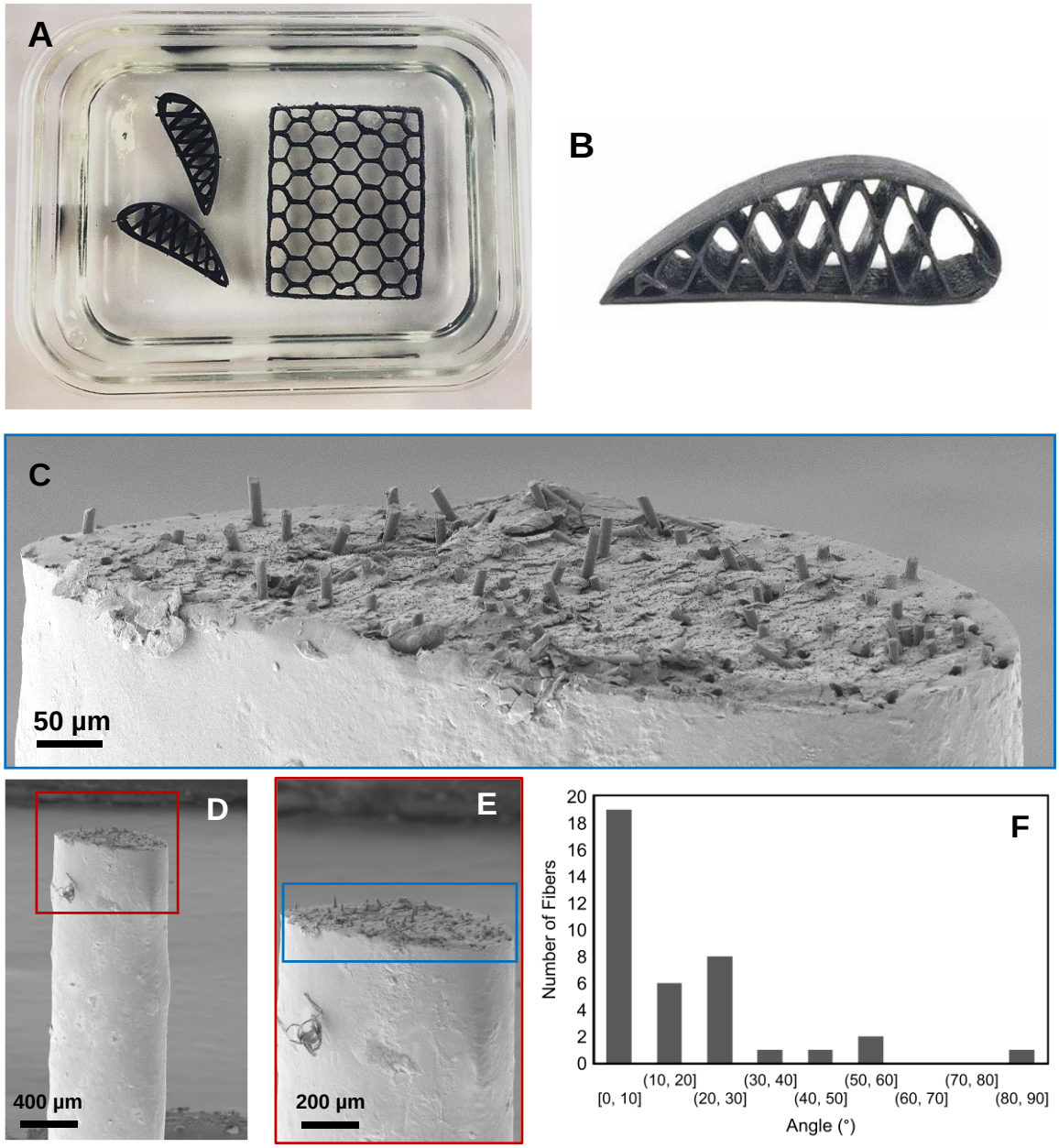

Figure 3-6 Chopped carbon fiber-reinforced epoxy parts, (A) after printing inside the support bath, (B) the airfoil after post-curing. (C) An SEM image of the cross-section 3D- printed of CF-reinforced epoxy. (C) – (E) SEM images of the carbon fiber-reinforced epoxy filament in different magnifications. (D) The histogram of the carbon fibers angles respect to the filament angle.

Most often, in 3D-printed materials, the interlayer interfaces are the weakest links, which often arise from layer-by-layer deposition and curing. For these materials, the mechanical

properties are anisotropic, with properties being better along the print direction than the transverse direction, often by several times [30], [36], [136]. Recently, the HARP process has been introduced by Mirkin and co-workers for 3D printing of photocurable resins, in which the continuous printing enabled by a mobile liquid interface resulted in isotropic mechanical properties regardless of the print direction [20]. To determine whether the IBPC process results in an isotropic material, tensile tests based on the ASTM standard were performed. For these experiments, large sheets of epoxy, ~10 × 8 cm were printed (Figure 3-7a, Figure 3-8). Tensile specimens were punched out using an ASTM D638 Type V cutting die in different orientations (0, 45, and 90°) relative to the printing direction (Figure 3-7b). The surface finish depends on several factors including the nozzle speed and also the interfacial tension between the bath and the epoxy and the yield stress of the bath. Since the nozzle velocity affects the filament diameter, it would also affect the surface finish of the printed sheets. Samples printed at higher speeds should have smoother surfaces since individual filaments that form the surface will have a smaller diameter. For mechanical measurements, the surface of the samples were polished. The high surface tension tends to minimize the surface area. This seems to be the reason for having a relatively smooth surface for the printed sheets.

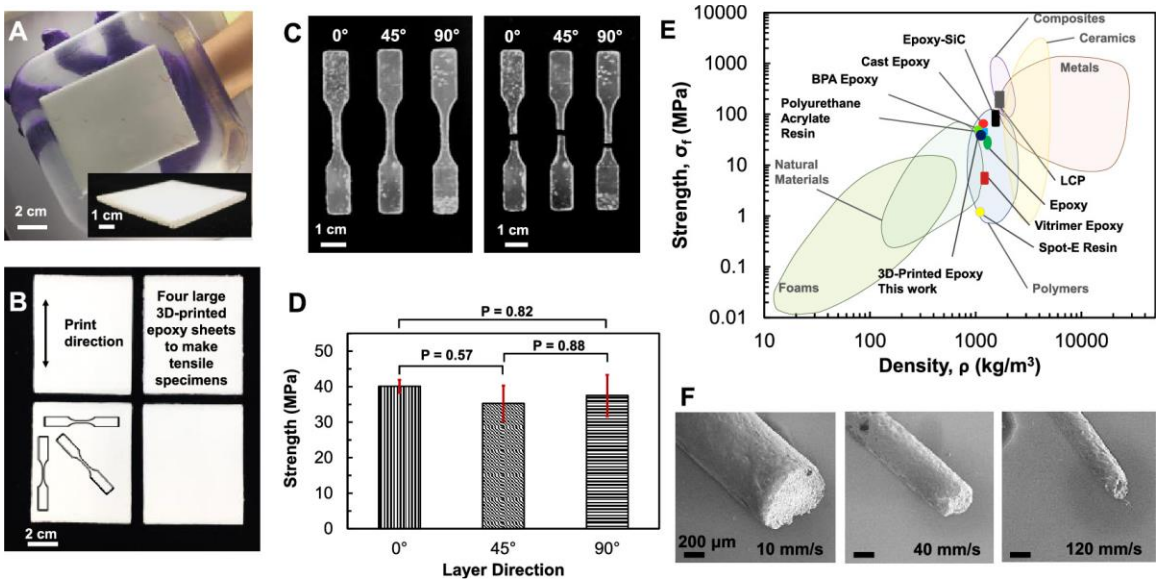

Figure 3-7 Isotropic mechanical properties of the printed structures. (A) An image of a 3D-printed epoxy sheet for the tensile test inside and outside the bath. (B) Tensile test specimens were punched out from the printed sheets using an ASTM standard die in different orientations with respect to the print direction. (C) Photos of the dogbone specimens before and after the tensile test. (D) Strength for samples with different printing layer directions. (E) An Ashby plot for strength vs density comparing the properties of the printed epoxy in this work with the literature (details are provided in the Supporting Information). (F) The SEM images of the filaments printed in three speeds (10, 40, and 120 mm/s).

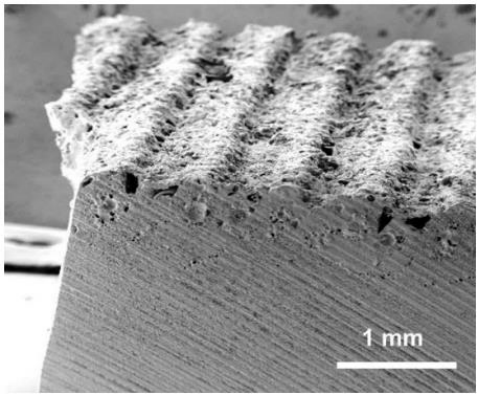

Figure 3-8 An SEM image of the printed epoxy sheet used for tensile test. This sample was cut using a diamond saw from the printed sheet, and the lines on the side-surface are traces of the saw. The top surface shows the as-print (unpolished) surface of the sheet.

The specimens showed a similar fractured pattern (Figure 3-7c). The results showed that the specimens have isotropic mechanical properties indicated by insignificant Tukey's HSD (honest significance difference) test (Figure 3-7d, Figure 3-9, and Table 3-2, Table 3-3). The strength of the tensile specimens at printing directions of 0, 45, and 90° was 40.1 ± 1.8, 35.3 ± 5, and 37.5 ± 5.8 MPa, respectively. Generally, additive manufacturing processes produce objects that have inferior mechanical properties compared to the conventional manufacturing processes. This can be attributed to several factors depending on the process and material type. These factors include the formation of voids during printing, cold junction between interfaces, and poor surface finish, among others. In the case of the process presented in this work, the bath (water) may also affect the mechanical properties. To ensure that the underlying material strength was measured, the surface of the tensile sheets was slightly polished.

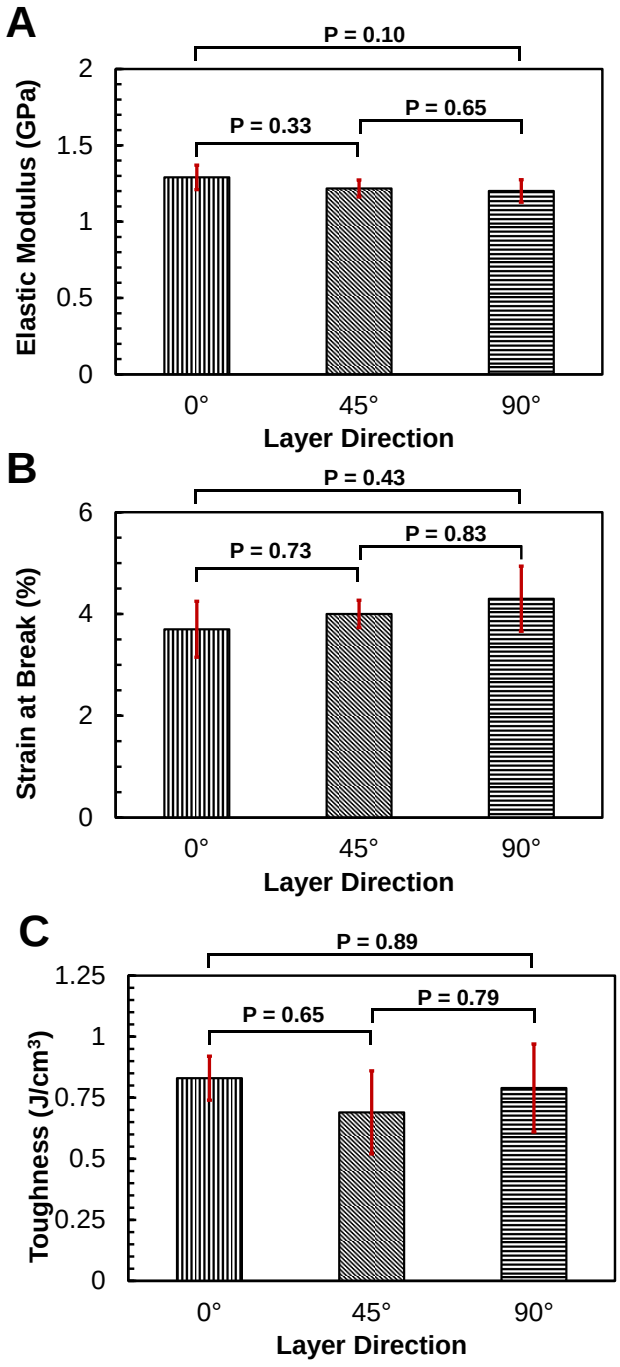

Figure 3-9 Statistical comparison of the elastic modulus, strain at break, and tensile toughness for the printed epoxy in different orientations with respect to the print direction.

Table 3-2 Mechanical properties for the printed epoxy in different orientations with respect to the print direction.

Sample Angle	Strength (MPa)	E (GPa)	Strain at Break (%)	Toughness (J/cm^3)
0	40.1 ±1.8	1.26 ±0.10	3.7 ± 0.55	0.83 ± 0.09
45	35.3 ± 5	1.14 ± 0.05	4.0 ± 0.27	0.69 ± 0.17
90	37.5 ± 5.8	1.07 ± 0.08	4.3 ± 0.64	0.79 ± 0.18

Table 3-3 The results of the Tukey's HSD test on tensile specimens with different print orientations. (A) strength, (B) elastic modulus, (C) strain at failure, and (D) tensile toughness.

A

Printing Direction Pair	Tukey's HSD P-value	Tukey's HSD Inference
0° vs 45°	0.57	Insignificant
0° vs 90°	0.82	Insignificant
45° vs 90°	0.88	Insignificant

B

Printing Direction Pair	Tukey's HSD P-value	Tukey's HSD Inference
0° vs 45°	0.33	Insignificant
0° vs 90°	0.10	Insignificant
45° vs 90°	0.65	Insignificant

C

Printing Direction Pair	Tukey's HSD P-value	Tukey's HSD Inference
0° vs 45°	0.73	Insignificant
0° vs 90°	0.43	Insignificant
45° vs 90°	0.83	Insignificant

D

Printing Direction Pair	Tukey's HSD P-value	Tukey's HSD Inference
0° vs 45°	0.65	Insignificant
0° vs 90°	0.89	Insignificant
45° vs 90°	0.79	Insignificant

To visualize the internal structure of the printed specimens, micro-CT images were acquired. Figure 3-10 shows a 3D micro-CT image of a broken tensile specimen. The void diameter distribution histogram shows the size of the voids detected within the machine resolution (>~3 μm). The void volume fraction was calculated by dividing the void volume by the total volume. The void volume fraction was calculated to be less than ~0.1%. Moreover, the density of the printed objects was calculated using the Archimedes method. The obtained density (~1.15 g/cm^3) was in good agreement with the density of Epon epoxy (~1.2 g/cm^3). From the micro-CT and density measurements, it can be concluded that the printed objects

are nominally solid with a very low void volume fraction. In other words, the printed material is solid with no apparent porosity (Figure 3-11). The combination of surface defects and bath effect (effect of water during curing) may have resulted in lower mechanical properties compared to cast epoxy. This point deserves more investigation to fully understand the bath effect in this process.

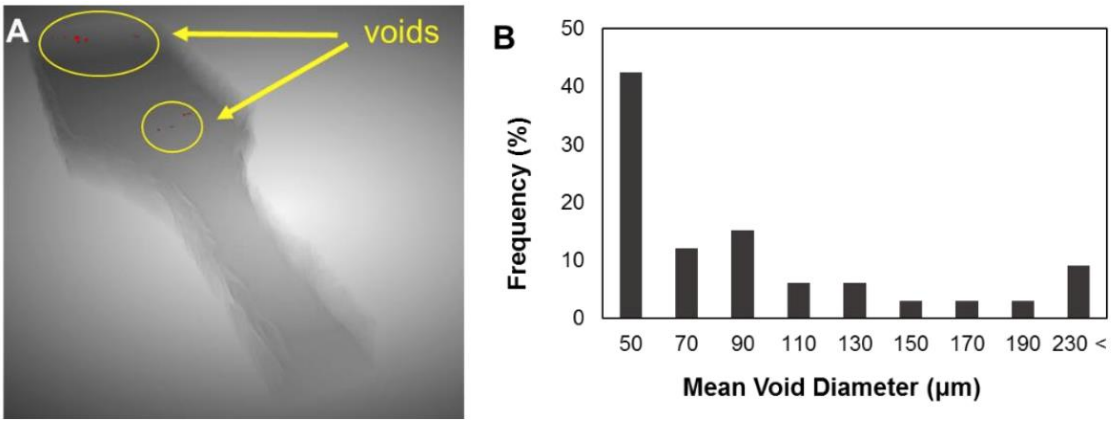

Figure 3-10 (A) A 3D micro-CT image of a broken tensile specimen. The red dots are identified as voids. (B) The void diameter distribution histogram.

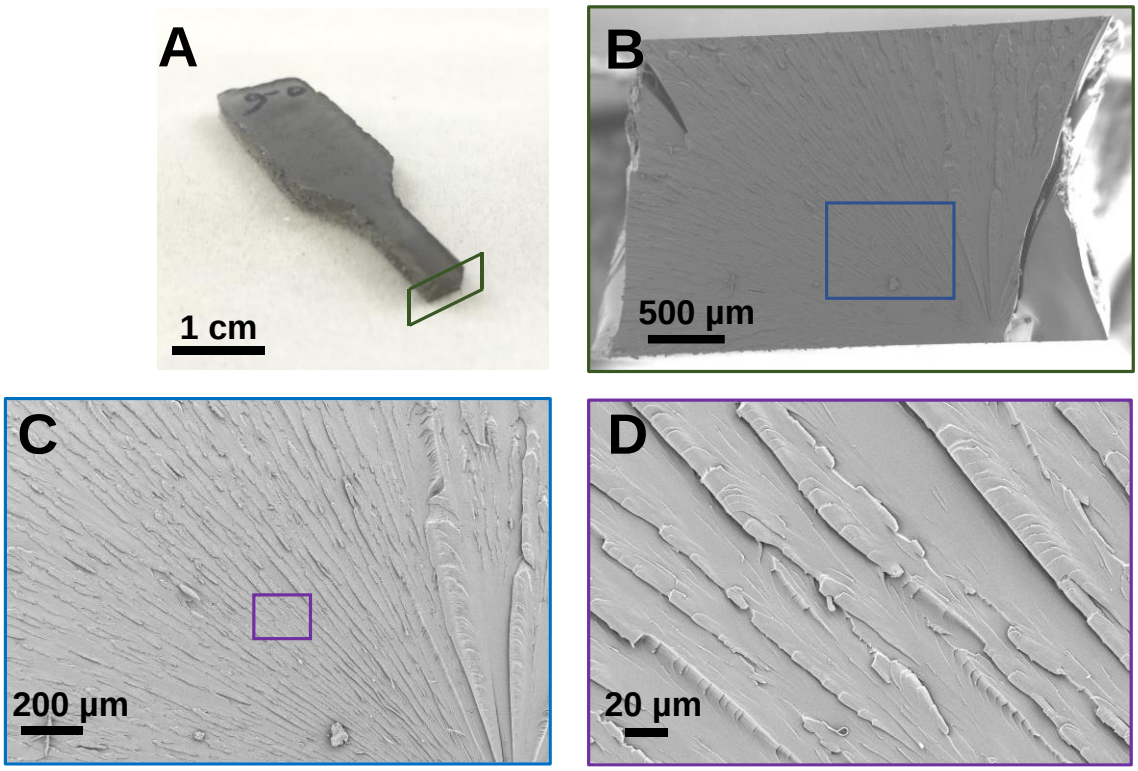

Figure 3-11 SEM images of the cross-section of the tensile specimen in various magnifications.

Figure 3-7e shows an Ashby plot for strength vs density comparing the properties of the 3D-printed epoxy in this work with the literature. Isotropic mechanical properties are often an indication of strong interlayer interfaces. The interface between the printed layers was examined using scanning electron microscopy (SEM). The SEM results show that the interlayer interfaces are fully fused with each other (Figure 3-12a), which indicate that the presence of the bath does not affect the interface, and consecutive printed layers form strong chemical bonds after full cure.

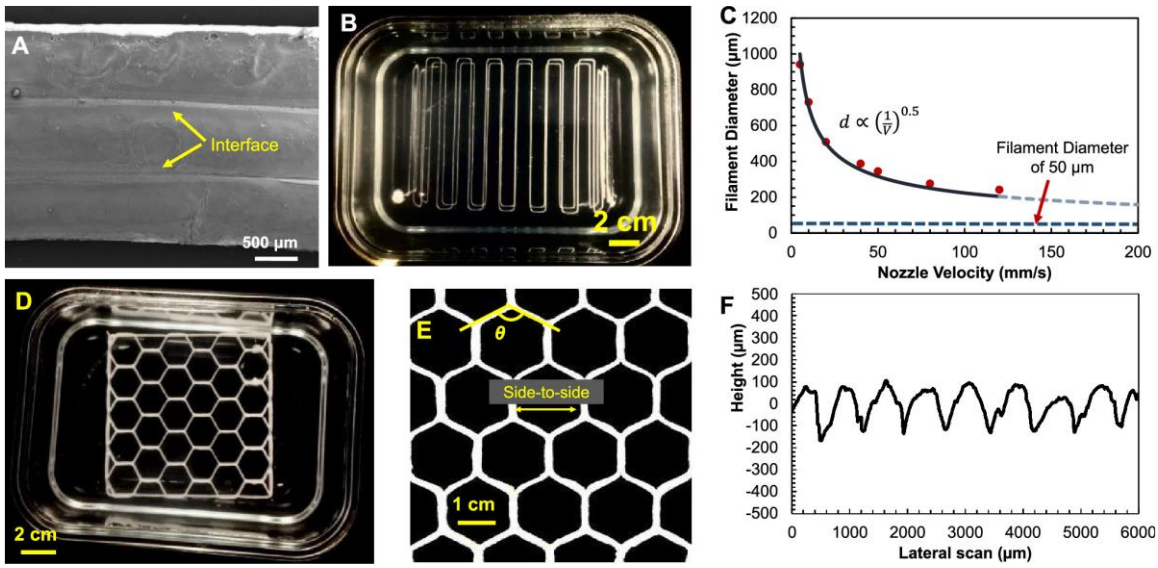

Figure 3-12 High-quality interlayer interface, print fidelity, and print diameter vs nozzle speed. (A) An SEM image shows the interlayer interface between three printed epoxy layers; nearly perfect bonding in the interface is observed. (B) Filaments printed with different nozzle speed. (C) The printed filament diameter vs nozzle speed. The solid line shows a trend line based on $\propto \sqrt{\frac{1}{V}}$. The horizontal dashed line shows the filament diameter of 50 µm, which is associated with the onset of the Rayleigh instability, corresponding to the nozzle speed of ~2000 mm/s. (D) A photo of a printed honeycomb inside the support bath. (E) A zoomed-in view after post-curing used for print fidelity (length and angle) analysis. (F) A profilometer height profile acquired from the surface of a sample printed with a nozzle speed of 50 mm/s.

To evaluate the printing resolution of the IBPC process, single filaments were printed under a constant flow rate while increasing the nozzle speed (V). The nozzle speed was increased from 5 up to 120 mm/s (the speed limit of the printer) (Figure 3-12b and Figure 3-13). The filaments' diameters were measured using SEM (Figure 3-7f, Figure 3-14, and Table 3-4). The results show that filaments are circular, and the filament diameter decreases from ~945 to ~220 µm when the nozzle speed increases from 5 to 120 mm/s. The nozzle diameter to print these filaments was ~840 µm. Hence, with the same nozzle, various filament diameters can be printed by changing the nozzle speed. It was found that the filament diameter (d) vs

the nozzle speed estimated from volumetric print rate ($Q \sim \frac{\pi d^2}{4} v$) follows a similar trend ($d \propto \sqrt{\frac{1}{V}}$) to the measured filament diameter (Figure 3-12 and Figure 3-15), albeit the measured diameters are consistently smaller than the theoretical estimate. This shows that the volumetric print rate does not solely define the print diameter.

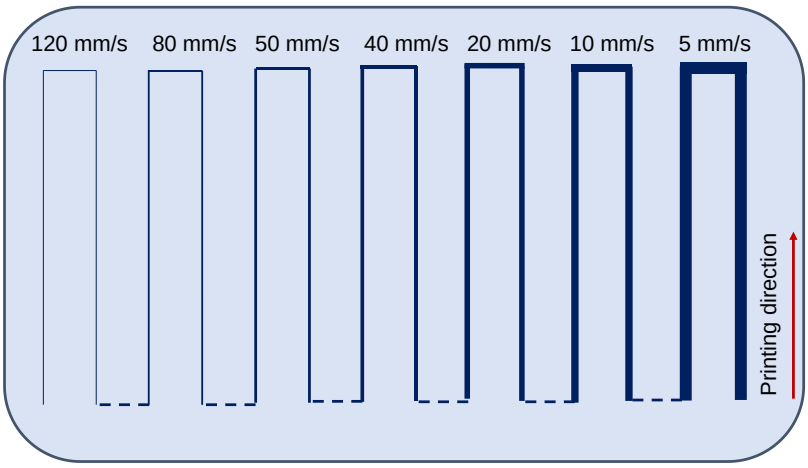

Figure 3-13 (A) The schematic of printed filaments at a constant flow rate and different nozzle speeds. The faster nozzle speeds result in thinner filaments.

Table 3-4 The nozzle speed corresponding to SEM images in Figure 3-14.

Sample	Nozzle speed (mm/s)	Diameter (μm)
A	5	945.2
B	10	638.4
C	20	437
D	40	344.5
E	50	322.4
F	80	257.8
G	120	219.2

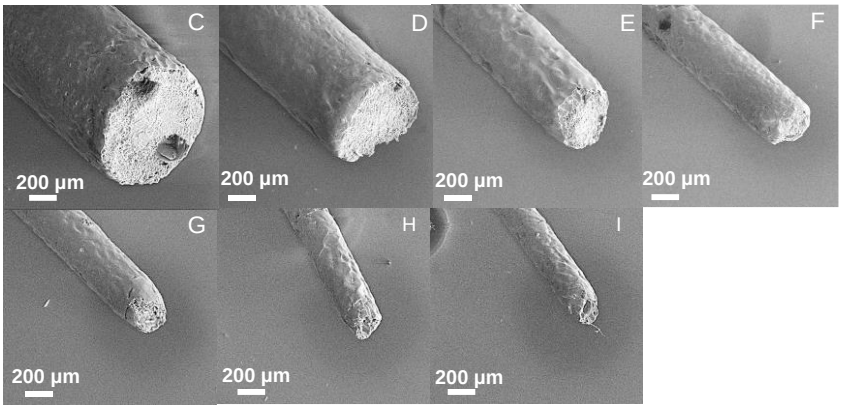

Figure 3-14 The SEM images of printed filaments at various speeds given in Table 3-4.

One would expect that by further increasing the nozzle speed, smaller features can be obtained. This trend can be continued up to the point at which the interfacial tension between the bath and the thermosetting polymer breaks up the printed filament to individual droplets, a phenomenon identified as the Plateau–Rayleigh instability, according to which liquid jets break into droplets to minimize their surface area (energy) [137]. The yield stress of the bath (σ_y, which was measured to be ~76 Pa) is the opposing force, while the interfacial tension ($\gamma_{bath-polymer}$) is the driving force for such instability. The minimum stable feature size can be estimated to be $\frac{\gamma_{bath-polymer}}{\sigma_y}$ [137]. The interfacial tension of the epoxy and the support bath is estimated using $\gamma_{water-epoxy} = \gamma_{water} + \gamma_{epoxy} - 2\sqrt{\gamma_{water}\gamma_{epoxy}}$ [138]. The minimum stable feature size for the epoxy and the aqueous bath system is estimated to be ~50 µm. By extrapolating the filament diameter vs nozzle speed, an upper limit for nozzle speed is estimated to be ~2000 mm/s (Figure 3-12c), above which the printed filament will break up to individual droplets. Such phenomenon has been recently explored for printing droplets inside a yield stress bath [137].

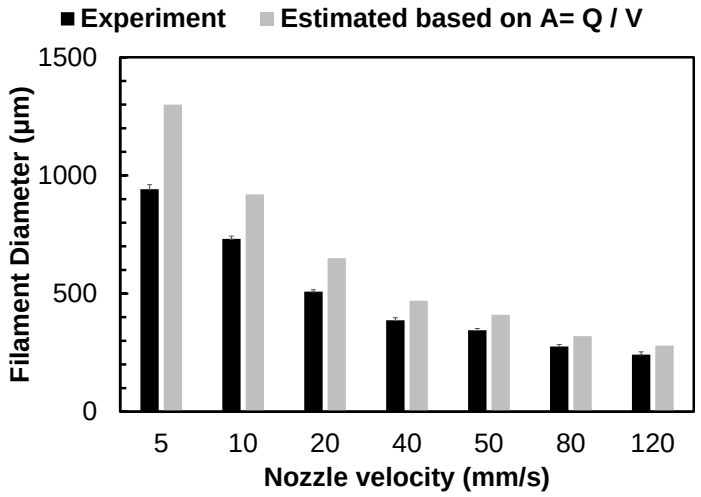

Figure 3-15 Comparison of experimentally measured filament diameter and the estimated diameter calculated from Q / V vs. nozzle speed.

The IBPC process is capable of printing with high fidelity. As a demonstration, the average angle (119.6 ± 2.8°) and the side-to-side length (15.9 ± 0.12 mm) of a honeycomb structure were measured and compared to the CAD model input to the printer (120° and 16 mm, respectively) (Figure 3-12d, e). The surface ridges on the printed part depend on the filament diameter and hence the nozzle speed (Figure 4c). For a nozzle speed of 50 mm/s and a flow rate of 0.8 mL/min, the profilometer shows surface ridges with a peak-to-valley of approximately 200 μm and an average peak-to-peak of approximately 720 μm (Figure 3-12f). Faster nozzle speeds will result in thinner filaments and, hence, smoother surface and better resolution. If the goal is to increase the volumetric print rate, variable speed pumps may be needed to increase the flow rate (Q) while the nozzle speed increases.

As the nozzle moves in the bath, it creates a crevasse behind it. As an analogy, consider cutting a gel with a knife. As opposed to conventional gels (which are often brittle), a thixotropic material will "heal" and close the crevasse after a certain time. The driving force

for the closure is the hydrostatic pressure, while the viscous force ($V\eta/d$) of the bath is the resisting force, in which V and d are the nozzle velocity and diameter, respectively, and η is the bath viscosity. The closure of the crevasse behind the nozzle will prevent the reflow of the dispensed polymer into this space. The hydrostatic pressure (ρgh) depends on the depth (h) in which the material is being printed, where ρ is the bath density. The printing depth in this study was in the range of ~2–6 cm. To evaluate the viscous force, the bath viscosity as a function of shear rate, $\dot{\gamma} = \frac{V}{d}$ was measured. (Figure 3-16a). The results show that the bath viscosity nearly linearly drops vs the shear rate, and as a result, the viscous force remains approximately constant (Figure 3-16b and Table 3-5).

Table 3-5 The measured bath viscosity and the calculated viscous force vs. nozzle speed.

Nozzle velocity V [mm/s]	Shear strain rate $\dot{\gamma} \approx \frac{V}{d}$ [1/s]	Bath viscosity η [Pa.s]	Viscous force $\frac{V.\eta}{d}$ [Pa]
5	4.17	11.83	49.29
10	8.33	6.03	50.25
20	16.67	3.06	51
40	33.33	1.49	49.67
50	41.67	1.25	52.08
80	66.67	0.78	52
120	100	0.52	52

For these experimental conditions, the printing depth was calculated, and it was found it should be more than 5 mm to ensure the closure of the crevasse behind the nozzle (Figure 3-16b). It could be observed that, in a shallow depth (<~5 mm), nozzle track marks were left on the gel, while for a larger depth, no track mark behind the nozzle could be observed in the bath (Figure 3-17).

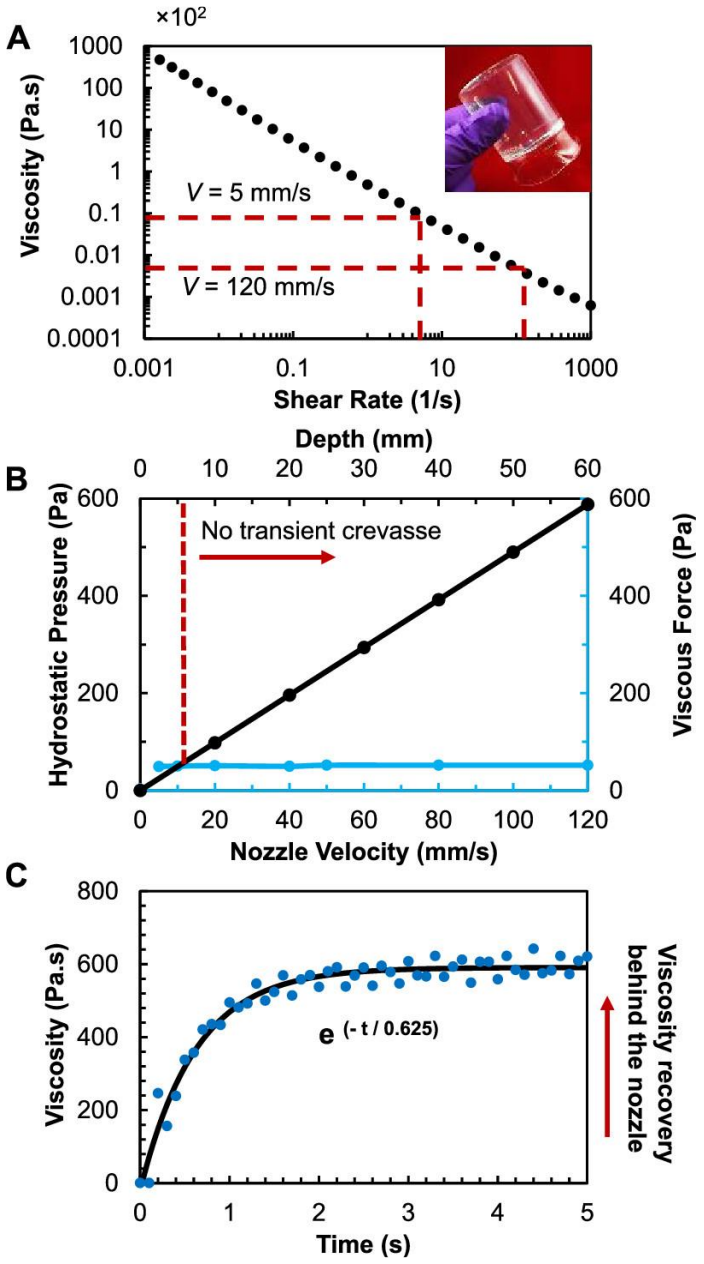

Figure 3-16 The rheological properties of the thixotropic support bath and viscous force have crucial effects on the process outcomes. (A) The viscosity vs shear rate for the thixotropic support bath. (B) The hydrostatic pressure vs bath depth and the viscous force vs nozzle velocity. The viscous force is nearly constant. (C) The buildup of the bath viscosity vs time extracted from the 3ITT. The solid line is an exponential fit.

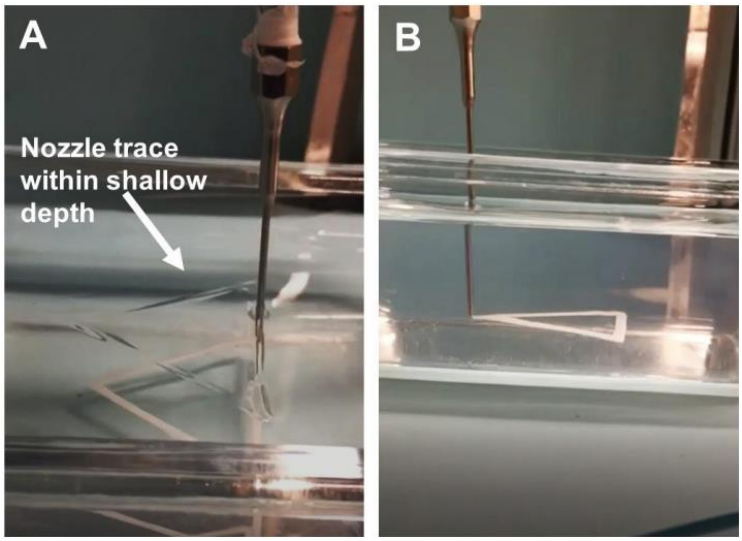

Figure 3-17 (A) and (B) top-view and side-view optical images during 3D printing. The nozzle trace can be observed in the top-view image for shallow depth, while no trace is observed for deeper depth.

The Reynolds numbers ($Re = \frac{\rho . V . d}{\eta}$) of 10–15 are often associated with the onset of turbulent flow around a moving cylinder in a fluid [139]. For the epoxy flowing through the nozzle, the Reynolds number was calculated to be $Re = 0.005$, which is well within the laminar flow range. It was calculated that the flow speed in the nozzle should increase to ~23.8 m/s for the onset of turbulent flow ($Re = 10$), which corresponds to a flow rate of over ~710 mL/min. The other relevant Re number is associated with the moving nozzle in the bath. Since the viscosity and nozzle speed have an inverse relationship, the Re number increases nonlinearly with the nozzle speed (Figure 3-18). The calculated Re number shows that at a nozzle speed of ~750 mm/s, the onset of turbulent flow in the bath resulting in a recirculating flow and unstable printing can be expected. It should be noted that the bath Re number was calculated from the experimentally measured bath viscosity vs the nozzle velocity (Table 3-5).

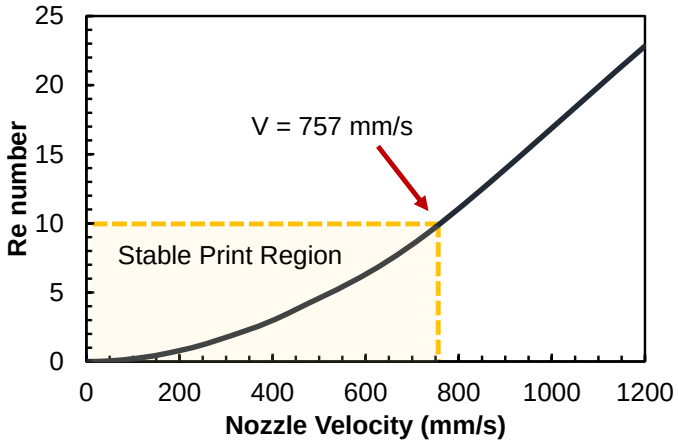

Figure 3-18 The calculated Reynolds (Re) number for the bath vs. the nozzle speed. At nozzle speed of V=575 mm/s, Re=10, which could be the onset of turbulent flow in the bath resulting in recirculating flow and unstable printing. The bath Re was calculated form the experimentally measured bath viscosity vs. the nozzle velocity.

The shear strain rate varies from ~4 to ~100 s^{-1} for the nozzle speed of 5 – 120 mm/s. This corresponds to a viscosity in the range of ~12 Pa·s down to ~0.5 Pa·s. As a comparison, the viscosity of the epoxy used in this work was ~2.2 Pa·s (21.9 P) (Figure 3-19).

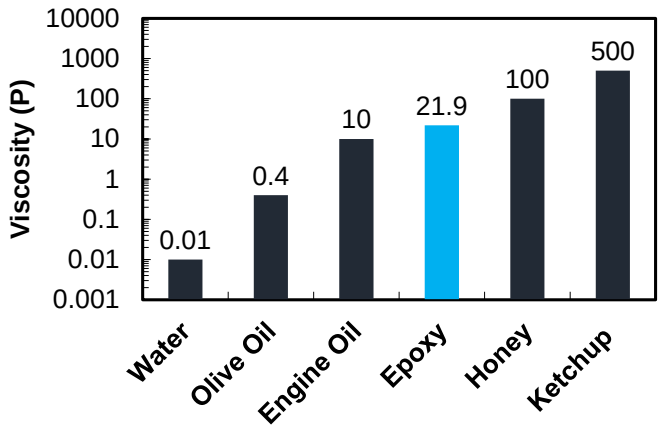

Figure 3-19 The comparison of the epoxy viscosity with other common fluids. (10 P=1 Pa.s).

A nozzle speed was in the range of ~40 – 50 mm/s for most of the printed structures, which corresponds to a shear strain rate of 30 – 40 s^{-1}, and a bath viscosity of ~1.25 – 1.5

Pa·s. To investigate the recovery of the bath viscosity behind the nozzle, the 3ITT (the three-interval thixotropic test) was performed, in which the bath was subjected to step strain rates between 0.1 and ~100 s^{-1} (Figure 3-20). The viscosity recovery vs time when the shear rate changes from ~100 to ~0.1 s^{-1} is shown in Figure 3-16c. The data are fit by an exponential function with a thixotropic time constant of $\tau = 0.625\ s$. In the wake of the nozzle, the bath viscosity quickly recovers the majority of its static viscosity (in a short time (<1 s), which is enough to maintain the geometry of the printed polymer). Additionally, this fast recovery time allows for the nozzle to return back to the same location to continue printing the subsequent layers. Laponite in water forms a three-dimensional network that results in the observed time-dependent shear-thinning/thickening behavior (thixotropic). This thixotropy is the result of the breakup and buildup of the 3D microstructure of Laponite in water. There is a time constant associated with this breakup and buildup that results in the observed time-dependent behavior.

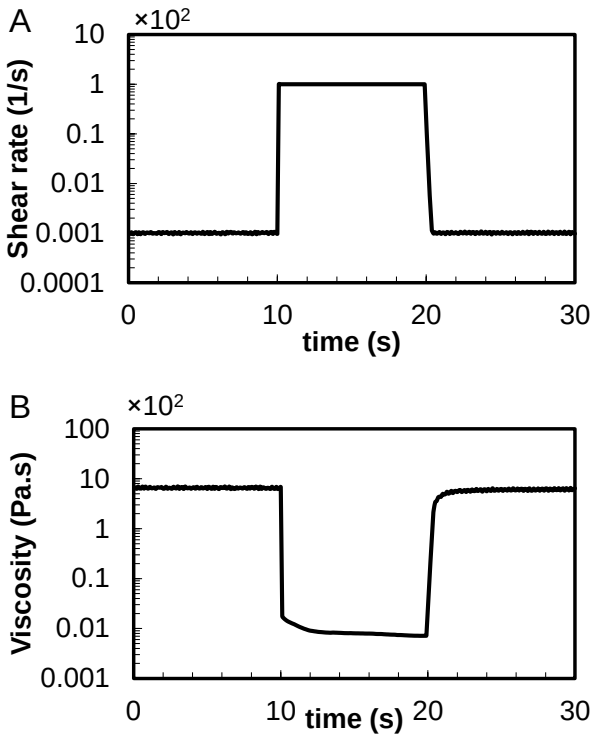

Figure 3-20 The 3ITT test, (A) shear rate versus time, (B) viscosity versus time.

During epoxy cross-linking, the epoxide group in epoxy resin reacts with the curing agent to form a highly cross-linked three-dimensional network. To investigate the thermally induced chemical reactions during the process, simultaneous differential scanning calorimetry (DSC) and thermogravimetric analysis (TGA) measurements under flowing nitrogen was performed. The exothermic peak of epoxy resin curing (cross-linking) has a peak at ~122 °C, with an onset and endpoint of 86 and 168 °C (Figure 3-21a). The second exothermic peak at ~375 °C, which is accompanied by a large drop in mass in the TGA response, is associated with degradation (thermal decomposition). The 3D-printed epoxy shows a T_g of ~92 °C. The T_g has an onset and endpoint at 77 and 107 °C, respectively (Figure 3-21b). For the cast epoxy, the T_g onset and endpoint are 87 and 136 °C, respectively (Figure 3-22). Based on the TGA

response, the cast and 3D-printed epoxy show a similar degradation (decomposition) response (Figure 3-23).

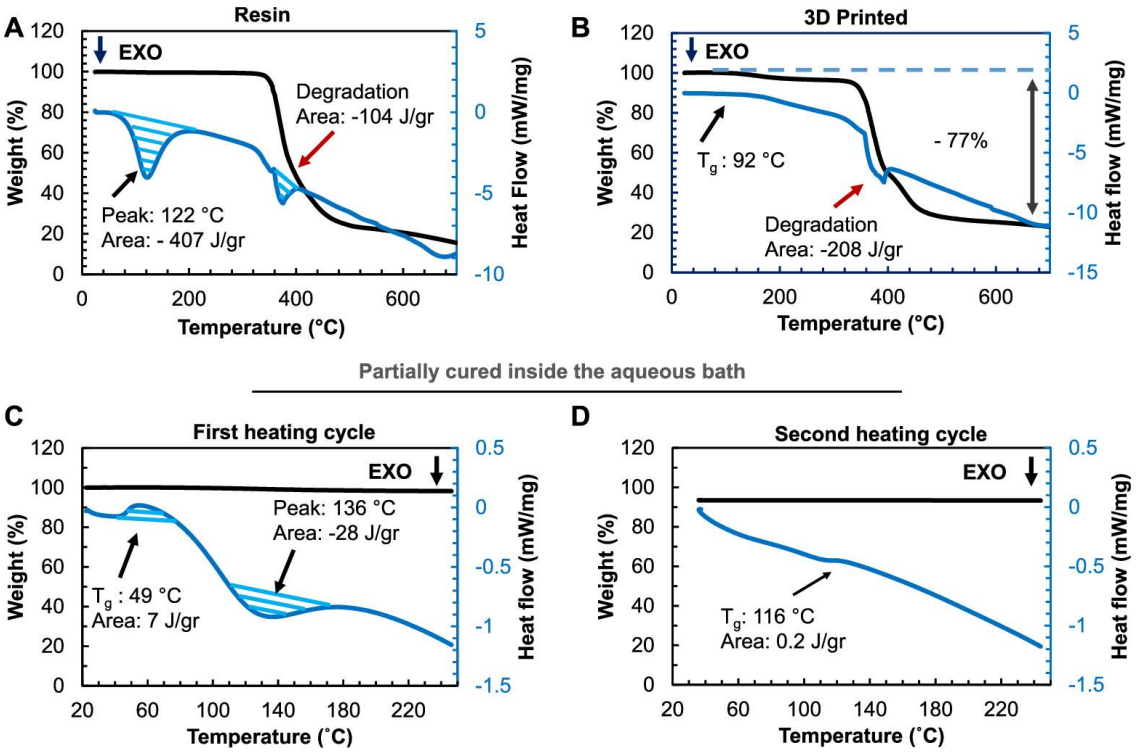

Figure 3-21 Differential scanning calorimetry (DSC) and thermal gravimetry analysis (TGA) to analyze the thermally induced chemical reactions during partial cure and full cure. (a and b) DSC/TGA responses for the resin and the 3D-printed epoxy, respectively. (c and

d) DSC/TGA responses of the partially cured epoxy inside the aqueous bath for the first and second cycles, respectively.

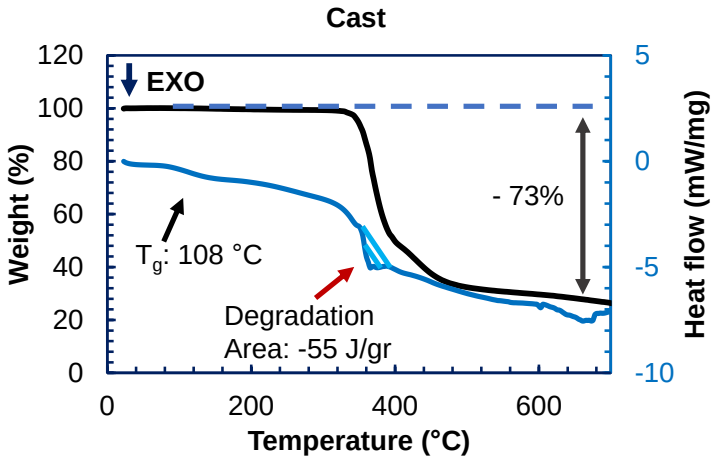

Figure 3-22 The DSC/TGA responses of the cast epoxy.

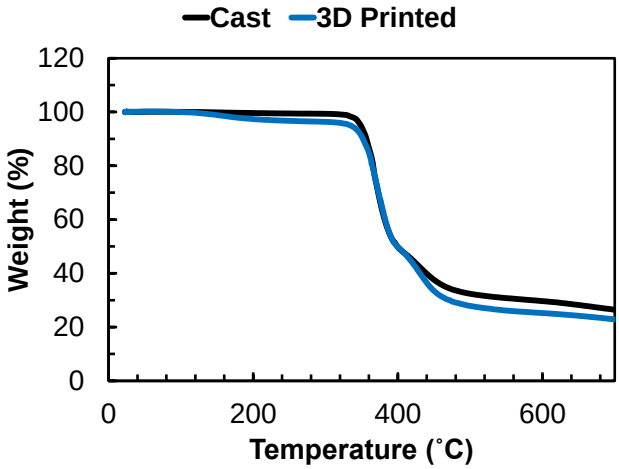

Figure 3-23 The TGA responses of the cast and 3D-printed epoxy.

In conventional processes including casting, the epoxy resin is cured in air or an inert gas environment. In this process, however, the initial partial curing was performed inside the

aqueous bath at room temperature followed by the full cure out of the bath in an oven at an elevated temperature (85 °C). To further evaluate the thermal behavior of the partially cured epoxy inside the aqueous bath, two heating cycles on this sample up to 250 °C were performed (well below the decomposition temperature). In the first heating cycle (Figure 3-21c), an endothermic peak was observed for T_g at ~49 °C, with an onset and endpoint of 41 and 55 °C, respectively. The second peak is exothermic with a peak at 136 °C and an onset and endpoint of 102 and 177 °C, respectively. This peak is associated with residual curing. In the second heating cycle (Figure 3-21d), the T_g was detected at ~116 °C. No noticeable drop in weight was detected based on the TGA data for either cycle. The results reveal that the initial partial cure at room temperature inside the bath results in a low cross-link density, and hence, the detected T_g for the first cycle is much lower than the cast epoxy. The residual cure in the first cycle results in a higher cross-link density, and consequently, the T_g increases to a value close to the cast epoxy. Only 0.5 wt. % of water evaporation was measured for the partially cured epoxy, an indication that the residual water inside the partially cured epoxy was minimal (Figure 3-24).

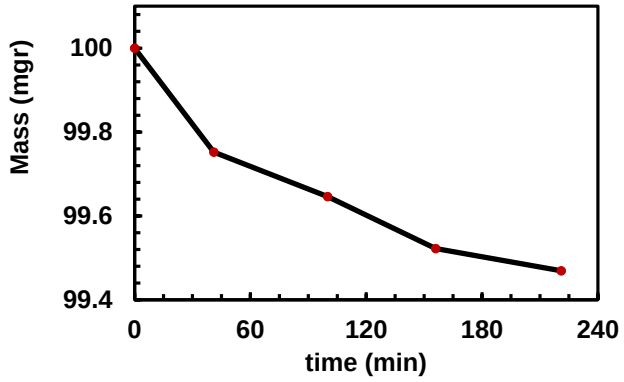

Figure 3-24 Measured mass vs. time for the partially cured epoxy indicates negligible water evaporation from the sample.

To compare the chemical composition of the printed epoxy vs the control cast epoxy, EDS (energy-dispersive X-ray spectroscopy) spectra from both the surface and the cross section of the printed epoxy was acquired. The spectra and the material composition matched the ones of the cast epoxy (Figure 3-25, Table 3-6), and no detectable traces of the Laponite were found on the printed samples.

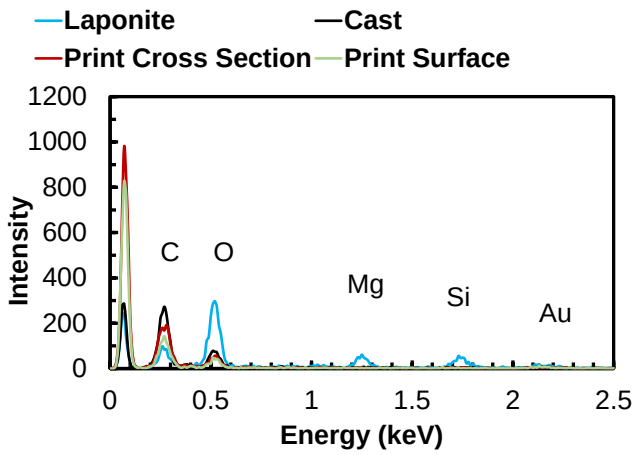

Figure 3-25 The EDS spectra of the Laponite, cast epoxy, cross-section and surface of the printed epoxy.

Table 3-6 The atomic percentage of the elements from the EDS spectra in Figure 3-25.

Element (at. %)	C	O	Mg	Si	Au
Cast	87.18	12.82	0	0	0
Print Surface	86.77	13.23	0	0	0
Print Cross Section	88.5	11.5	0	0	0
Laponite	40.71	45.75	5.48	7.01	1.06

For 3D printing of epoxy in the literature, rheology modifiers are used. In this case, the use of bath eliminates using any rheology modifiers. This is very important for achieving isotropic mechanical properties. This article also reports on the details of a two-step curing (partial curing in the bath and complete curing outside of the bath) with detailed thermal analysis. 3D printing of epoxy needs a careful choice of support bath. For the PDMS and hydrogels, often a low-yield-stress (~<10 Pa) bath is used. According to the Rayleigh instability, the minimum printable feature size depends on the ratio of the interfacial tension and the yield stress of the bath. In the preliminary experiments, it was observed that for support bath with a low yield stress (mineral-oil-based gel), the printed parts (epoxy) broke up

unless the diameter of a single filament was as high as ~3 mm. Therefore, a support bath with a high yield stress (~76 Pa) was designed to be able to achieve a better resolution. Having a transparent bath was intended for the *in-situ* monitoring of the process for subsequent research.

The support bath is designed in a way that it prevents rise or sinks of the printed part as it was seen that the parts and filaments were in place during the printing and room temperature curing. The case of single-filament printing differs from when filling a space. In the latter case, the bottom side and one side of the extruded filament are in contact with the previously printed epoxy, while the top surface and the other side surface are in touch with the bath. This top surface and the side surface come into contact with the next filaments and next layers. Since the epoxy does not cure, the interdiffusion between printed layers overall results in all sides of a filament within a space-fill print to have similar dimensions and curvature. This effect, however, will show up in the uppermost top and bottom and side layers, which essentially form the sample surface. The time-dependent shear thinning, and thickening (thixotropy) may play a role in the resolution and also surface finish of the sample. If the bath recovery time is too long, the epoxy may spread into the bath and compromise the resolution. On the other hand, the recovery time may also smoothen the surface, as the adjacent lines have enough time to merge before the bath fully recovers. There may be a trade-off between the resolution and surface smoothness of the printed object depending on the recovery time, and this deserves a full study.

Although the focus in this work has been on the effect of speed on the printing performance, it is also important to discuss the role of nozzle diameter in the printing

performance. The viscous force ($V\eta/d$) of the bath, in which η is the bath viscosity, which is the resisting force to crevasse closure, depends on the nozzle velocity (V) and nozzle diameter (d). By increasing the nozzle diameter, the viscous force would decrease. In addition, the bath viscosity is a function of the shear rate $\dot{\gamma} = \frac{V}{d}$. By increasing the nozzle speed, the shear rate would reduce, which corresponds to a higher bath viscosity. As a result, the viscous force remains approximately constant, as shown in Figure 3-16b. Therefore, theoretically, the diameter does not have a direct effect on the viscous force. This needs to be experimentally verified in future work. The nozzle diameter can also affect the volumetric flow rate (print rate). For a fixed flow rate, the larger the diameter, the smaller the nozzle speed required to achieve the same filament diameter.

To further investigate the effects of the print-bath interactions, EDS maps of a fractured surface of a tensile specimen is acquired. A 750 μm by 750 μm region is chosen to identify the elements. This large area is composed of several print layers; thus, the possible presence of any bath residue can be detected by this experiment. Figure 3-26 (A-D) shows the EDS map of a printed specimen. The EDS detector only identified gold, carbon, and oxygen which are the elements of epoxy.

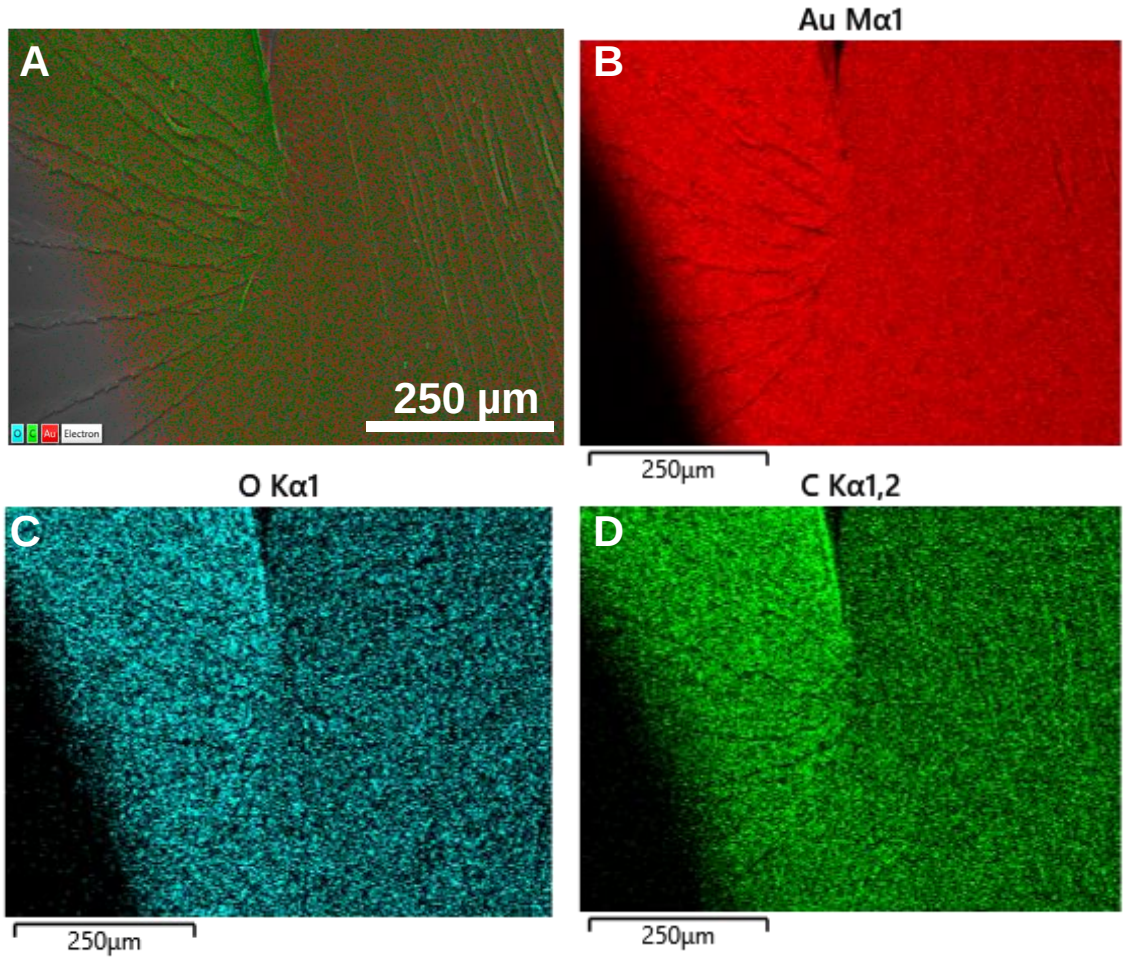

Figure 3-26 EDS map of a fractured surface of a tensile specimen. (A) the EDS layered image (B) gold, (C) oxigen, (D) carbon elements present in the epoxy sample.

3.3 Conclusion

Overall, the IBPC process overcomes several limitations facing the 3D printing of thermosetting polymers, namely, the need for rheology modifiers (for direct extrusion) or specialized chemistries (for photocurable processes), the weak interlayer interface in layer-by-layer curing, and the need to print and remove support structures. Several challenges remain: new support baths should be developed through engineering the bath microstructure and rheological properties that allow for even finer structures and faster printing speeds to be

achieved; methods for incorporation of continuous fibers in the printed material can further expand applications to load-bearing structures; and new resins and hardener chemistries can be developed for a faster cure and higher overall throughput.

4 PROCESSING AND 3D PRINTING OF POLYMER DERIVED SICN CERAMICS

Preceramic polymer resins are attractive for the 3D printing of net-shaped ceramic components. Recently various processes have been demonstrated for 3D printing of polymer-derived ceramics (PDCs). Ultimately in these processes, the process outcomes strongly depend on the process parameters. In particular, for PDCs the ceramic density, and ceramic yield are affected by the catalyst concentration and cross-linking duration. Here, thermal analysis and FTIR is used to quantify the interrelation of the process parameters on the process outcome for polysilazanes and demonstrate 3D printing of PDC components based on the best-identified process parameters. The results of this work can be used as guidelines for future additive manufacturing of PDCs.

4.1 Materials and Methods

4.1.1 Materials

A commercial polysilazane (Durazane 1800; Merck KGaA, Germany) was used as the precursor polymer to SiCN. Dicumyl peroxide (DCP) $[C_6H_5C(CH_3)_2]_2O_2$ (Sigma Aldrich) was used as the catalyst.

4.1.2 Sample Preparation

Thin circular specimens with a diameter of ~7 mm was prepared by casting the preceramic polymer into PTFE (poly(tetrafluoroethylene) molds (Figure 4-1A). The molds were made by punching out the PTFE thin sheets (thickness ~0.7 mm) and attaching them to another PTFE sheet using clips for easy specimen removal out of the mold. The sample preparation process

is schematically presented in Figure 4-1A. Four different samples were prepared by mixing the catalyst and the precursor polymer using a roller mixer for 30 min and labeled as SiCN (neat polysilazanes) and SiCN + 1, 2, 4 wt.% DCP (polysilazanes and dicumyl peroxide at 1, 2, 4 wt.% ratios).

4.1.3 Thermal Analysis

The polymer-to-ceramic transformation was investigated using simultaneous DSC/TGA equipment (STA449/F5 Netzsch). The thermal analysis was performed from room temperature up to 1000°C with a heating rate of 20°C/min in a nitrogen gas environment. In all thermal analysis experiments, the sample size was ~15 mg.

4.1.4 FT-IR Analysis

FTIR spectra were obtained using Thermo-Scientific Nicolet iS50 FT-IR Spectrometer (MA, USA) in transmission mode for solid samples.

4.1.5 3D Printing

3D printing was performed in a similar process as reported in [54]. Briefly, a support bath composed of 5 wt.% fumed silica with an average particle size in the range of ~200−300 nm (Sigma Aldrich) in 95 wt.% light mineral oil was prepared. The needle diameter used for printing was ~0.024 in. Durazane 1800 and dicumyl peroxide were mixed at the ratio of 100:1 wt.% using a roller mixer at 50 rpm for 15 min. Dicumyl peroxide is used as a catalyst to lower to the cure temperature. The solution was poured into Teflon mold and cured in an oven at 180°C for 24 h. After curing the sample was crushed into powder using a pestle and mortar. The powder was drily milled at 500 rpm for 24 h using zirconia balls with a diameter of 5 mm.

The volume of balls to powder was 2:1. The powder was then ball milled for 4 h at 500 rpm using steel balls with a diameter of 1 mm to achieve a fine powder. To increase the resin viscosity, 50 wt.% crushed cured powder was added to the preceramic polymer. After printing, the precursor polymer was cured thermally at ~180°C for 24 h inside the same bath and retrieved from the bath.

4.1.6 Pyrolysis Process

The pyrolysis process was performed using a tube furnace (Thermo Scientific Lindberg/Blue M Mini-Mite) inside a nitrogen gas environment. The pyrolysis time−temperature cycle was as following: room temperature to 450°C at 2°C/min heating rate, 450−850°C at 0.5°C/min heating rate, followed by the hold at 850°C for 1 h.

4.2 Results and Discussion

The thermal behavior of preceramic polymers is important in many manufacturing processes [54], [55], [140]. The four major reactions that occur during the thermal crosslinking of polysilazanes include hydrosilylation, vinyl polymerization, transamination, and dehydrocoupling (dehydrogenation) [68]. The hydrosilylation reaction is rather fast, and its rate can be remarkably increased using a catalyst. This reaction results in the formation of Si-C bonds, which are stable during the thermal depolymerization step. While the hydrosilylation starts at ~100–120°C, the dehydrocoupling reactions start at ~300°C. Si–Si and Si–N are formed as a result of dehydrogenation. Similar to dehydrocoupling reactions, vinyl polymerization occurs at >300°C. The vinyl polymerization involves no mass loss, while the transamination processes (200−400°C) are associated with mass loss due to the evolution of

amines, ammonia, or oligomeric silazanes [68]. Transamination results in the decrease of the nitrogen content in the ceramic upon pyrolysis.

To understand the thermal behavior of the preceramic polymer, simultaneous DSC/TGA analysis was performed. Here, the aim was to investigate the effects of the catalyst concentration on preceramic crosslinking. In the first stage, the experiments on the uncured (uncrosslinked) resin was performed to distinguish the effects of the different concentrations of the catalyst on the crosslinking temperature. Figure 4-1B shows the DSC heat flow spectra. For the pure preceramic polymer resin, crosslinking occurred in the broad range of ~100–400°C. The results showed that the addition of the catalyst significantly narrowed the crosslinking temperature range, such that the crosslinking was represented by a sharp peak (~160°C) instead of a broad range. This peak is associated with hydrosilylation, which is one of the major reactions that occur during crosslinking in polysilazanes that contains silicon hydrogen bond and the vinyl group [68]. The presence of the catalyst showed a strong increase in the hydrosilylation rate. Intensifying the hydrosilylation rate is beneficial in terms of lowering the crosslinking temperature [54]. The results additionally show that the peak of the crosslinking temperature decreases by increasing the catalyst concentration. Specifically, the DSC peak was 166, 161, and 157°C for the catalyst concentration of 1%, 2%, and 4%, respectively.

Three mass loss events were observed in TGA spectra for both pure resin and the resins containing catalyst. The first mass loss for the pure resin occurred in the range ~100–400°C, while for the resins containing catalyst the mass loss started from 100°C and stopped ~180°C. This also confirmed the role of the catalyst in lowering the crosslinking temperature. The

second major mass loss occurred at the temperature in the range of ~300–500°C. This mass loss is attributed to the dehydrocoupling reactions and transamination processes [68]. During the dehydrocoupling reaction, Si─N and Si─Si bonds were formed. In the transamination processes, the evolution of oligomeric silazanes occurred, which can decrease the nitrogen content of the final ceramic. Another important reaction that takes place at a temperature above 300°C is vinyl polymerization [141]. This process does not lead to a mass reduction. The last major mass loss step started at ~550°C and lasted up to ~800°C. This mass loss is attributed to the ceramization process. At these elevated temperatures, the crosslinked preceramic polymer resin converted to an amorphous ceramic. The results showed that the ceramic yield slightly decreased by increasing the concentration of the catalyst. Specifically, for the pure resin, the ceramic yield was 72.9%, and it decreased to 69.3% for the resin with a 4% catalyst (Figure 4-1C).

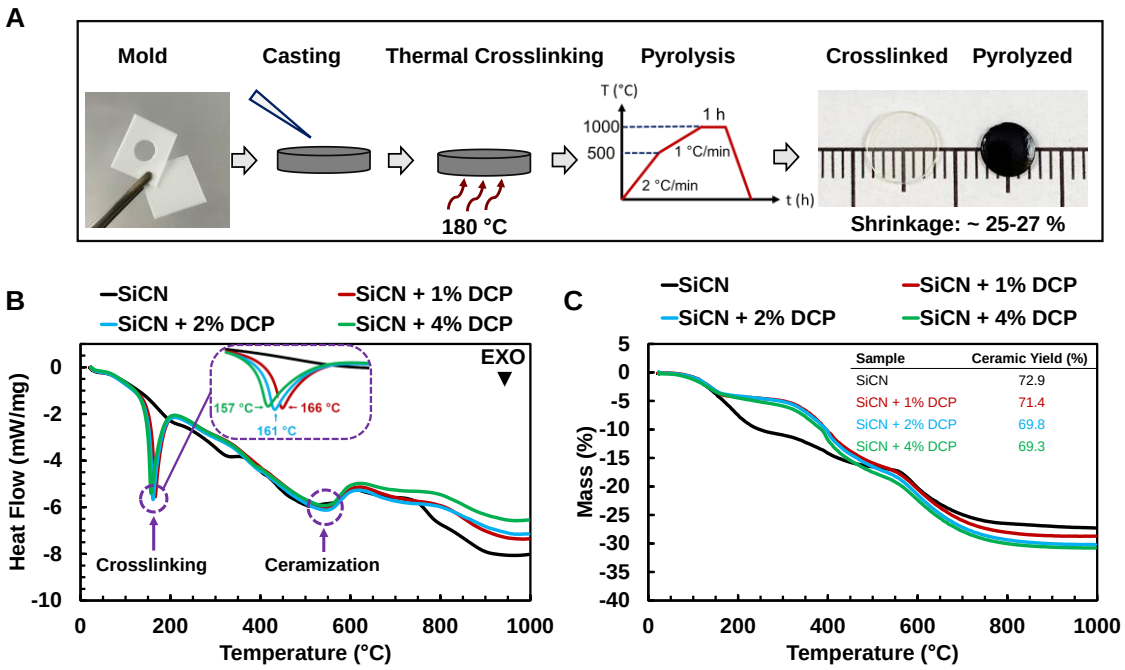

Figure 4-1 The thermal analysis of uncrosslinked SiCN resins. (A) The schematic representation of sample preparation for various experiments. (B) The differential scanning calorimetry (DSC) analysis and (C) thermogravimetric analysis (TGA) of the uncrosslinked resin with different concentrations of the catalyst.

The ceramic yield of the PDCs depends on their chemistry including the backbone structure and degree of crosslinking. To gain more insights into the effects of the catalyst concentration on the ceramic yield, thermal analysis on the crosslinked resins was performed. In these experiments, the sample had the same concentration of the catalyst as the first experiments and cross-linked them for 1-h prior to thermal analysis (Figure 4-2). For comparison, all samples were crosslinked at 180°C based on the DSC results in Figure 4-1. No indication of partial crosslinking was observed [142]. The glass transition phenomenon was observed for all resins in the temperature range of 325–344°C. Specifically, the Tg was

obtained to be 343.7°C for the pure resin. By increasing the catalyst concentration from 1% to 4%, the Tg decreased from 334.7 to 324.8°C.

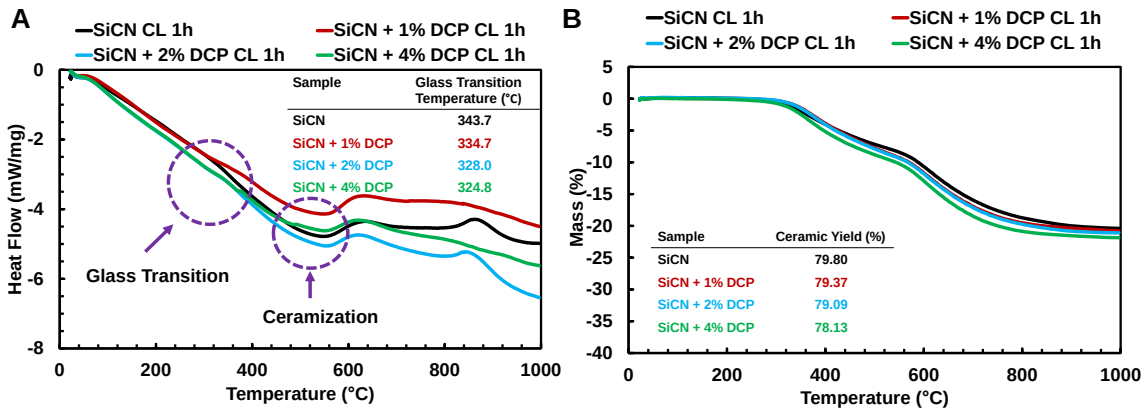

Figure 4-2 The thermal analysis of crosslinked SiCN resins. (A) Differential scanning calorimetry (DSC) and (B) TGA of the uncrosslinked resin with different concentrations of the catalyst.

The TGA results confirmed that the crosslinking process occurred as the resins did not go through a mass loss up to a temperature of ~320°C, which indicates that the hydrosilylation reactions were performed completely. A similar trend of mass loss was observed for all resins. Similar to the uncrosslinked resins, an increase in the catalyst concentration caused a slight decrease in ceramic yield. Specifically, the ceramic yield was decreased from 79.8% to 78.13%, for the pure resin and the resin with 4% catalyst, respectively. However, the initially crosslinking step (~1 h at 180°C) increased the overall ceramic yield for all samples by ~10%.

Table 4-1 The ceramic yield of the resins with different catalyst concentration for various cross-linking duration.

Sample	Ceramic Yield (%)			
	Uncrosslinked	Crosslinked		
		1 h	4 h	24 h
SiCN	72.9	79.80	83.17	86.06
SiCN + 1% DCP	71.4	79.37	81.30	85.25
SiCN + 2% DCP	69.8	79.09	80.04	84.49
SiCN + 4% DCP	69.3	78.13	80.62	84.48

Table 4-2 The glass transition temperature of the resins with different catalyst concentration for various cross-linking duration.

	Glass Transition Temperature (°C)		
	1 h	4 h	24 h
SiCN	343.7	362.0	380.8
SiCN + 1% DCP	334.7	352.0	375.5
SiCN + 2% DCP	328.0	347.8	354.2
SiCN + 4% DCP	324.8	331.4	343.5

Table 4-3 The density of the pyrolyzed ceramic from the resins with different catalyst concentration for various cross-linking duration.

Sample	Density (g/cm^3)		
	1 h	4 h	24 h
SiCN	2.04	2.17	2.29
SiCN + 1% DCP	2.00	2.14	2.23
SiCN + 2% DCP	1.94	2.10	2.10
SiCN + 4% DCP	1.92	2.01	2.10

To investigate the effects of crosslinking duration on the ceramic yield, the glass transition temperature, and the density of the pyrolyzed resins,[69], [143] thermal analysis

experiments on the resins crosslinked for 1, 4, and 24 h with the identical conditions to the previous experiments were performed. Detailed results are presented in Table 4-1, Table 4-2, Table 4-3, and Figure 4-3. Several observations were made. The highest ceramic yield was obtained for 24-h crosslinking, regardless of the catalyst concentration (Figure 4-3A). The highest ceramic yield (~86%) was obtained for the crosslinked resin without any catalyst. The lowest ceramic yield was obtained for the uncrosslinked resin with a 4% catalyst (~69.3%). Overall, the lowest ceramic yield was obtained for the resins without prior thermal crosslinking, regardless of the catalyst concentration, which emphasizes the effect of crosslinking on constraining the mobility of low molecular weight chains.

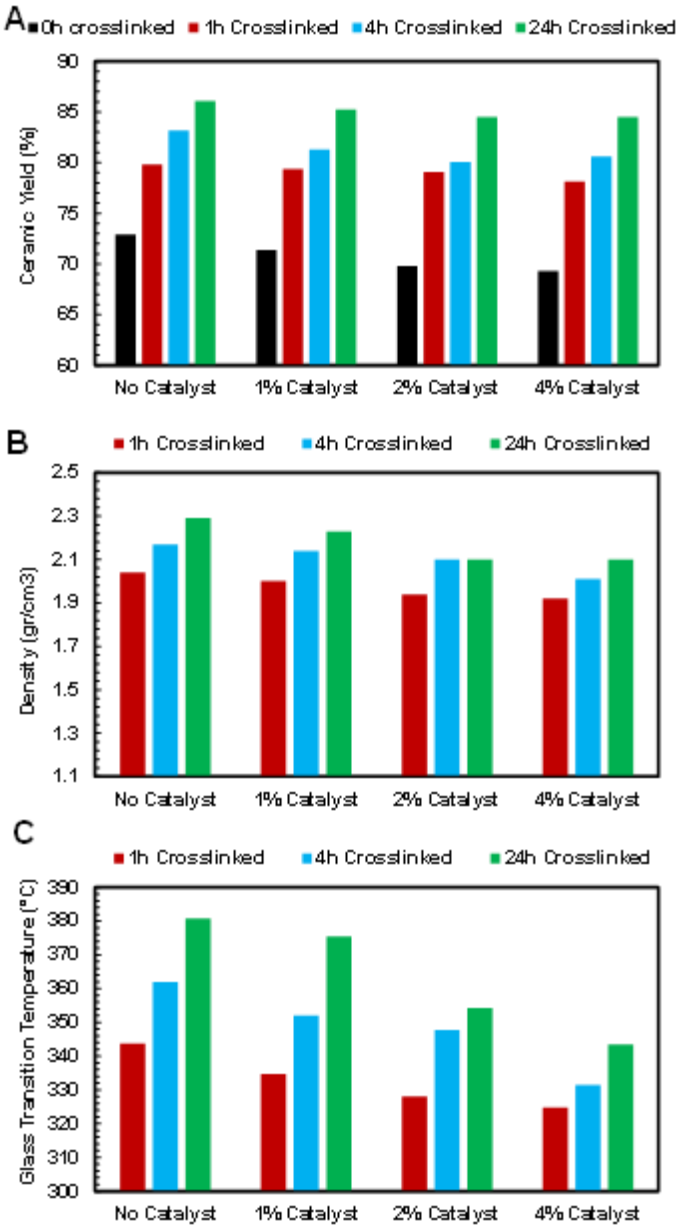

Figure 4-3 The (A) ceramic yield, (B) density, and (C) glass transition temperature of the resins with different catalyst concentrations for various crosslinking durations.

Similarly, the pyrolyzed resins that were crosslinked for 24-h had the highest density (2.1–2.29 g/cm^3), while the resins that were crosslinked for only 1 h had the lowest density (1.92–

2.04 g/cm^3), Figure 4-3B. The glass transition temperature, which is an indication of the required energy for the amorphous material to transition from a solid-state to a rubbery state, showed a similar trend to the ceramic yield and density, Figure 4-3C.

The density measurements and glass transition temperature also confirmed the full curing of the samples crosslinked for 24 h. The results match with the measurements done by [143].

In order to further analyze the effects of catalyst concentration and crosslinking duration on the resins, FTIR analysis was performed. To assess the effect of catalyst concentration, FTIR spectra were collected on the resin before crosslinking, and after 1-h of crosslinking with different amounts of catalyst (DCP) 0%, 1%, 2%, and 4% (Figure 4-4A). The peaks were assigned based on the previous report [144]. The absorption bands at 3380 cm^{-1} and 2160–2120 cm^{-1} represent the bonds for the N─H and Si─H functional groups, respectively. These major peaks all reduced in intensity with increasing the amount of catalyst, which is an indication of crosslinking according to Equations (2)–(4). The crosslinking mechanism involves the following main reactions [141]: Based on the observed reactions dehydrogenation happens. However theoretically, given that the dicumyl peroxide was added as catalyst the released hydrogens can react with the catalyst and condensation occurs.

To have a complete polymerization is it more preferable to have the reaction number 3 so that the polymeric chain always reactive for continuous polymerization.

$$\cdots Si - H + H - Si \cdots \rightarrow \cdots Si - Si \cdots + H_{2\,(g)} \quad (2)$$

$$\cdots Si - H + H - N \cdots \rightarrow \cdots Si - N \cdots + H_{2\,(g)} \quad (3)$$

$$\cdots Si - H + H_2C = CH - Si \cdots \rightarrow \cdots Si - CH_2 - CH_2 - Si \cdots \quad (4)$$

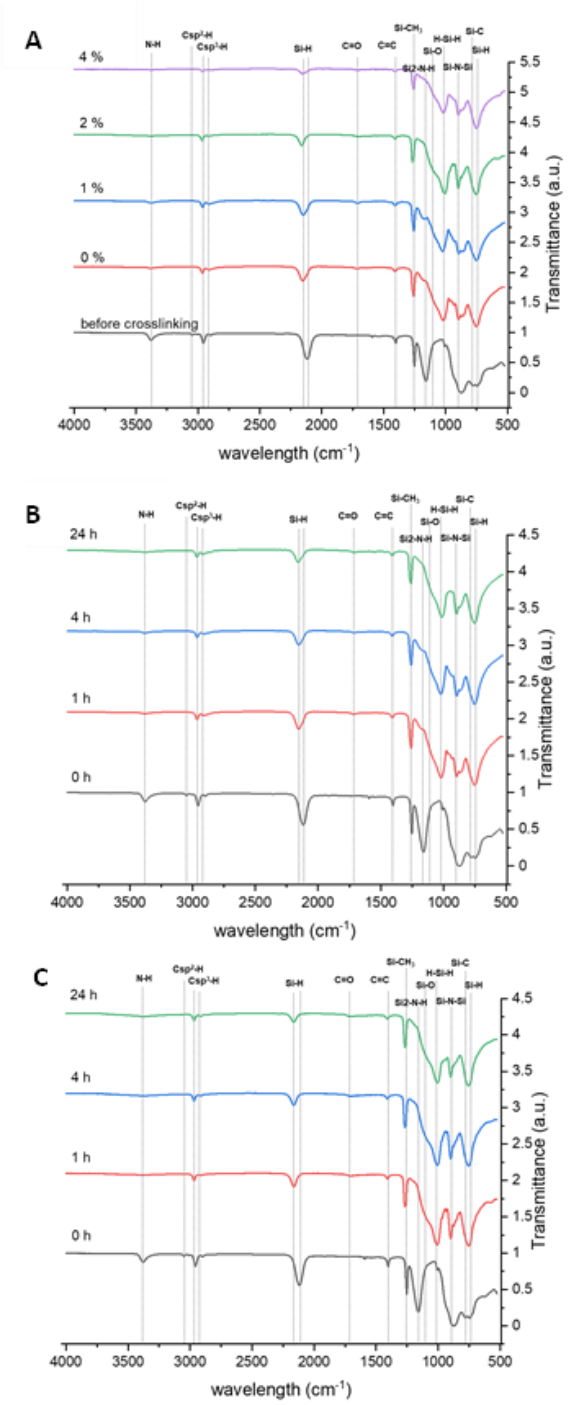

Figure 4-4 (A) FTIR spectra before crosslinking (black), and after 1 hour of curing with varying amounts of catalyst (DCP) 0%, 1%, 2%, and 4%. (B) FTIR spectra without catalyst (DCP) after 0, 1, 4, 24 h of curing. (C) FTIR spectra with 2% catalyst (DCP) after 0, 1, 4, 24 h of curing.

The peaks at 2120–2160 cm^{-1} for Si−H and the peak at 3380 cm^{-1} for N─H reduced more significantly when there was a larger amount of DCP, while the peaks at 1400 cm^{-1} for C=C have also become smoother. The sp^2 carbon vibration peak at 3149 cm^{-1} has smoothened out after crosslinking. This indicates the above reactions resulted in a higher degree of crosslinking as there was more amount of DCP after 1-h reaction. The C=O band around 1718 cm^{-1} slightly appeared after reaction and is attributed to the adsorbed CO_2 onto the surface of the specimen and inclusion in the backbone structure. The Si─O absorption band also slightly appeared as a blunt shoulder around 1100 cm^{-1} because of the slight oxidation curing in an air atmosphere.

Additionally, to assess the effects of the crosslinking duration, FTIR spectra were collected on resins without any catalyst after 0, 1, 4, 24 h of crosslinking (Figure 4-4B). The absorption bands at 3380 cm^{-1} and 2160–2120 cm^{-1} represent the bonds for the N─H and Si─H functional groups, respectively. Both peaks gradually reduced in intensity with increasing the curing duration. The N–H peak became smoother after 24 h, which indicates reaction according to Equation (4) has been processed to minimize the reactant N─H within 24 h. When 2% catalyst was added to the resins, the FTIR results showed that N─H and Si─H bands reduced in intensity faster compared to the case without catalyst (Figure 4-4C). The N─H peak became smoother after 1 h, which indicates Equation (4) has processed to minimize the reactant N─H yield within 1 h, faster than the case without catalyst (Figure 4-4B)

The FTIR results indicated that the mechanism of increased curing with dicumyl peroxide is a thermal hydrosilylation effect making the dicumyl peroxide a catalyst in this system because it initiated the free radical and does not end up in the final structure. It is initiated by the abstraction of hydrogen from perhydropolysilazane via thermal activation to

form highly reactive silicon radical species (Figure 4-5A). The crosslinked network is formed through propagation (Figure 5B). Anti-Markovnikov addition of an alkene by the silicon radical yields a covalent Si─C bond with carbon radical (Figure 4-5B, step 1). Subsequent saturation of the alkyl chain is achieved by the abstraction of an additional hydrogen atom from another silicon, thereby propagating the chain reaction (Figure 4-5B, step 2). This active silicone radical can either react with perhydropolysilazane and propagate the chain (Figure 4-5B, step 3), or it can react with another Durazane (Figure 4-5B, step 4) and finally form an active silicon radical (Figure 4-5B, step 5).

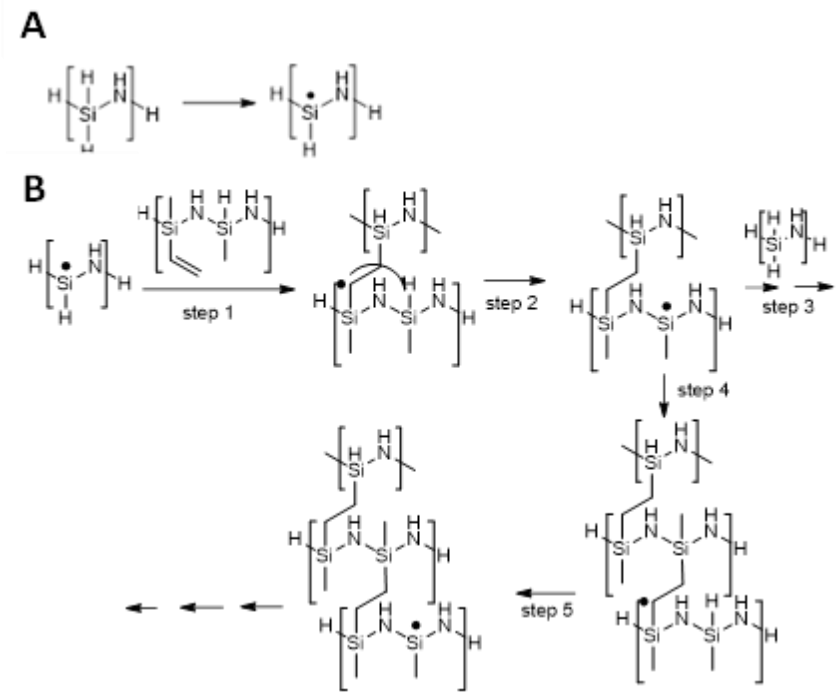

Figure 4-5 (A,B) Thermal hydrosilylation mechanism in the presence of dicumyl peroxide followed by initiation and propagation.

Based on the above DSC/TGA and FTIR analysis, the following parameters for 3D printing were recommended: 1 wt.% catalyst, crosslinking at 180°C for 24 hours. The addition of a catalyst is necessary to narrow down the crosslinking temperature, as, for the pure preceramic polymer resin, crosslinking occurs in the broad range of ~100–400°C. The minimum amount of catalyst concentration investigated in this work (1%) was chosen for printing since the addition of more catalyst did not prove to have a significant positive effect on the ceramic yield or density. Also, both the thermal analysis and FTIR results clearly indicate that 24-h crosslinking is needed for full curing to occur, with the highest ceramic yield.

For 3D printing, a recently reported method based on extrusion of the preceramic polymer into a thixotropic bath was followed [54], [142]. Briefly, in this process, 3D printing is enabled by dispensing the preceramic polymer at the tip of a moving nozzle into a bath that can reversibly switch between fluid and solid states, and the subsequent thermal crosslinking of the printed part at once inside the bath (Figure 4-6A). The bath converts to fluid at the tip of the moving nozzle, allows the preceramic polymer to be dispensed, and quickly returns to a solid-state to maintain the geometry of the printed polymer both during printing and the subsequent high-temperature (180°C) crosslinking (Figure 4-6B, C, and E). The last step in the process is the pyrolysis of the retrieved crosslinked resin to obtain ceramic parts (Figure 4-6D, and F). A piece of pyrolyzed 3D-printed ceramic held next to a 1900°C flame is shown in Figure 4-6G.

Figure 4-6 Several 3D printed SiCN components. (A) Schematic representation of the 3D printing process. (B) Parts after printing inside the bath. (C) and (E) parts after curing, (D) and (F) parts after pyrolysis. (G) A piece of the pyrolyzed sample held next to a 1900°C flame.

Based on this method a Newtonian preceramic polymer is dispensed into a non-Newtonian support bath. One issue that arose during 3D printing was the rise of the dispensed preceramic polymer in the wake formed behind the nozzle leading to the formation of stretched oval cross-sections preventing successfully printing of the intended geometries. This issue comes from the very low viscosity of the preceramic polymer, which was ~4 mPa.s (note that the viscosity of water is 1 mPa.s). The viscosity is a measure of a fluid resistance to flow. The lower the viscosity, the easier the fluid moves. The very low viscosity of the preceramic polymer made it flow up in the gap behind the nozzle before the bath fully recovers to its rest viscosity (>100 Pa.s) (Figure 4-7).

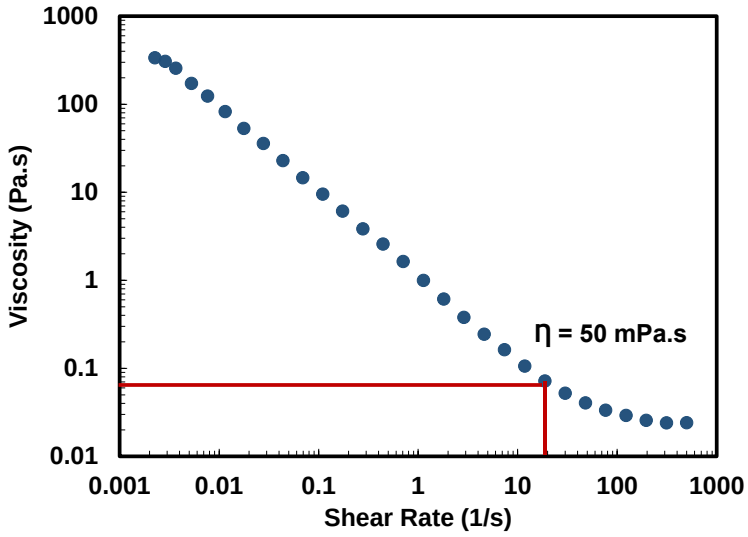

Figure 4-7 Viscosity of the support bath vs. shear rate; Viscosity curve shows a shear-thinning behavior. The viscosity of the support bath as the nozzle moves at the printing speed drops to 50 mPa.s.

3D printing was performed using a needle with an outer diameter of 0.9 mm at a printing rate of 15 mm/s. The viscosity of the bath drops to ~50 mPa.s at the associated shear rate of ~16 S^{-1} ($\dot{\gamma} = \frac{V}{d}$ where V is the nozzle speed and d is the nozzle diameter). To overcome this issue, casted samples were prepared as described earlier. Briefly, 1 wt. % catalyst was added to the preceramic polymer and cured it in an oven at 180°C for 24 h followed by crushing the sample to a fine powder using a ball mill. The fine powder was added to the preceramic polymer at 50 wt.% ratio [145]. In this way, the viscosity was increased to ~7 Pa.s keeping it a Newtonian fluid (Figure 4-8A,B). This approach helped to increase the viscosity of the resin and print successfully.

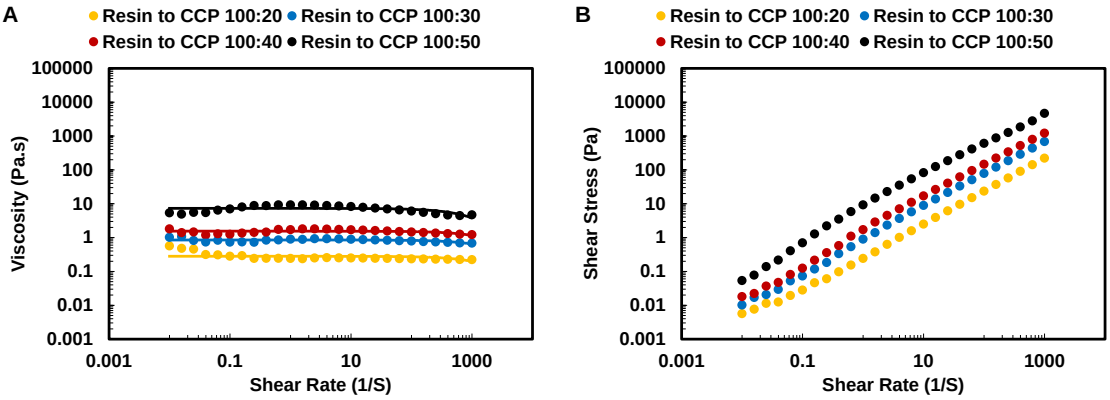

Figure 4-8 The rheological properties of the preceramic polymer at different ratios of the crushed cured powder (CCP). (A) Viscosity vs shear rate and (B) shear stress versus shear rate both show Newtonian behavior.

To investigate the effects of the addition of the crushed cured powder to the preceramic polymer on the ceramic yield, thermal analysis on the new resin was performed. In the first experiment, thermal analysis was performed on the uncrosslinked resin while in the second experiment, the thermal analysis was done on the crosslinked samples at 180°C for 24 h. DCS experiment on the uncrosslinked resin shows a sharp peak associated with crosslinking temperature ~168°C (Figure 4-9A). It shows that the addition of the crushed powder does not change the crosslinking temperature. Since the crushed cured powder was added to the preceramic polymer, both uncrosslinked and crosslinked samples show a glass transition ~311 and 380°C, respectively. The crosslinked sample shows a higher ceramic yield compared to the uncrosslinked sample because crosslinking process prevents the loss and fragmentation of low molecular weight parts of the precursor polymer during ceramization However, the addition of the crushed cured powder to the preceramic polymer shows a slight reduction in ceramic yield, ~2%.

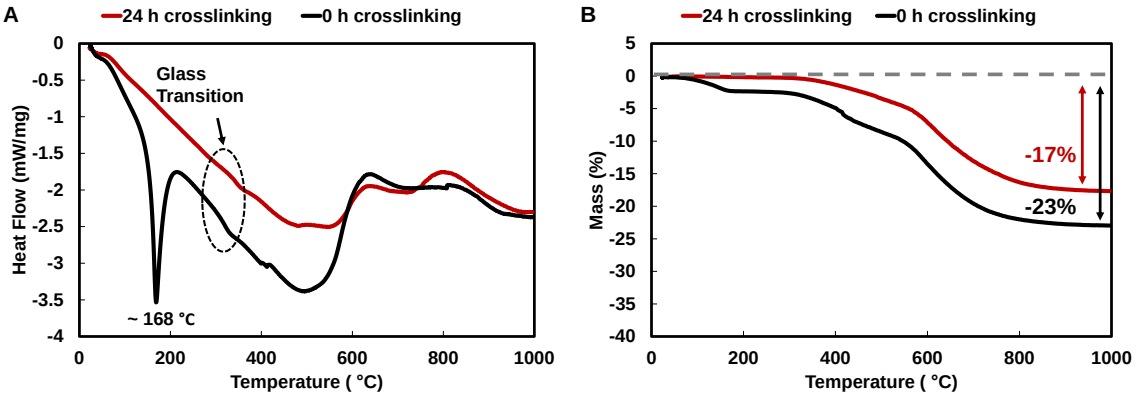

Figure 4-9 The thermal analysis of the uncrosslinked and crosslinked SiCN resins with the addition of the crushed cured powder. (A) Differential scanning calorimetry (DSC) and (B) Thermogravimetric analysis (TGA).

In the last experiment, to evaluate the ceramic yield of the printed parts, thermal analysis on the 3D printed samples was performed. After 3D printing, the samples were cured at 180°C for 24 h in the same bath. The retrieved samples were rigid enough to be taken out of the bath. Initially, the thermal analysis was performed on the 3D printed samples. The TGA result showed that the ceramic yield of the 3D printed sample was ~53% (Figure 4-10). It was an indication of partially curing of the 3D printed samples. To achieve full curing, the 3D printed samples were reheated with the same conditions as the first heating. For the last experiment, the thermal analysis was performed on 3D printed samples that were reheated in the air after taking them out from the bath. The TGA results show that the second heating cycle increased the ceramic yield of the 3D printed sample to 76%. The density of the 3D printed sample was measured ~2.05 gr/cm^3. Overall, the selected parameters of 1 wt.% catalyst, crosslinking at 180°C for 24 h results in good quality prints. The pyrolysis step may require further analysis and modification to prevent cracking of the printed structures (Figure 4-6D).

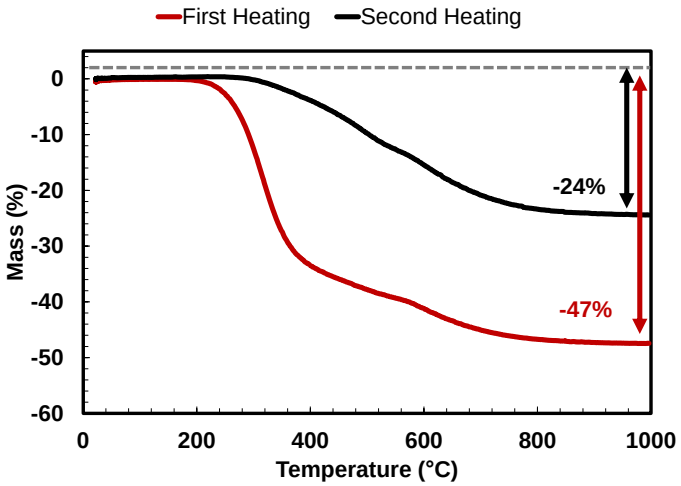

Figure 4-10 The thermal analysis of the uncrosslinked and crosslinked SiCN resins with the addition of the crushed cured powder.

4.3 Conclusion

The results showed that the addition of the catalyst significantly narrowed the crosslinking temperature range of the polysilazanes, such that the crosslinking was represented by a sharp peak instead of a broad range. The presence of the catalyst showed a strong increase in the hydrosilylation rate. The results additionally showed that the peak of the crosslinking temperature decreases by increasing the catalyst concentration. The ceramic yield slightly decreased by increasing the concentration of the catalyst. The highest ceramic yield was obtained for 24-h crosslinking, regardless of the catalyst concentration. The highest ceramic yield (~86%) was obtained for the crosslinked resin without any catalyst. The lowest ceramic yield was obtained for the uncrosslinked resin with a 4% catalyst (~69.3%). Overall, the lowest ceramic yield was obtained for the resins without prior thermal crosslinking, regardless of the catalyst concentration, which emphasizes the effect of crosslinking on constraining the

mobility of low molecular weight chains. Similarly, the pyrolyzed resins that were crosslinked for 24-h had the highest density (2.1–2.29 g/cm^3), while the resins that were crosslinked for only 1 h had the lowest density (1.92–2.04 g/cm^3). Based on the above DSC/TGA and FTIR analysis, the following parameters for 3D printing were recommended: 1 wt.% catalyst, 50 wt.% crushed cured powder, crosslinking at 180°C for 24 h, reheating with the same conditions after part removal from the bath in air.

5 TOWARD LOW-ENERGY MANUFACTURING AND SELF-HEALING OF CO-CONTINUOUS METAL-CERAMIC COMPOSITES

The concept of self-healing materials, mainly inspired from biological systems, in last several decades has been pursued toward fully autonomous materials and structures. Self-healing for polymers (extensively) and metals (to much less extent) have been demonstrated, however, there are no such reports for metal-ceramic composites. Metal-ceramic composites are technologically significant as structural and functional materials and are among the most expensive materials to manufacture and repair. Hence, technologies for self-healing metal-ceramic composites are of paramount importance. Here, a concept is demonstrated to fabricate and heal co-continuous metal-ceramic composites at room temperature. The composites are fabricated by infiltration of metal (here Copper) into a porous alumina preform (fabricated by freeze-casting) through electroplating; a low-temperature and low-cost (by ~ 60-times lower cost compared to traditional molten metal infiltration) process for fabrication of such composites. Additionally, the same electroplating process is demonstrated for healing damages such as grooves and cracks in the original composite, such that the healed composite recovers its strength by more than 80%. Such technology may be expanded toward fully autonomous self-healing structures.

5.1 Materials and Methods

5.1.1 Material Preparation

Ceramic platelets (117751, Rona Flair White Sapphire) were kindly provided by Merck KGaA, Darmstadt, Germany. Alginate (Protanal LF10/60FT) was purchased from FMC

Corporation. Fumed colloidal silica (silica ≥ 99%, average diameter of 12 nm, Strem Chemical Inc.) was purchased from VWR. TAC (Ammonium citrate tribasic) was purchased from Sigma Aldrich. Copper plating electrolyte was purchased from Transene company Inc.

5.1.2 Ceramic slurry preparation

A 20 vol.% aqueous ceramic slurry was prepared using the following ratios: the alumina to alginate ratio was 100:3 wt.%, the alumina to fumed colloidal silica ratio was 100:12 wt.%, and the ratio of powder to TAC was 100:0.4 wt.%. The slurry was prepared in the following steps. First the TAC was added to DI water and mixed using a magnetic stirrer at 400 RPM for one hour until all powder completely dissolved. Alumina and silica were mixed and divided into five equal containers. All containers were incrementally added to the TAC/DI water solution and mixed using a planetary ball mill at 500 RPM for 30 minutes. To prevent breakage of the microplatelets, no balls were used during ball milling. Finally, the ceramic slurry was mixed with the same RPM for 12 h to have a homogeneous ceramic slurry. The pH value of the ceramic slurry was ~7.5. To obtain a stable ceramic slurry, the pH value was modified using HCL (hydrochloric acid) to ~5.

5.1.3 Freeze casting

A mold containing acrylic walls with a copper bottom plate was made for the unidirectional freeze-casting. The ceramic slurry was poured into the mold and the mold was placed on the cold finger of a homemade freeze-casting setup. The bottom end of the cold finger was submerged into a liquid nitrogen flask. The dimensions of the mold were 150 mm × 150 mm × 50 mm. To make a large plate of ceramic preform, the slurry was poured to the depth of ~3 mm. After freeze-casting process, the walls of the mold were disassembled while on the cold

finger. The frozen plate was cut into ~ 50 mm × 50 mm samples (the thickness of the samples was ~3 mm) using a sharp razor blade. All samples were freeze-dried in a Labconco FreeZone 2.5 freeze drier for at least 48h.

5.1.4 Sintering

The freeze-dried ceramic plates were heated in a ST-1700C-445 (Sentro Tech) high temperature box furnace in air environment. The heating process had two steps, a binder burnout step to remove the alginate and a sintering step to transform the green body into solid ceramic. The heating program was as follows: room temperature to 600 °C at 1 °C/min; holding at 600 °C for 3 h; from 600 °C to 1600 °C at 1 °C/min; holding at 1600 °C for 4 h; from 1600 °C to room temperature at 5 °C.

5.1.5 Calculations of density and porosity

To estimate the porosity, reference [146] was followed. For alumina, silica, and copper density values of $3.98,\ 2.19, and\ 8.96\ \frac{gr}{cm^3}$ were used, respectively. The density of the composite was calculated to $3.77\ \frac{gr}{cm^3}$. The estimations showed that the composite had a ceramic phase of $24\ vol\%$, metal phase of $66\ vol\%$, and porosity of $10\ vol\%$.

5.1.6 Estimation of energy consumption during the process

A VersaSTAT-4 Potentiostat/Galvanostat (Princeton Applied Research) controlled the electrochemical cell by applying a constant current (– 69 mA). The power was estimated using $P = U \times I = 0.052 \times 0.069 = 0.0036\ W$, where U was the average potential, and I, was the constant current. The energy was obtained using $E = P \times t = 0.0036 \times 3600 \times 24 \times$

$10 = 3110.4\,J$. The specific energy was obtained by dividing the energy by the mass of the deposited copper (in this case $4.89\ gr$) and was $636\,\frac{J}{gr}$. The energy density was obtained by dividing the energy by the volume of the deposited copper (in this case $0.55\ cm^3$) and was $5.6\ \frac{kJ}{cm^3}$. To calculate the energy consumption for healing a crack, the energy to heal a crack was divided by the length of the crack for each specimen.

5.1.7 Mechanical characterization

Three-point flexural experiments were chosen to study the mechanical properties of the composite beams using an MTI/Fullam SEMTester (MTI Instruments, Inc). The span length of the samples was 9.8 mm. The samples were cut into 1 mm × 1 mm × 15 mm beams. The crosshead displacement rate was 0.1 mm/min. A 5 lb loadcell was used to capture load-displacement response in mechanical experiments. Equations below were used to calculate flexural stress and strain respectively:

$$\boldsymbol{\sigma_f = \frac{3Fl}{2bd^2}} \tag{5}$$

$$\boldsymbol{\epsilon_f = \frac{6Dd}{l^2}} \tag{6}$$

where *F* is force, *l* is the span length, *b* and *d* are the width and thickness of the beams, and *D* is the displacement.

5.1.8 Characterization of rheological properties

The rheological measurements were performed using an Anton Paar rheometer using a 50-mm upper cone with an angle of 0.5° and a 50-mm in diameter lower plate. The viscosity of the ceramic slurry was determined by applying a shear rate sweep from 1000 S^{-1} to 10^{-1} S^{-1}.

5.1.9 Scanning electron microscopy

SEM imaging of the ceramic scaffolds and composite beams was performed using a Zeiss Supra 40 SEM. For ceramic preform, samples were coated with gold-palladium to enhance their electrical conductivity for SEM imaging. The metal-ceramic composite was mostly conductive enough to be imaged without any metal coating.

5.1.10 Nanoindentation experiments

A NanoFlip Nanoindenter (nanomechanics Inc.) equipped with a Berkovich tip was utilized to perform the nanoindentation experiments. The indentation experiments were run in load-control mode. The maximum load was set to 45 mN and the strain rate was set to 0.05 1/s. Each indentation had three stages: loading, holding at maximum load for one second, and unloading. The continuous stiffness measurement (CSM) technique was used to determine the hardness and elastic modulus of the specimen as a function of indentation depth [147]. An array of 9 by 25 indentations was performed on the healed samples starting from the metal part to the composite region of the sample.

5.2 Results and Discussion

The manufacturing process starts with preparation of an aqueous ceramic slurry as previously reported [146]. Details are presented in the materials and method section. Briefly, a 20 vol.% solids loading ceramic slurry was prepared by dissolving TAC (ammonium citrate tribasic) as the dispersant in DI (deionized) water. The role of dispersant is crucial in preventing agglomerations by controlling the interparticle forces influencing the stability of the ceramic slurry. Next, alginate was added to this slurry as a binder to temporarily strengthen the green body during freeze-drying. In the slurry, alumina microplatelets were used with a mean diameter and thickness of ~ 6 μm and 500 nm, respectively. In the next step, the alumina microplatelets and silica nanopowder were incrementally added (~ 12 nm average diameter) to the slurry and mixed using a planetary ball mill. This incremental addition of the powder helped in having a more homogeneous ceramic slurry. The rheology measurement of the ceramic slurry showed a shear thinning behavior, which is a characteristic of a stable slurry (Figure 5-1). Then, the ceramic slurry was poured into a large mold. The mold was placed on the cold finger of a home-built freeze-casting setup. The other end of the cold finger was submerged in liquid nitrogen. After freeze-casting, the large thin sheet was cut into several 50 mm by 50 mm sheets, and they all were freeze-dried at once.

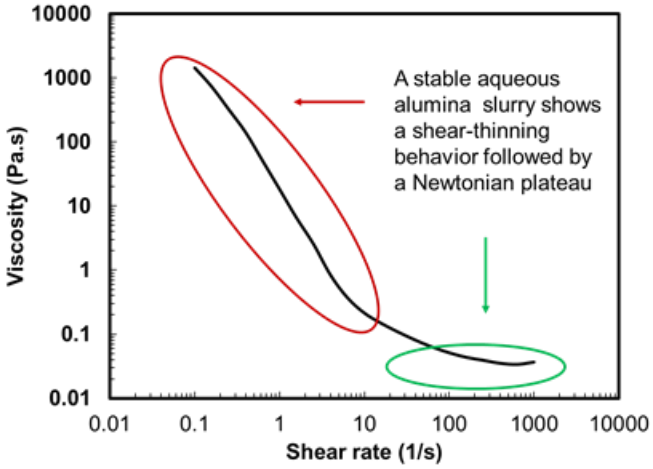

Figure 5-1 Viscosity as a function of shear rate for the ceramic slurry. The response shows a shear thinning behavior followed by a Newtonian plateau, which is an indication of a stable slurry.

Finally, the freeze-dried samples were stacked onto each other in a furnace for the thermal processing step. The heating step had two stages, binder burn-out and sintering. In the binder burn-out, the alginate binder was removed in the air at 600 °C. Debinded samples were then heated to 1600 °C to sinter the alumina. Silica nanoparticles were used as a liquid phase sintering aid. Figure 5-2A shows several ceramic plates after sintering. Figure 5-2B is an SEM cross-section image that shows the pore morphology inside the sintered ceramic plates (preform).

To infiltrate the porous ceramic, preform with metal (here copper, Cu), electrodeposition process from a conductive substrate was used (Figure 5-2D). The sintered ceramic plates were polished, sonicated in DI water and dried in a vacuum oven at 110 °C. To fabricate the cathode for electrodeposition, one side of each ceramic plate and a glass slide was coated with chromium (Cr) and gold (Au) using an e-beam evaporator (Figure 5-2B). A thin layer of Cr was deposited prior to Au deposition as an adhesion layer. The coated sides of each glass slide and ceramic plate were attached to each other to make the cathode for

electrodeposition. The electrodeposition process was controlled using a potentiostat in the galvanostatic mode at a current density of ~ 8.6 mA/cm^2. This current density was obtained from the cyclic voltammetry acquired from the fabricated cathode (Figure 5-2C). A copper mesh was used to function as an anode where oxidation reaction happens. A NaCl reference electrode was used to form a three-electrode electrochemical cell. The electrodeposition process was monitored until the copper filled up the ceramic preform plate from the gold-coated side to the opposite side, through the thickness of the ceramic plate (Figure 5-2C, inset). Once, over-deposition on the opposite side was observed, the electrodeposition was stopped. Figure 5-2D shows a schematic of the metal infiltration by electrodeposition process. Metal ions migrate inside the electrolyte-filled pores toward the bottom cathode and are reduced to metal to fill up the pores toward the top surface of the ceramic preform.

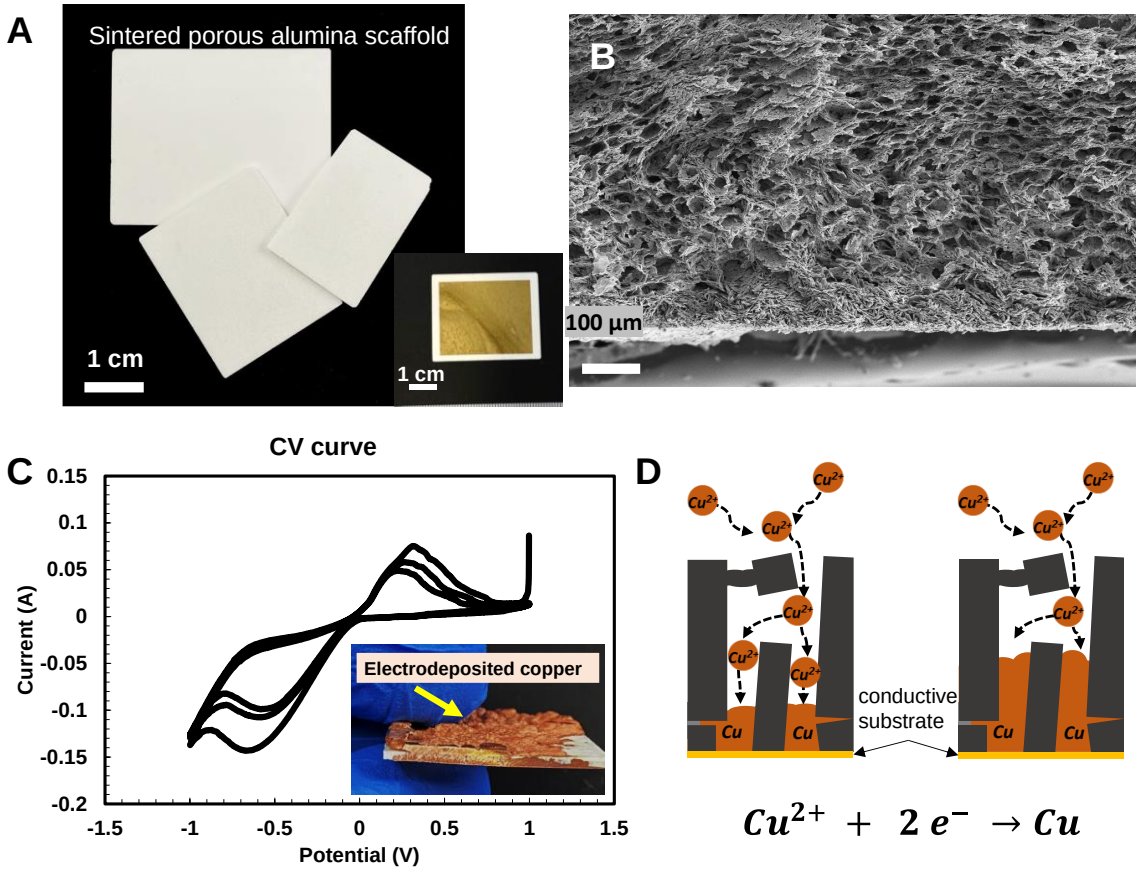

Figure 5-2 Manufacturing process of the metal-ceramic composite; (A) large ceramic preform plates fabricated by freeze-casting process. Inset, one-side coated ceramic preform ready for packaging into a cathode for metal infiltration by electrodeposition; (B) An SEM image of a cross-section of a preform that shows the pore morphology; (C) The CV (cyclic voltammetry) response of the electrochemical cell before copper infiltration; The inset is an optical image of the cross-section of an infiltrated preform that shows the uniform deposition through its thickness and over-deposition on the opposite surface of the ceramic plate. (D) A schematic representation of the metal-infiltration by electrodeposition process.The metal grows from the conductive side up to the free surface.

In the initial experiments, bi-directional freeze casting was performed to fabricate the ceramic preforms [148]. In this method, a 20° PDMS (Polydimethylsiloxane) wedge was placed at the bottom of the freeze-casting mold. The wedge provides a more uniform pore morphology compared to conventional freeze-casting. After freeze-drying the green body, samples were compressed perpendicular to the ice lamellar growth direction. This

compression step assists in a better alignment of the ceramic microplatelets, resulting in a more uniform lamellar structure [146]. Figure 5-3A and B show SEM images of the cross-section of the compressed scaffold depicting the effectiveness of the compression step in improvement of the pores' alignment. The compression was 60% of the original height of the green body. After the compression stage, samples went through the same thermal treatment as described earlier. The porosity in the compressed samples was 42%. This compression step was beneficial for several reasons. First, the material would have a better alignment, which may result in better mechanical properties including strength and toughness. Secondly, the well-aligned lamellar structure would ease the electrochemical metal infiltration as it provides a more straight path for the electrolyte to penetrate. However, the main drawback of this approach was its limitation in the sample size and scalability, as the obtained ceramic preforms were small to reliably fabricate composite samples by electroplating and for subsequent mechanical characterization. Figure 5-3C shows an SEM image of an infiltrated ceramic preform. The bright regions are copper, and the dark regions are alumina.

In the subsequent experiments, to overcome the sample size limitations, a large mold with dimensions of 150 mm by 150 mm was used and filled with only a few millimeters of slurry in height. The freezing time drastically increases with the depth of the slurry in the mold. Interestingly, in this way the slurry could be frozen in a few minutes as opposed to the initial experiments that on average took several hours and larger ceramic preforms could be fabricated.

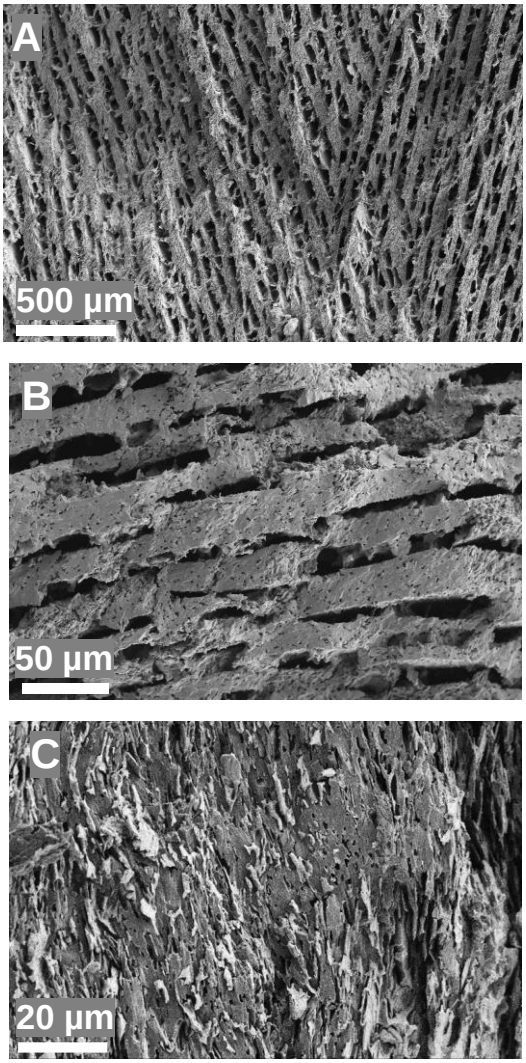

Figure 5-3 (A)-(C) SEM images of the compressed ceramic preforms fabricated using bi-directional freeze-casting; (C) An SEM image of an infiltrated ceramic preform. The bright regions are copper, and the dark regions are ceramic (alumina).

Structures in application can undergo various types of damages. Here, two types of common damages including a groove-type damage and a fractured-crack type damage are demonstrated. To simulate damages in the composites for healing demonstration, grooves were made. Interestingly, the grooves could be controllably machined on the composite using micromilling without breaking or cracking the samples, which is an indication of the machinability of the composites. Figure 5-4A shows a schematic representation of a beam

before and after healing a groove-type damage. Figure 5-4B shows the side-view profile of the machined grooves on the beam surface obtained by a profilometer. The grooves are ~100 – 200 micron in depth and a few hundred microns in width. Electrodeposition process was used to fill the grooves. For this purpose, the bottom side of each composite beam specimen was used as cathode, similar to the infiltration process that was originally used to fabricate the composite. The copper ions selectively deposited on the conductive regions of the composite (copper) and filled up the machined groove. After the deposition process was stopped, the over-grown depositions were polished. Figure 5-4C shows a SEM image of a groove after filling. The inset shows a high magnification SEM image of the cross-section of the groove. Noted that in this process, copper is deposited on a metal-ceramic composite surface. Since the ceramic phase (alumina) is non-conductive, copper can only deposit on the exposed copper on the surface of the groove. Hence, the quality of the deposited metal and the interface between the deposited metal and the original composite primarily depend on the surface conductivity of the original composite.

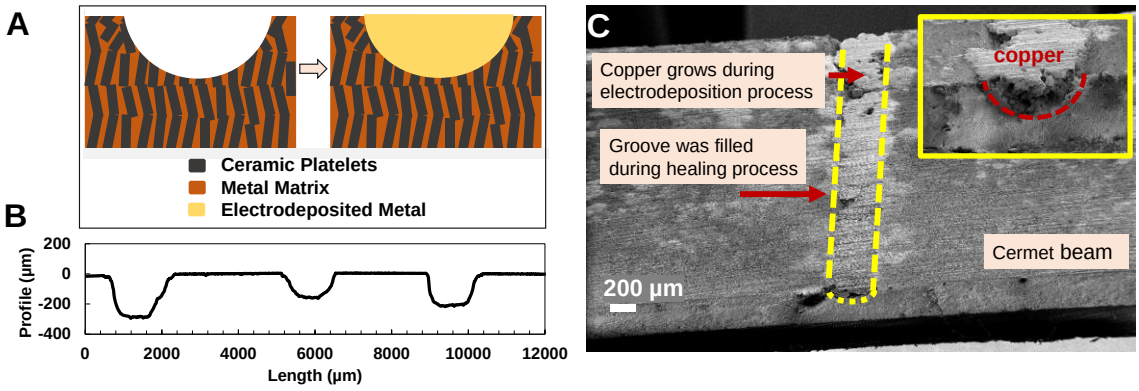

Figure 5-4 (A) A Schematic representation of the healing process for a machined groove on the composite. (B) A plot of the side-view profile of the machined grooves on the beam

surface. (C) An SEM image of a filled groove. The inset shows higher magnification side-view image.

Next, cracked beams were prepared. Initially, a notch was created on each beam, followed up by 3-point bending. The presence of the notch facilitated initiation and propagation of the crack from the tip of the notch. The flexure experiments were continued till each beam fully fractured, which resulted in a notch-crack geometry that was used for healing experiments.

In these experiments, flexure fracture experiments were first performed to generate a crack on notched beams. Then, it was aimed to heal the crack. The same galvanostatic electrodeposition process was used to fill up the cracks. For this purpose, two ends of each beam were connected to the cathode electrode of the potentiostat. Figure 5-5A depicts a schematic representation of the electrochemical healing process. Figure 5-5B-E show SEM images of the cracked composite after healing. The uniform bright regions are the deposited metal, and the grey regions are the original metal-ceramic composite. Several observations were made from these experiments. First, Cu grows from adjacent surfaces of the crack and notch and merges in the middle to heal the notch and the crack. Another observation is that the notch is nearly fully healed, while the crack is partially filled. This could be an indication that larger damages may be easier to heal than smaller ones, since the electrolyte must penetrate through tighter regions to heal smaller damages. Higher magnification SEM images in Figure 5-5C-E show the interface region between the deposited copper and the original metal-ceramic composite. Noted that since the ceramic phase of the composite (alumina) is not conductive, copper can only deposit on the metal phase (copper) of the composite. Given that the composite is co-continuous, at any given interface there is likely that metal and ceramic phases are exposed at roughly proportional to their volume percentage. As can be observed from the

SEM images, at the interface the copper-copper bonding is strong (metallic bond), where as the interface between the copper and ceramic phase is mechanical interlocking.

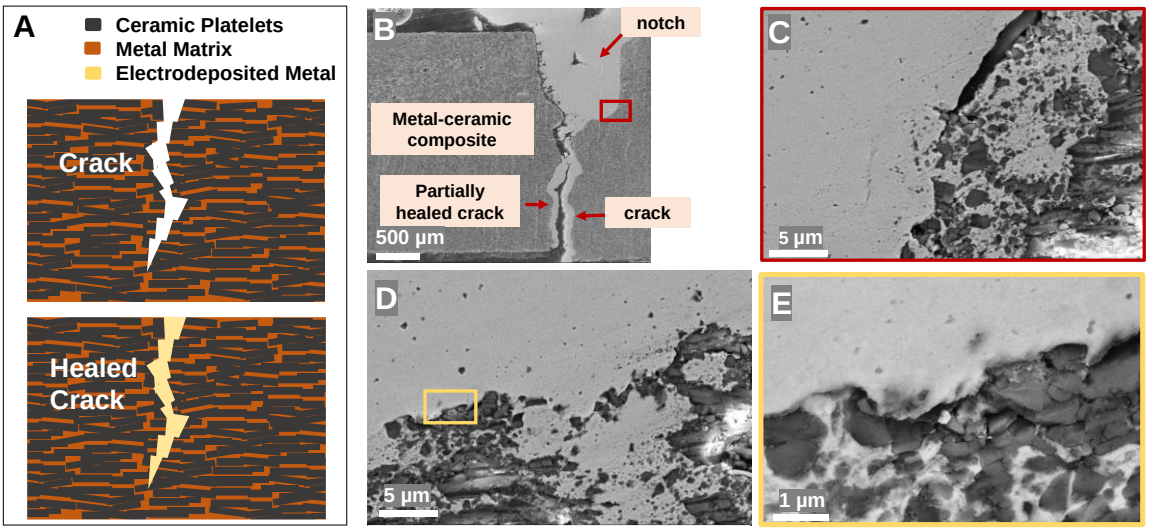

Figure 5-5 A schematic of the healing process of the composite beam and SEM images of the top-view of the notched composite beam after electrochemical healing process. (A) A schematic representation of the healing process for the notched composite. (B) A low magnification SEM image of the notched beam after the healing process. (C)-(E) Higher magnification SEM images of the interface between the deposited metal and the metal-ceramic composite.

To quantitatively investigate the healing process, flexural experiments were preformed on the composite healed beams. To do so, the fabricated composite was cut into beams using a diamond saw. One of the objectives was to measure the effects of the crack on the electrical resistance of the composite beams before and after fracture and after healing process. Given that the composite material is co-continuous, it is electrically conductive, and the electrical resistance of the cracked and healed composite can be measured. Since it was aimed to locally heal the crack after fracture, the composite beams were conformally coated with parylene C. Parylene is a commonly used polymer in the electronic industry to provide insulation or a chemical protective barrier. A shadow mask was prepared using Kapton tape to prevent

coating of two ends of the beams, which provide two electrically conductive nodes. The first experiment was the electrical resistance measurement after fracture and after the healing process. The second experiment was the healing process, which required having conductive nodes for the electrodeposition process. After parylene coating, the fractured surfaces were the only conductive parts in the beam, and hence this approach helped with locally healing of the crack avoiding the copper growth all over the beam.

Figure 5-7A shows a schematic of the localized healing process. To locally heal the beams, the electrochemical cell was prepared by placing a copper mesh inside a syringe filled with the copper electrolyte and connected it to the counter electrode using a copper wire. To avoid reduction reaction happening in this configuration, a plastic Luer lock pipette tip was used (Figure 5-7). The beam was placed on a Teflon sheet which provided a hydrophobic substrate, preventing the electrolyte from spreading. Both conductive ends of the beams were connected to the working electrode. At this point, the electrodeposition was started to heal the crack. Using this configuration, applying the same galvanostatic condition as the initial copper infiltration, the copper ions would migrate toward the cathode surface, which here was the fracture surfaces. Once they reached the conductive regions, the reduction reaction took place and copper ions turned into solid copper until the crack fully filled. Figure 5-7B shows an SEM image of a typical fracture surface. The bright regions are the metal phase, and the dark regions are the ceramic. These copper sites inside the cracks are the exposed surface during healing process that the metal phase starts growing from.

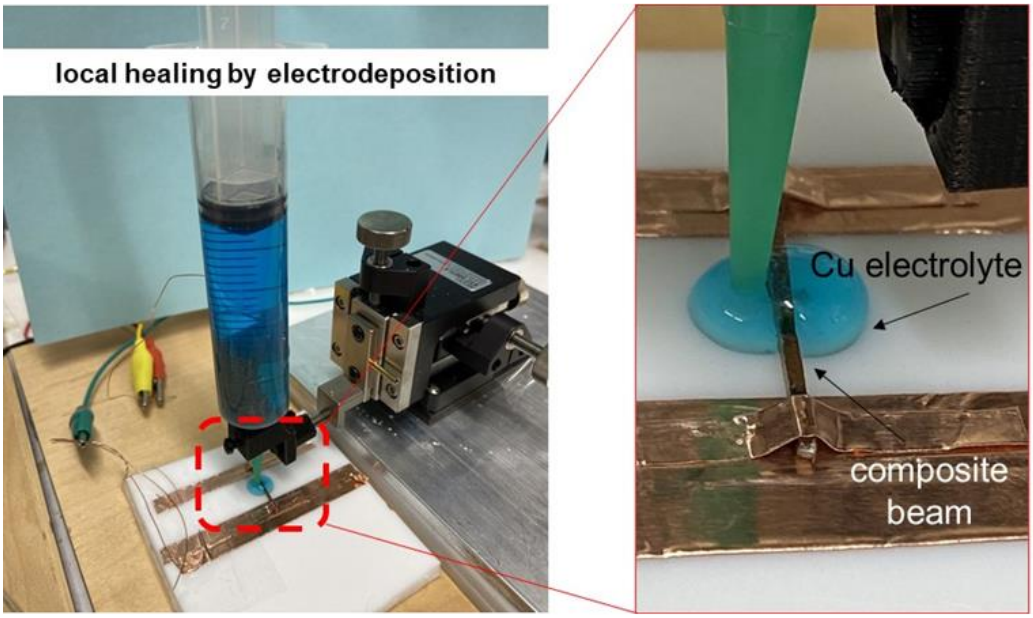

Figure 5-6 The customized healing setup. A copper mesh was used to act as the anode inside a copper-electrolyte filled syringe. The hydrophobic Teflon substrate prevents spreading of the electrolyte.

Figure 5-7C shows a representative force-deformation plot of an intact beam and a healed beam. The specific strengths of the intact beams and healed beams were $8.4 \pm 1.4 \frac{\text{MPa}}{gr/cm^3}$, and $6.8 \pm 0.9 \frac{\text{MPa}}{gr/cm^3}$,, respectively. The flexural strength of the intact beams and the healed beams was 31.8 ± 5.5 MPa, and 25.5 ± 3.6 MPa, respectively. The strength recovery was calculated by dividing the strength of the healed specimen to the strength of the intact specimen. The strength recovery was $82 \pm 14\%$.

The inset in Figure 5-7C shows a schematic of electrical resistivity variation during damage evolution and electrochemical healing. The electrical resistance is defined as $R = \frac{\rho l}{A}$, where ρ is the resistivity of the material, A is the cross-sectional area and l is the length. The electrical resistance of an intact beam remains constant until a damage, in this case a crack, initiates and propagates. As the crack propagates the resistance of the structure increases

because the cross-sectional area reduces. Therefore, the change in electrical resistance can be considered as an indication of damage evolution. After the damage is detected, by electrochemical healing of the beam, the electrical resistance will decrease, ideally to the original value. For these experiments, the resistance of the composite beams was measured before fracture, after fracture, and after healing process. The electrical resistance of the intact beam, fractured beam, and healed beam was 10.3 ± 1.2, 16.3 ± 2.5, and $13 \pm 2.8\ \mathrm{m\Omega}$, respectively. Such large changes in electrical resistance can be easily detected for application in intelligent system toward full autonomic damage detection and healing.

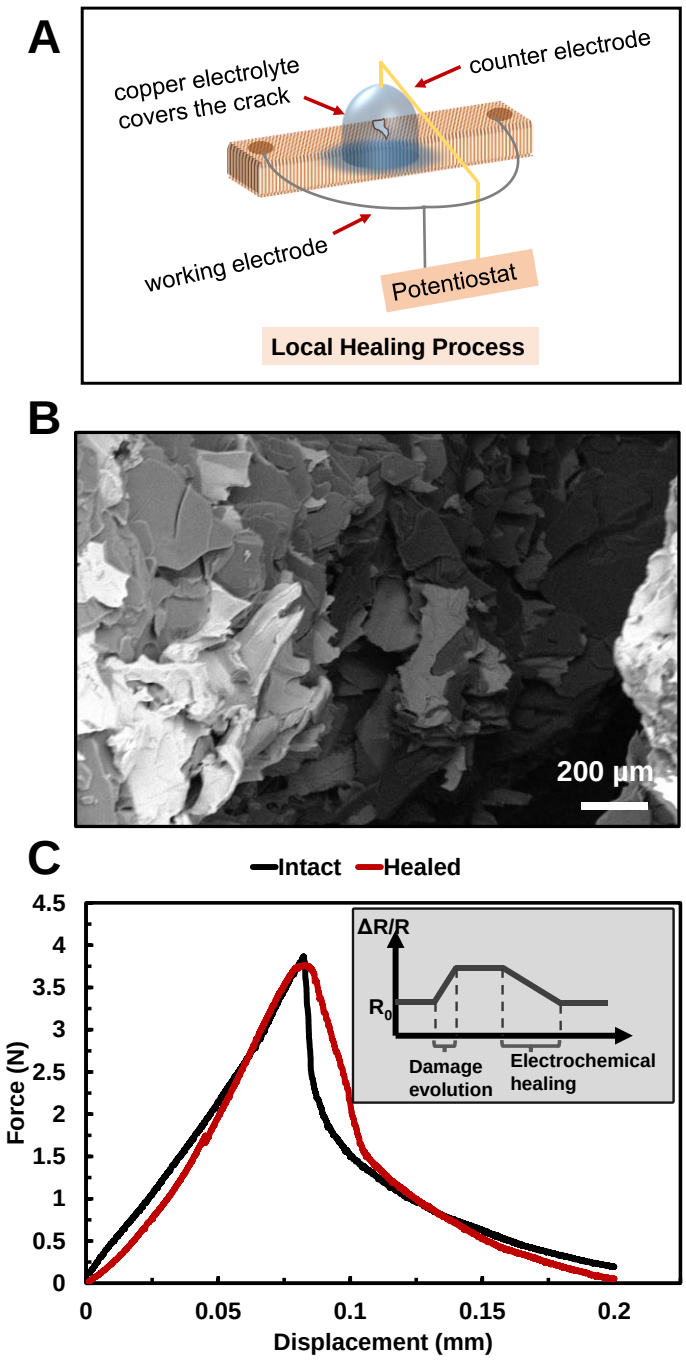

Figure 5-7 (A) A schematic of the localized healing process. (B) An SEM image of the interior surface of a crack after three-point bending experiment. The bright regions are copper, and the dark regions are alumina. (C) A representative force-displacement flexural response for an intact beam and a healed beam. The inset is a schematic of the electrical

resistivity variation during damage evolution, damage detection, and electrochemical healing.

To estimate the energy consumption during metal infiltration, the reference [146] was followed. The specific energy and energy density for the metal infiltration were $636\ \frac{J}{gr}$ and $5.6\ \frac{kJ}{cm^3}$, respectively. In conventional metal-ceramic infiltration processes a furnace is heated up to above the melting temperature of metal. These methods are often assisted with high vacuum. The energy consumption for metal infiltration using conventional metal infiltration process has been estimated to be $428\ \mathrm{MJ}$, with the corresponding specific energy and energy density of $39\ \frac{kJ}{gr}$ and $350\ \frac{kJ}{cm^3}$. [146]. These values only include the heating ramp and dwelling at a certain temperature for metal infiltration and exclude the energy consumption during high vacuum. The results for metal infiltration process to fabricate the metal-ceramic composite show that this process requires ~ 60 times less energy input compared to the conventional molten metal infiltration process.

To heal the cracks, a galvanostatic technique as the initial metal infiltration was used, with a current density of $20\ \frac{mA}{cm^2}$. The energy consumption to heal the crack was estimated to be $1.1 \pm 0.37\ \frac{J}{mm}$. To the best of our knowledge, this is the first report on the electrochemical healing of metal-ceramic composites. The electrochemical healing process has been previously used to heal a nickel foam. The energy consumption per crack length was reported for nickel foam to be $\sim 200 - 500\ \frac{J}{mm}$ [84]. In this case, the crack was healed locally as opposed to submerging the entire sample into an electrolyte bath, which can explain the much smaller energy consumption in this process. Specifically, results show that the energy

input to heal the crack per unit length of crack was three orders of magnitude lower than the reported value for nickel foams.

To study the performance of the interface between electrodeposited metal and the composite beam, nanoindentation experiments were performed. The continuous stiffness measurement technique was used to determine the hardness and elastic modulus. Figure 5-8A shows an SEM image of the sample and a schematic showing the regions of interest in nanoindentation experiments. An array of 9 by 25 indentations was performed on the healed sample. Each row of indentations swept the electrodeposited metal, the interface between the electrodeposited metal and the composite (which now on is called as the interface), and the composite. Thus, it could cover the electrodeposited metal, the interface, and the composite beam to quantify the performance of the interface. The inset in Figure 5-8C is an optical image of the sample showing the indentation footprints (larger image is shown in Figure 5-9). Figure 5-8B and C show a line-plot of the hardness and elastic modulus across these three regions. Both plots show a similar trend. The elastic modulus and hardness show nearly constant values on the electrodeposited metal region. There is a slight reduction in the average values of hardness and elastic modulus at the interface region. Noted that a clear interface region can be only roughly defined based on these values as three different regions was enclosed on the SEM images (Figure 5-8A). These plots show the average ± standard deviation of nine lines of indentations in the array, each with 25 indentation points. The values of hardness and elastic modulus of the copper, the interface, and the composite are presented in Figure 5-8 D-E.

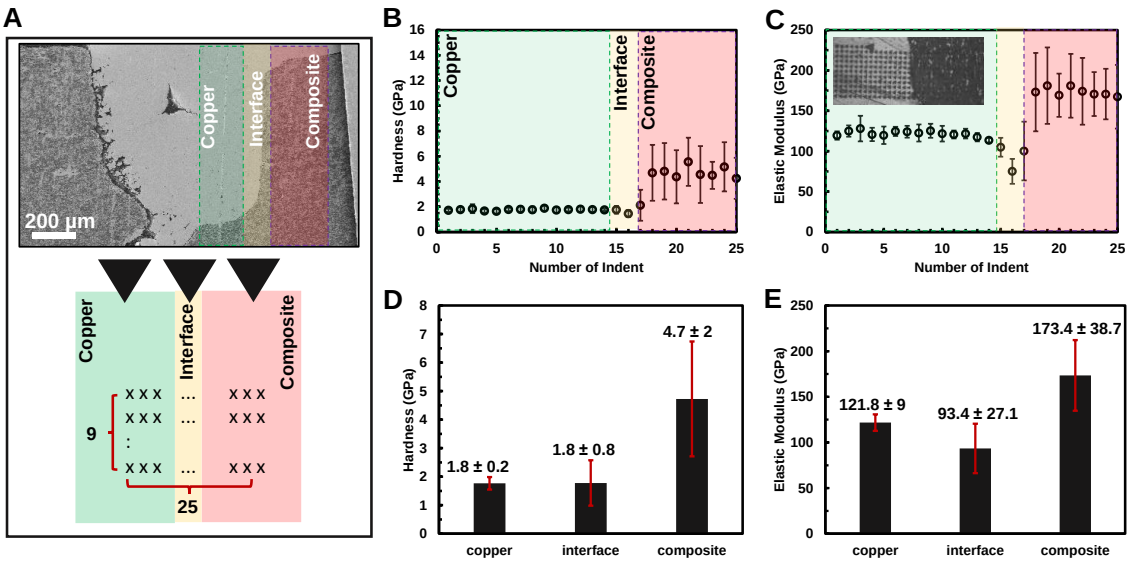

Figure 5-8 Nanoindentation experiments on the composite beam after healing process. (A) An SEM image of the healed composite showing the regions of interest in the nanoindentation experiment; and a schematic of the regions of interest showing the indentation array on the specific locations on the healed beam. (B) - (C) The hardness and elastic modulus versus number of indentations where each point on the plot shows the average and standard deviation of the results for nine indentations in each column. (D) - (E) The hardness and elastic modulus values in three different phases on the sample including copper, interface, and composite.

The indentation modulus of copper was 121.8 ± 9 which was in the range of the electrodeposited copper reported as 131 ± 35 GPa [149]. The elastic modulus of the composite can be estimated using the rule of mixtures. The measured elastic modulus of the composite was 173.4 ± 38.7, which was in good agreement with the calculated elastic modulus based on the rule of mixture, which was 177 GPa. Noted that the large standard deviations in composite properties originate from the rather random organization of the ceramic platelets inside the copper matrix, which results in large variation in mechanical properties compared to the ones on the pure metal region. Unlike elastic modulus, which is an intrinsic property of the material, hardness is an extrinsic property. The hardness of materials depends on the many parameters

including processing; thus, it can vary accordingly. Depending on the parameters in the electrochemical process, the grain size of the electrodeposited metal can vary. The grain size of the material directly affects the hardness of the material. The measured hardness of the electrodeposited copper in this experiment was 1.8 ± 0.2 GPa, which is in the range of the reported values in the literature, 1-2.2 GPa [149].

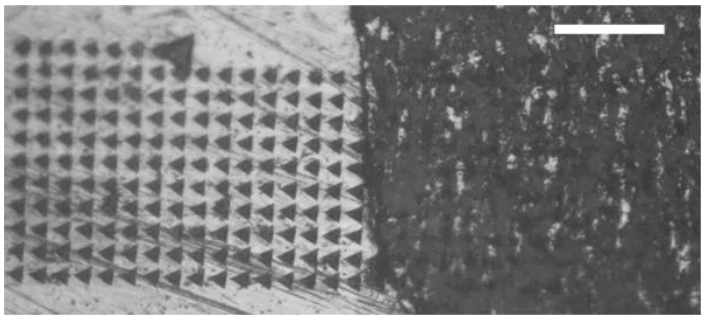

Figure 5-9 An optical image of the footprint of the nanoindentation array at the interface region between the electroplated metal and the metal-ceramic composite. The footprints are much clearer on the metal due to optical contrast. Scale bar: 50 μm.

5.3 Conclusion

In summary, a low-cost room temperature process for fabrication and healing of metal-ceramic composites was presented, which to the best of our knowledge is the first of its kind ever reported. The electrochemical deposition of metals was demonstrated that can be used as an effective process toward self-healing metal-ceramic composites. Future research can concentrate on deposition of various other metals and even alloys both for fabrication and healing, and more controlled healing process by using a closed loop feedback based on continuous monitoring of the variation of the electrical conductivity of the composite.

6 SCALABLE MANUFACTURING OF CERAMIC SHEETS VIA FREEZE CASTING USING A COLD PLATE

There are a wide range of manufacturing techniques for ceramic materials including three-dimensional printing, hot pressing, stir casting, freeze casting, tape casting, spark plasma sintering, among others, which uses different particles shapes and sizes. Sintering is the most crucial step in ceramic processing because it can directly affect the mechanical properties, pore structure, etc. Here, a process for ceramic manufacturing using a bi-modal nanoparticle size alumina is presented. Having two particle sizes in which the diameter of the particles are ten times larger with respect to each other may improve the sintering process. A better consolidation results in better mechanical properties.

6.1 Materials and Methods

6.1.1 Materials

Ceramic nanoparticles (diameter of 300 nm and 30 nm) were purchased from MSE Supplies LLC. Sodium alginate was purchased from Sigma Aldrich. TAC (Ammonium citrate tribasic) was purchased from Sigma Aldrich.

6.1.2 Ceramic slurry preparation

A 20 vol.% aqueous ceramic slurry was prepared using the following ratios: the alumina to sodium alginate ratio was 100:3 wt.%, and the ratio of powder to TAC was 100:0.4 wt.%. In the experiments alumina nanoparticles with diameters of 300 nm and 30 nm were used. For the first recipe, a ratio of alumina nanoparticles with diameter of 300 nm to 30 nm at 75 to 25

weight percent was used, while for the second recipe a 50 to 50 weight percent composition was used. The slurry was prepared in the following steps. First the TAC was added to DI water and mixed using a magnetic stirrer at 400 RPM for one hour until all powder completely dissolved. Using a similar methodology sodium alginate was added to the solution and mixed for one hour. Alumina nanoparticles were incrementally added to the TAC/sodium alginate/DI water solution and mixed using a planetary ball mill at 500 RPM for 24 hours. To prevent breakage of the nanoparticles, balls were not used during ball milling.

6.1.3 Freeze casting and freeze drying

A thermoelectric cold plate was used to freeze cast the ceramic slurry. A DLP 3D printer was used to print large rectangular molds. The ceramic slurry was poured into the molds and transferred onto the thermoelectric cold plate once the temperature of the cold plate reached -10 °C. The entire freezing process for each batch of samples took ~10 minutes. After freeze casting process, the molds were removed from the frozen slurry while on the thermoelectric cold plate. All samples were freeze-dried in a Labconco FreeZone 2.5 freeze drier for at least 48h.

6.1.4 Sintering

The freeze-dried ceramic plates were heated in a ST-1700C-445 (Sentro Tech) high temperature box furnace in air environment. The heating process had two steps, a binder burnout step to remove the sodium alginate and a sintering step to transform the green body into solid ceramic. The heating program was as follows: room temperature to 600 °C at 1 °C/min; holding at 600 °C for 4 h; from 600 °C to 1600 °C at 1 °C/min; holding at 1600 °C for 2 h; from 1600 °C to room temperature at 5 °C/min.

6.1.5 Calculation of density and porosity

Archimedes' principle can be used to estimate the porosity and density of porous materials. Using this technique, the density and porosity of the porous ceramic sheets can be measured. For the density measurements, samples were cleaned with water and dried in an oven. Samples were weighed using a scale and the mass of the samples was recorded as M_1. Then, samples were submerged in water and put in a vacuum for 3 h to ensure all pores were filled with water. The samples were weighed in water using an Archimedes density measurement kit and recorded the mass of the samples as M_2. In the last step, a squeezed wet towel was used to remove the water droplets from the surface of the samples and recorded the mass of the samples as M_3. The below equations are used to determine the porosity (P) and density:

$$P = \frac{M_3 - M_1}{M_3 - M_2} * 100\% \quad (1)$$

$$\rho = \frac{M_1}{M_3 - M_2} * \rho_{water} \quad (2)$$

6.1.6 Mechanical properties

Three-point flexural experiments were chosen to study the mechanical properties of the ceramic beams and the composite beams using a universal testing machine (Shimadzu Inc.). The span length of the samples was 10 mm. The samples were cut into ~ 2 mm × 2 mm × 15 mm beams. The crosshead displacement rate was 0.05 mm/min. A 50 N loadcell was used to capture load-displacement response in mechanical experiments. Equations below were used to calculate flexural stress and strain, respectively:

$$\sigma_f = \frac{3Fl}{2bd^2} \quad (3)$$

$$\epsilon_f = \frac{6Dd}{l^2} \quad (4)$$

where F is force, l is the span length, b and d are the width and thickness of the beams, and D is the displacement. The strength and strain at break of the ceramics at 3:1 and 1:1 ratio was 13.61 ±4.1 MPa, 18.96 ± 3.4 MPa, and 0.0054 ± 0.0018, 0.0057 ± 0.0035, respectively.

6.1.7 Characterization of the rheological properties

The rheological measurements were performed using an Anton Paar rheometer using a 50-mm upper cone with an angle of 0.5° and a 50-mm in diameter lower plate. The viscosity of the ceramic slurry was determined by applying a shear rate sweep from 1000 S^{-1} to 100^{-1} S^{-1}.

6.1.8 Scanning electron microscopy (SEM)

SEM imaging of the ceramic scaffolds and composite beams was performed using a Zeiss Auriga SEM. For ceramic plates, samples were coated with gold to enhance their electrical conductivity for SEM imaging.

6.2 Results and Discussions

The manufacturing process starts with the preparation of an aqueous ceramic slurry. To summarize, TAC and sodium alginate were dissolved in DI water using a magnetic stirrer for one hour, separately. In the next step, alumina nanoparticles were added to the ceramic slurry and homogeneously mixed using a ball mill. Details of the material preparation are presented in the materials and methods section. In these experiments, spherical ceramic nanoparticles

were used with two different diameters, 300 nm, and 30 nm. Having a ceramic slurry composed of two different nanoparticle sizes could provide a better packing density compared to one size nanoparticle [106]. To identify the ratio of the alumina nanoparticles, a set of experiments was designed. According to the literature when one of the nanoparticles were ten times larger than the other, a ratio of 3:1 wt.% of larger to smaller diameter nanoparticles would provide the maximum packing density [106]. In another experiment a ceramic slurry based on 1:1 ratio was prepared. To ensure that the ceramic slurries were stable, the viscosity as a function of shear rate was measured using a rheometer. The procedure of preparing a stable ceramic slurry is presented in chapter 5. The viscosity of a stable alumina ceramic slurry shows a shear thinning behavior, as shown in Figure 6-1. By increasing the ratio of the smaller diameter nanoparticles, the viscosity of the ceramic slurry increases drastically.

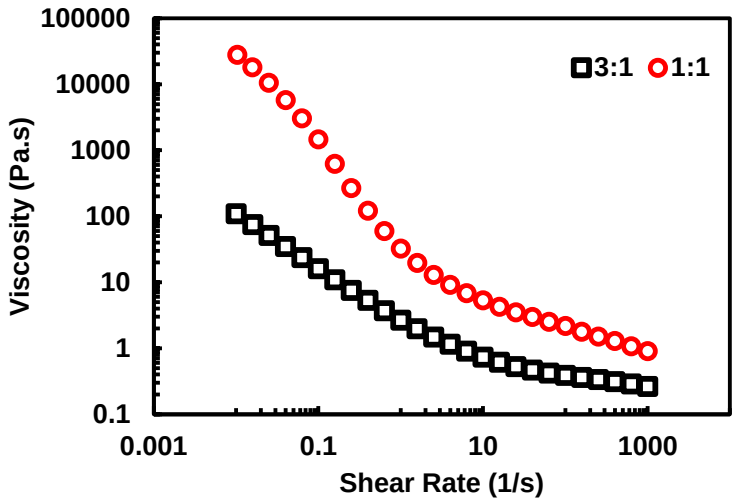

Figure 6-1 The rheological measurement of the ceramic slurry. The viscosity vs. shear rate response of the ceramic slurries with 3:1 and 1:1 ratio show a shear thinning behavior.

To freeze the ceramic slurry, a thermoelectric cold plate (TE Technologies INC.) was used. To have a constant cooling rate the temperature was set to -10 °C. While waiting for the cold plate to reach the desired temperature, the ceramic slurry was poured in the molds, which were placed on a separate copper plate. Once the cold plate reached the desired temperature, the entire copper plate with the molds were transferred on to the cold plate to freeze. This was done to ensure that the ceramic slurry freezes at constant cooling rate. A constant cooling rate is crucial in the follow up experiments as it affects the microstructure and pore morphology. Figure 6-2 shows the temperature – time profile of the cold plate. The inset is an optical image of the cold plate and the molds after freezing. After the freezing step, a freeze drier was used to perform the sublimation to remove the ice content. The green bodies were then heated up to 600 °C for binder burnout followed by another heating step to 1600 °C for sintering.

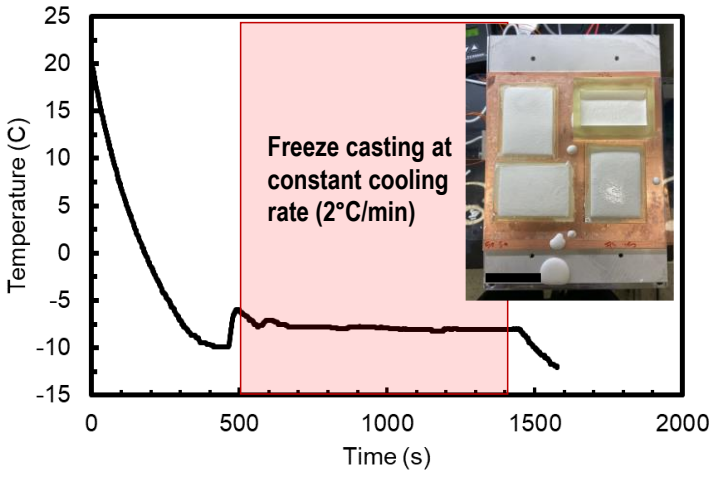

Figure 6-2 The temperature – time profile of the cold side of the thermoelectric plate. The inset is an optical image of the frozen ceramic slurry on the cold plate. The scale bar is 5 cm.

The Archimedes density measurement technique is preferrable for the measurements of the density and porosity of the porous materials compared to the geometrical measurement. Archimedes method was used to measure the density and porosity of ceramic plates. Table 6-1 presents the density and porosity of the sintered samples. The density of the ceramic with 1:1 ratio was slightly higher than 3:1 ratio. The reason for the higher density and lower porosity of the ceramic made from a 1:1 ratio of the alumina nanoparticles compared to the 3:1 ratio is that the former composition had a better packing density as the smaller diameter nanoparticles could filled the empty spaces between larger diameter nanoparticles. At least three samples were used for density measurements.

Table 6-1 Density and porosity values of the porous ceramic at different ratios of the alumina nanoparticles.

	Density (gr/cm3)	Porosity (%)
3:1	1.53 ± 0.04	60.3 ± 0.6
1:1	1.74 ± 0.02	56 ± 0.8

To further evaluate the properties of the ceramics with two compositions, mechanical characterizations was performed. The sintered samples were cut into beams for mechanical experiments. The three-point bending experiment was chosen to extract the mechanical performance of the sintered ceramics at two different compositions. At least 24 samples were tested for each case. Figure 6-3(A,B) shows representative flexural stress – strain plots for each composition. Figure 6-3 C shows an Ashby plot for the strength versus density. The blue circle is the ceramic manufactured in this work.

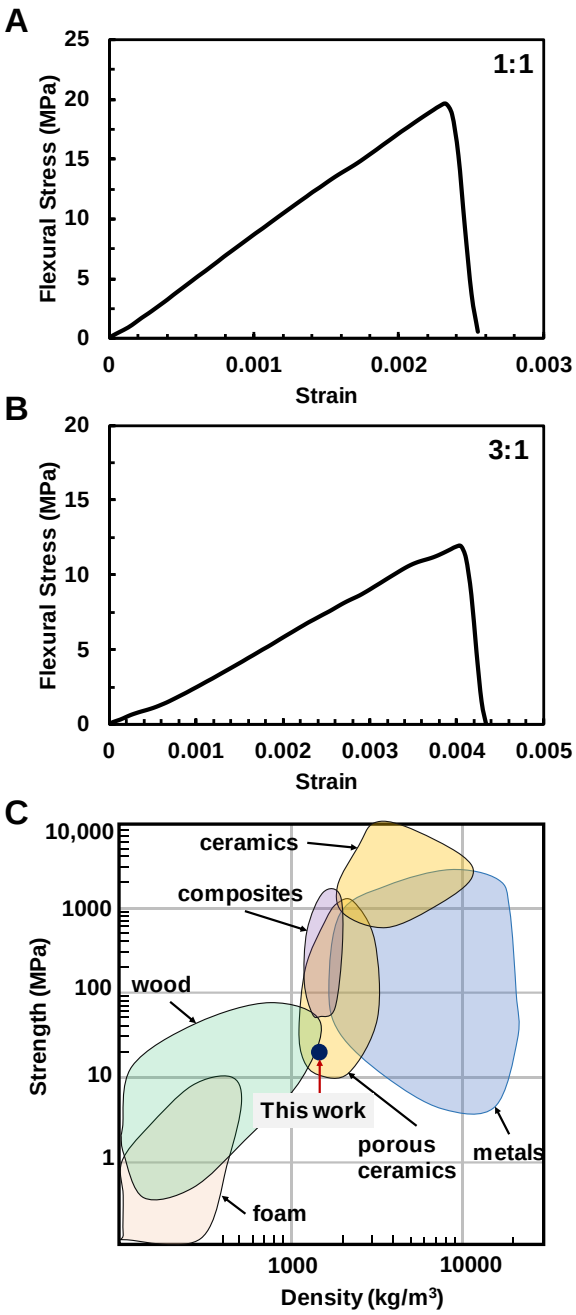

Figure 6-3 Mechanical properties of ceramic beams. The flexural stress – strain plots of the A) 1:1, and B) 3:1 composition. C) A strength vs. density Ashby plot. The blue circle is the ceramic manufactured in this work.

For ceramics, ASTM standards recommends performing and reporting statistical parameters using the Weibull analysis [127]. This is because the mechanical performance of the brittle materials largely depends on the distribution of flaws and defects, thus, deterministic

methods to analyze the mechanical properties are not comprehensive. The flexural strength is presented in terms of a two parameter Weibull distribution, $P_f = 1 - exp\left(-\frac{\sigma}{\sigma_0}\right)^m$ (Figure 6-4). Such analysis considers the variability in ceramic strength as a function of flaw population in the material. m is the Weibull modulus, and σ_0 is the characteristic strength. The Weibull modulus is the shape parameter that maps a failure probability of a specimen in a range of stress. Specimens' flexural strengths were ranked in ascending order and assigned a probability using $P_f = (i - 0.5)/n$, where n is the total number of specimens. Probabilities and the flexural strength are presented in terms of $\ln\left(\ln\left(1/\left(1 - P_f\right)\right)\right)$ and $\ln \sigma$. Based on this analysis, the characteristic strength, which is the value of stress for $P_f = 63.2\%$, for the 3:1, and 1:1 composition was calculated to be ~15.1 MPa, ~20.5 MPa, respectively. The specific characteristic strengths of the ceramics at 3:1, and 1:1 ratios were 9.8, and 11.8 $\frac{MPa}{gr/cm^3}$, respectively. The specific characteristic strength increases as the ratio of the smaller diameter nanoparticles increases. This is because the smaller diameter nanoparticles have higher surface area. Thus, during sintering, it helps in better consolidation as the sintering process tends to minimize the surface area by atomic diffusion. The linear regression of the flexural strength yields the Weibull moduli of $m = 3.8$, and $m = 6$ for 3:1, and 1:1, respectively. The higher the value of the Weibull modulus, the lower variability in the strength of the ceramic material. As a comparison, the Weibull modulus of the 3D printed silicon oxycarbide and freeze cast porous yttria stabilized zirconia has been reported to be $m = 3.7$, $m = 5.8$, respectively [54], [150].

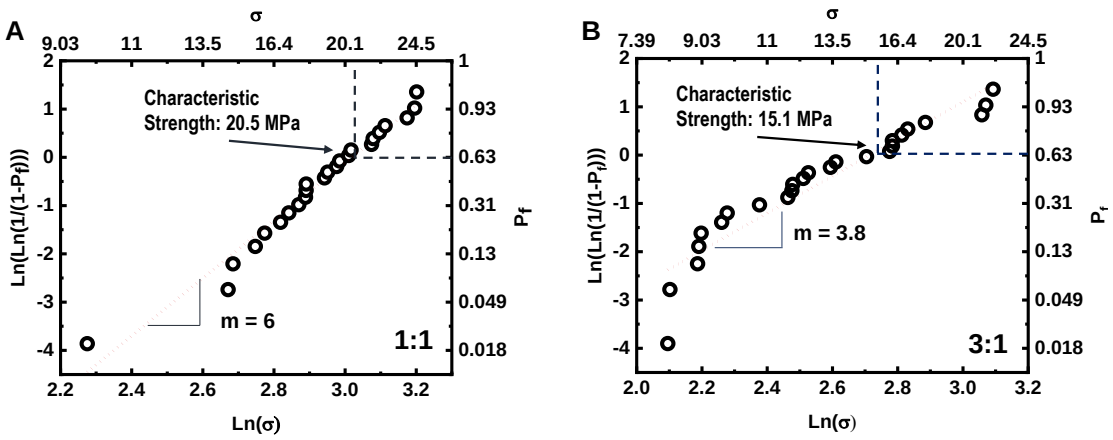

Figure 6-4 Statistical analysis of the mechanical properties. The Weibull analysis of the flexural strength of the ceramic beams (A) ceramic composition of 1:1, (B) ceramic composition of 3:1.

We acquired SEM images of the cross section of the ceramic beams to study the pore structure. Although smaller pores contribute to better mechanical performance, larger pores in the present study are preferable for the metal infiltration process. Porous ceramics are used to manufacture metal ceramic composites [91]. In chapter five, a manufacturing process for co-continuous metal ceramic composites was presented. In this process a copper sulfate electrolyte was used for electrochemical metal infiltration into porous alumina. An open pore structure is essential for metal infiltration step of the process as the metal grows from one side of the ceramic sheet to the other side. A uniform pore distribution is critical in terms of uniform metal growth. Because the metal can grow easier in large pores, this may lead to non-uniform metal infiltration as the smaller pores may not fill up during the metal infiltration. Figure 6-5A-D shows SEM images of the cross section of the ceramic beam at 3:1 ratio of ceramic nanoparticles. High magnification SEM images of the cross section show the microstructure and micropores.

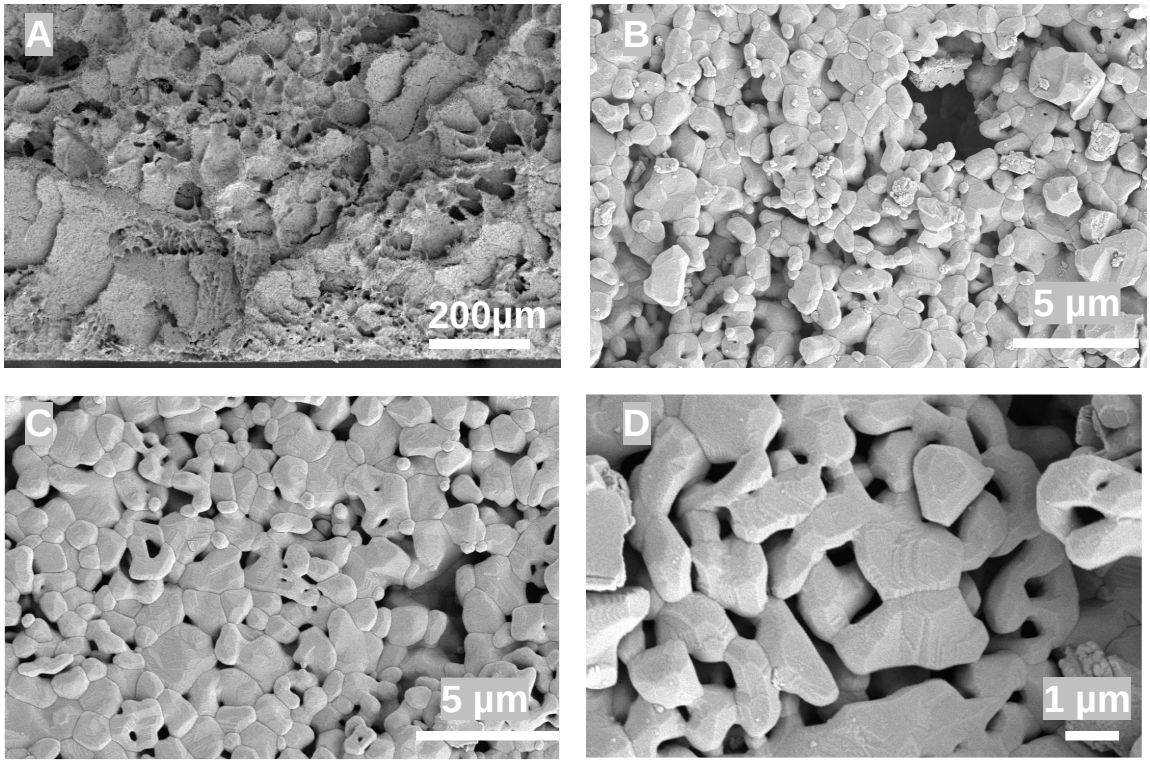

Figure 6-5 SEM images of the cross section of a ceramic beam at 3:1 ratio of nanoparticles. (A) Zoomed out view of the cross section showing the pore structure of the ceramic. (B), (C), (D) high magnification images of the cross section that shows the microstructure of the ceramic beam.

Figure 6-6 (A-F) show SEM images of the cross section of the ceramic beams at 1:1 ratio of the ceramic nanoparticles. Pores are distributed uniformly in the cross section of the beams. Higher magnification SEM images show the microstructure of the ceramic. The grain boundaries show that the sintering process and atomic diffusion of nanoparticles were performed successfully. To further investigate the pore structure, SEM images of the larger pores were taken. Figure 6-6 (E, F) show that the pores are open, which is desirable for the metal infiltration process to manufacture metal ceramic composites.

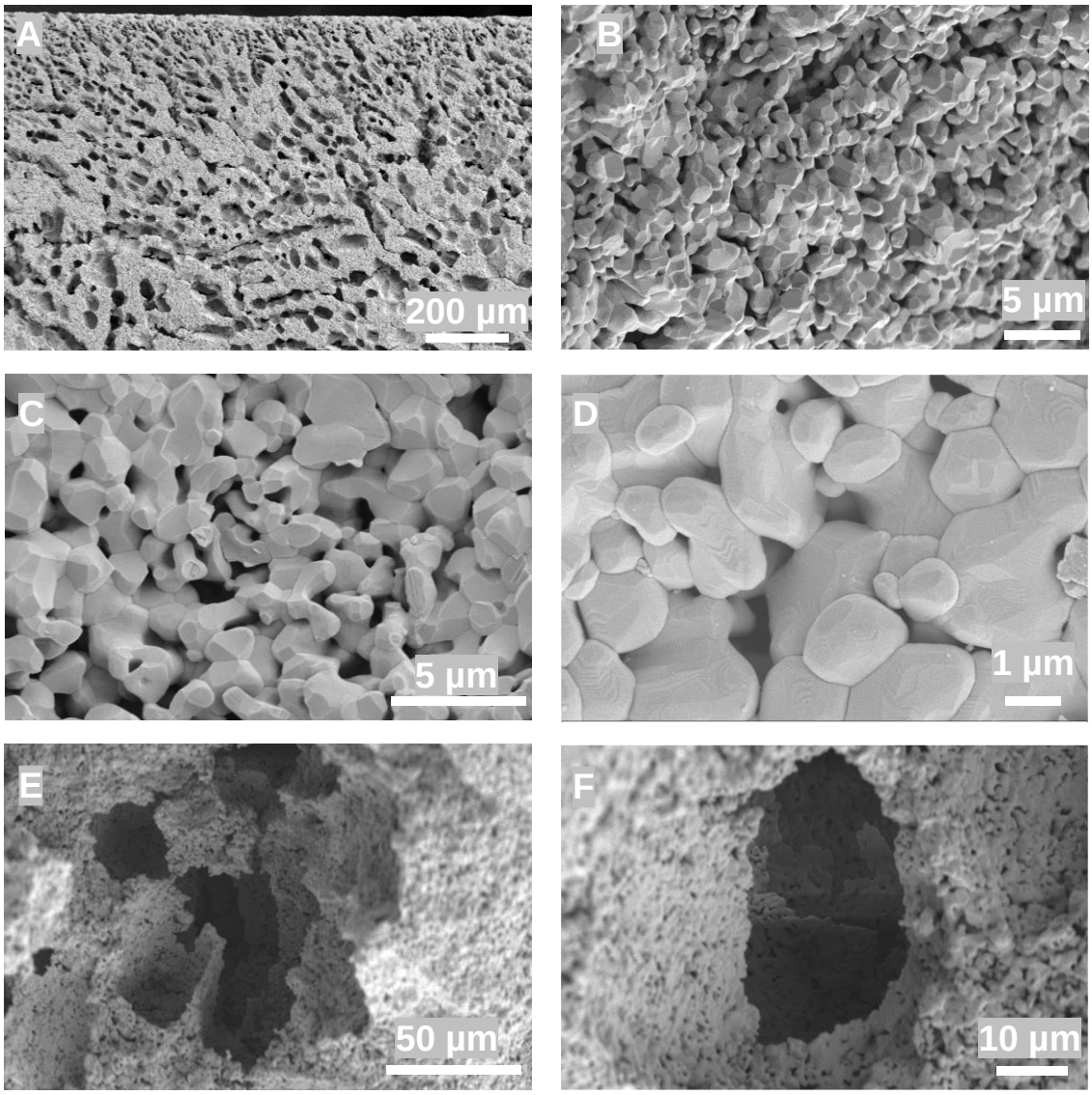

Figure 6-6 SEM images of the cross section of the ceramic with 1:1 ratio of nanoparticles. (A) zoomed out view of the cross section of the ceramic beam. (B), (C), (D) high magnification SEM images that show the microstructure of the ceramic. (D), (E) Images of the micro pores in the cross section of the beam.

Figure 6-7 (A-B) show the distribution of the grain size for the alumina nanoparticle compositions of 1:1, and 3:1. The average grain size of the former composition is 0.9 µm and the latter is 1.1 µm. The smaller grain size in the 1:1 composition is attributed to the larger

fraction of the smaller diameter nanoparticles in the ceramic. Smaller grain size also contributes to the better mechanical performance of the ceramic material.

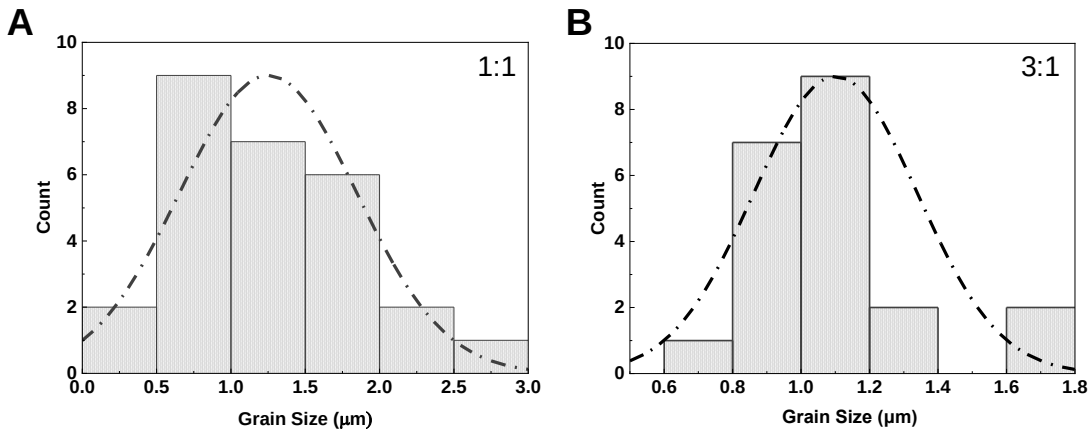

Figure 6-7 The grain size distribution for the alumina nanoparticle composition of (A) 1:1, and (B) 3:1.

6.3 Conclusions

Here, the process of fabricating porous ceramics using two different nanoparticle sizes is described. Two alumina nanoparticles with diameters of 300 nm and 30 nm were mixed in 1:1 and 3:1 ratio. The density and porosity measurements showed a slight increase in density and a reduction in porosity as the fraction of smaller diameter nanoparticles was increased. The mechanical characterization of ceramic beams showed that the specific characteristic strength increased by ~ 20% as the fraction of the small nanoparticles increased. The reason for improvement of the strength and the increase in the density was that the smaller diameter nanoparticles can fill up the gaps between the larger nanoparticles and provide higher surface area. This will be beneficial in better sintering that results in higher strength. Additionally, SEM images of the cross sections of the beams showed that the samples made from the 1:1 ratio of

the alumina nanoparticles have more uniform pore structure. A uniform pore structure is desirable for the follow up step in the process of manufacturing a metal ceramic composite.

7 MECHANICAL CHARACTERIZATION OF INTACT AND HEALED METAL-CERAMIC COMPOSITES

In Chapter 5, a new process for manufacturing and healing of metal-ceramic composites is presented. This technique is based on an electrochemical approach that infiltrates a metal inside pores of a ceramic preform. Since the interface between the metal and ceramic in this process is mechanical interlocking, the electrochemical healing is only applied to the metal phase of the composite. In other words, the healing process fills up a crack or a damage with a metal. The electrodeposited metal nucleates over the metal phase of the metal-ceramic composite as it is the only conductive part of the composite and grows until the crack is entirely healed. The strength of the healed composite depends on the strength of the interface between the metal in the original metal- ceramic composite and the electrodeposited metal as healing material. In this chapter, a systematic study is presented to investigate the interfacial strength of the locally healed metal-ceramic composite.

7.1 Materials and Methods

7.1.1 Material preparation:

Ceramic nanoparticles (diameter of 300 nm and 30nm) were purchased from MSE Supplies LLC. Sodium alginate was purchased from Sigma Aldrich. TAC (Ammonium citrate tribasic) was purchased from Sigma Aldrich.

7.1.2 Ceramic sheet manufacturing

A 20 vol.% aqueous ceramic slurry was prepared using the following ratios: the alumina to sodium alginate ratio was 100:3 wt.%, and the ratio of powder to TAC was 100:0.4 wt.%. Alumina nanoparticles with diameters of 300 nm, and 30 nm at a ratio of 50 to 50 weight percent were used to prepare the ceramic slurry. The slurry was prepared in the following steps. First the TAC was added to DI water and mixed using a magnetic stirrer at 400 RPM for one hour until the entire powder completely dissolved. Using a similar methodology, sodium alginate was added to the solution and mixed for one hour. Alumina nanoparticles were incrementally added to the TAC/sodium alginate/DI water solution and mixed using a planetary ball mill at 500 RPM for 24 hours. To prevent breakage of the nanoparticles, balls were not used during ball milling.

7.1.3 Heating process

The freeze-dried ceramic plates were heated in a ST-1700C-445 (Sentro Tech) high temperature box furnace in air environment. The heating process was performed in two steps, a binder burnout step to remove the sodium alginate and a sintering step to transform the green body into solid ceramic. The heating program was as follows: room temperature to 600 °C at 1 °C/min; holding at 600 °C for 4 h; from 600 °C to 1600 °C at 1 °C/min; holding at 1600 °C for 2 h; from 1600 °C to room temperature at 5 °C/min.

7.1.4 Mechanical characterization

Three-point flexural experiments were chosen to study mechanical properties of the ceramic beams and the composite beams using a universal testing machine (Shimadzu Inc.). The span length of the samples was 10 mm. The samples were cut into ~ 2.5 mm × 1.5 mm × 20 mm beams. The crosshead displacement rate was 0.05 mm/min. A 50 N loadcell was used to

record the load-displacement response in mechanical experiments. Equations below were used to calculate flexural stress and strain, respectively:

$$\boldsymbol{\sigma_f = \frac{3Fl}{2bd^2}} \quad (1)$$

$$\boldsymbol{\epsilon_f = \frac{6Dd}{l^2}} \quad (2)$$

where F is force, l is the span length, b and d are the width and thickness of the beams, and D is the displacement.

7.1.5 Estimation of porosity and density

Archimedes' principle can be used to estimate the porosity and density of porous materials. Using this technique, the density and porosity of the porous ceramic sheet can be measured. After metal infiltration process the same method can be used to determine the density and porosity of the composite material. Ideally, the porosity percentage of the porous ceramic is the volume of the ceramic that can be filled with metal, however, since only one step metal infiltration was done, there is some porosity left in the composite. Using Archimedes' principle, we can measure the porosity percentage of the composite. The difference between the porosity percentage of the ceramic and the composite is the percentage of the metal phase. Based on measurement, we estimate that the composite had a ceramic phase ~ 44%, metal phase ~44%, and a porosity of ~12%.

Samples were cleaned with water and dried in an oven. Then, they were weighed using a scale and the mass of each sample was recorded the mass as M_1. In the next step, the samples were submerged in water and put in a vacuum for 3 h to ensure all pores were filled with water. Next, the samples were weighed in water using an Archimedes' density measurement kit and

the mass of each sample was recorded as M_2. In the last step, squeezed wet towel was used to remove the water droplets from the surface of the samples and the mass of each sample was recorded as M_3. The below equations were used to determine the porosity (P) and density:

$$P = \frac{M_3 - M_1}{M_3 - M_2} * 100\% \quad (3)$$

$$\rho = \frac{M_1}{M_3 - M_2} * \rho_{water} \quad (4)$$

7.1.6 Scanning electron microscopy (SEM)

SEM imaging of the ceramic scaffolds and composite beams was performed using a Zeiss Auriga SEM.

7.2 Results and Discussion

The manufacturing process of the co-continuous metal-ceramic composite involves two steps: fabrication of the porous ceramic sheets; and the metal infiltration into the porous ceramic preforms. Large ceramic sheets were fabricated using a process described in Chapter six. To summarize, a 20-vol. % ceramic slurry was prepared by dissolving TAC as dispersant and sodium alginate as binder in DI water. Next the alumina nanoparticles were added to the solution and mixed for several hours. Details of the ceramic slurry preparation are presented in the materials and methods section. Here, a ratio of 50 to 50 weight percent was used for the alumina nanoparticles with diameters of 300 nm and 30 nm since it provides better specific characteristic strength, and more importantly uniform open pore structure. Chapter six presents the procedure to fabricate the ceramic sheets, characterization, and discussion on how using two different size ceramic nanoparticles can affect the final ceramic. Here, the same procedure for making the ceramic sheets as described in Chapter six was used.

After making the ceramic sheets, to make the metal-ceramic composite, electrodeposition was used to infiltrate the porous ceramic with metal (here copper). A commercial copper sulfate electrolyte was used in the electrodeposition process. One side of the ceramic sheets and glass slides were coated with chromium (Cr) and gold (Au) using an electron beam (e-beam) evaporator to have conductive surfaces. The conductive surfaces of the ceramic sheet and a glass slides were packaged face to each other to act as cathode in the electrochemical cell (Figure 7-1 A). A VersaSTAT-4 Potentiostat/Galvanostat was used to perform the electrodeposition process (Figure 7-1 B). A copper mesh was used to act as the anode. The results in chapter five showed that copper can grow easier in larger areas compared to narrow channels. Thus, it is important to prevent nonuniform copper growth inside the pores of the ceramic sheets given that the ceramic sheets have both large pores and small pores. Therefore, the experiment was started with a low current density in the beginning of the infiltration to ensure that the gap between the ceramic sheet and the glass slide fills up uniformly. By applying a constant current in three steps, the electrodeposition process was controlled; a constant current of 1 mA/cm^2 for one day, 3 mA/cm^2 for three days, and 20 mA/cm^2 for six days to fill up the porous ceramic sheet. Figure 7-1 C-E shows the ceramic sheet after the electrodeposition process. The ceramic sheet was cut into beams for the three-point bending tests. Three-point bending experiments was chosen for the mechanical characterization as it involves both tensile and compressive stresses. Ten samples were tested to extract the flexural stress - strain of the metal-ceramic composite. The flexural strength and strain of the composite were 38.34 ± 13.01 MPa, and 0.0062 ± 0.0025, respectively. Addition of the metal phase into the ceramic sheet increased the flexural strength of the ceramic ~ 102%. Figure 7-1 F shows a representative flexural stress – strain curve of a metal-ceramic

composite. The inset is a beam during a three-point bending test. Archimedes' Principle was used to measure the density of the composite. The density of the composite was 4.4 gr/cm^3. The composite had ~ 44 vol. % ceramic phase, 44 vol. % metal phase, and 12 % porosity.

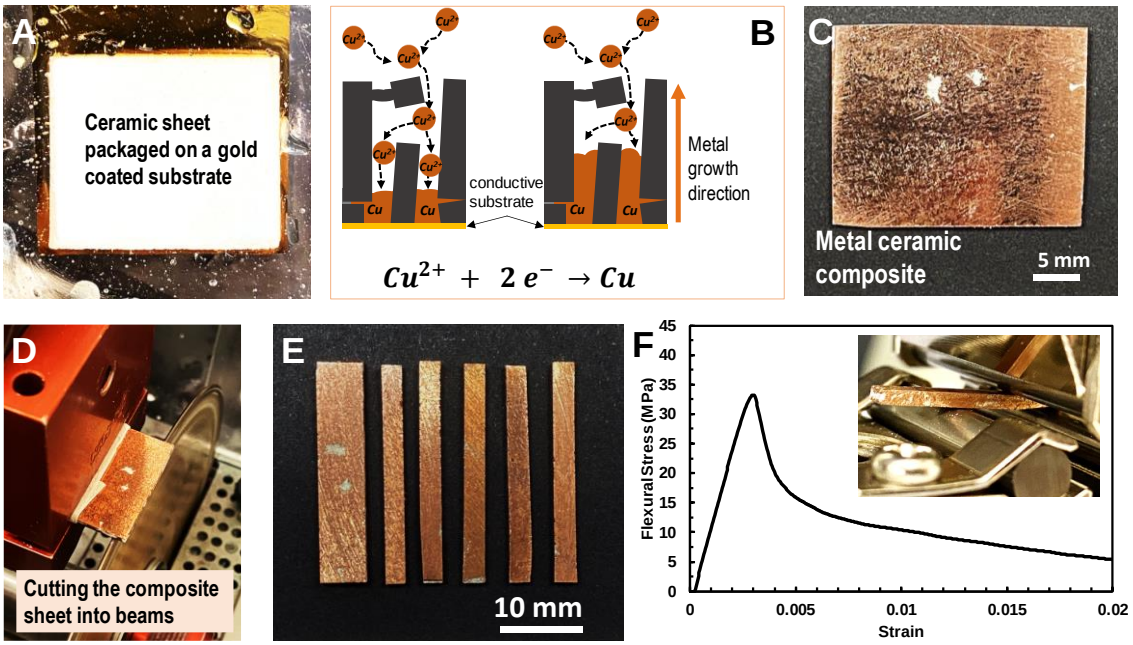

Figure 7-1 The process of fabricating metal-ceramic composite beams. (A) A ceramic sheet packaged on a conductive substrate for metal infiltration process using electrodeposition. (B) A schematic representation of the metal infiltration process. Copper ions are reduced to solid copper by applying a constant current starting from the conductive substrate. (C) A metal-ceramic composite sheet after electrodeposition infiltration. (D) The cutting process of the composite material using a diamond saw. (E) The beams were cut from the composite sheet. (F) A representative flexural stress – strain response of a composite beam that shows a ductile behavior due to the inclusion of the metal phase into the ceramic sheet. The inset shows a beam during the three -point bending test.

To visualize the morphology and microstructure of the metal and ceramic in the composite material, SEM images of a polished cross-section of a composite beam is provided (Figure 7-2 A). Bright regions are copper and the dark areas are ceramic. Figure 7-2 B-C show zoomed-in views of different locations on the cross-section of the composite beam. The images show that in some regions the initial metal infiltration process was not perfect as it left

some unfilled pores in the composite. This can be improved by optimizing the initial electrodeposition parameters to ensure all open pores are filled uniformly. These defects can reduce the strength as they can act as initiation points for crack formation. Figure 7-2 D shows a high magnification SEM image of the interface between the ceramic and the electrodeposited copper in the composite.

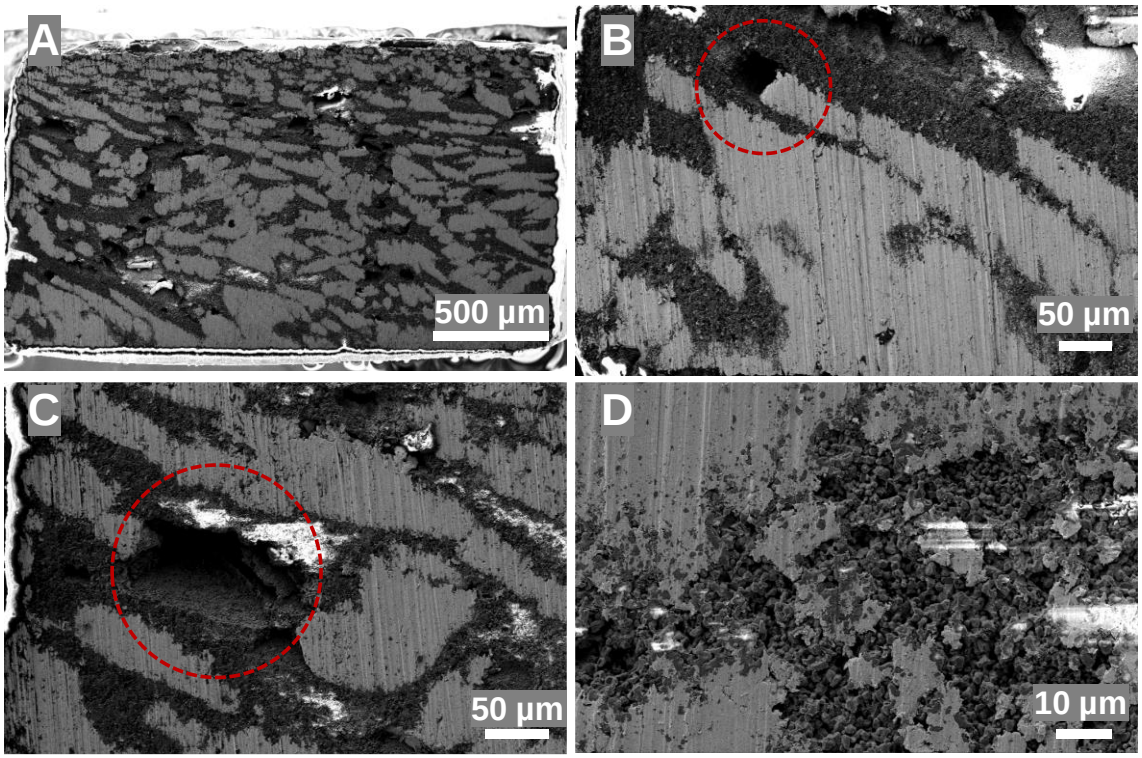

Figure 7-2 SEM imaging of the cross-section of a metal-ceramic beam. Bright regions are copper, and the dark areas are ceramic phase of the composite. (A) the cross-section view of the beam. (B – C) Shows the unfilled regions in the cross-section of the composite material. (D) The high magnification SEM image of the interface between metal and ceramic.

After the initial three-point bending experiment, the fractured surfaces of the beams were polished to obtain a flat surface. This polishing step was designed to simplify the healing process and analysis after the mechanical characterization of the healed beams. Figure 7-3 A shows two pieces of a beam after the initial three-point bending and polishing step facing each

other. Figure 7-3 B shows a side view of the pieces of a beam depicting the healing process. In the local healing process, electrodeposition technique is used. In this method by placing the damaged sample on a three-axis positioner that has a syringe loaded with a copper sulfate electrolyte and a copper mesh (to act as anode), an electrolyte droplet can be formed over the entire damaged region. The inset in Figure 7-3 B shows the droplet formed over the gap between the two pieces of the beam. Then, by connecting the conductive ends of the beams to the potentiostat the required circuit was formed. By applying a constant current, copper ions in the electrolyte will be pushed toward the conductive parts of the cross-section of the beams, which is the metal phase of the composite. Copper ions by accepting two electrons will be reduced to solid copper. This cycle will continue until the damaged region, which is the gap between two pieces of the beams (~0.2 mm) in these experiments, are filled entirely. After the healing process the overdeposited copper is gently polished. Figure 7-3 C shows the top, bottom, and side view of a healed beam. The healed region is marked using a white rectangle.

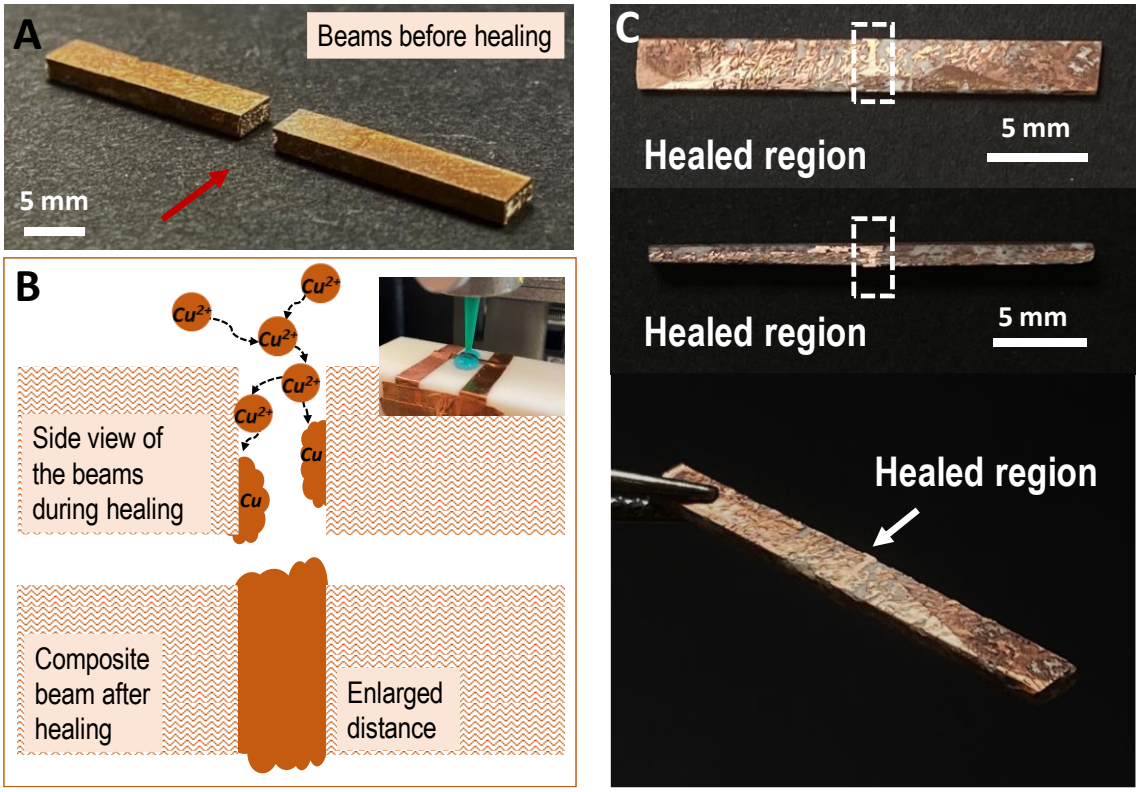

Figure 7-3 The healing process. (A) A composite beam after the three – point bending experiment. The fractured surfaces of the beam were polished to obtain flat surfaces. (B) The electrochemical healing via local healing technique where the copper sulfate electrolyte is locally formed over the fractured surfaces in order to complete the circuit for electrodeposition. (C) The top, side, and isometric view of the healed composite beam. The shiny narrow region in the middle of the beam is the electrodeposited metal that heals the beam.

It should be noted that a tensile experiment is preferable to extract interfacial properties of the healed composite. However, due to the challenges in gripping the samples, three-point bending experiments were used to evaluate the interfacial strength of the healed composite beams.

Four scenarios are predicted to evaluate the interfacial strength of the healed composite beams using the bending experiments (Figure 7-4). The first scenario is that the beam after the bending experiment breaks from the healed material, which is pure copper and leaves an

electrodeposited metal-metal interface. The second scenario is that the healed beam breaks at the interface between the electrodeposited copper (healing material) and the copper portion of the composite material. This failure is the preferred scenario to extract the interfacial strength of the healed beams. The third scenario is that the beam breaks at some point in the composite material. However, it is less probable to happen as the maximum bending moment is applied to the middle section of the beam where the healing was performed. The fourth scenario is that the beam breaks at a combination of electrodeposited metal-metal interface and the electrodeposited metal-composite interface.

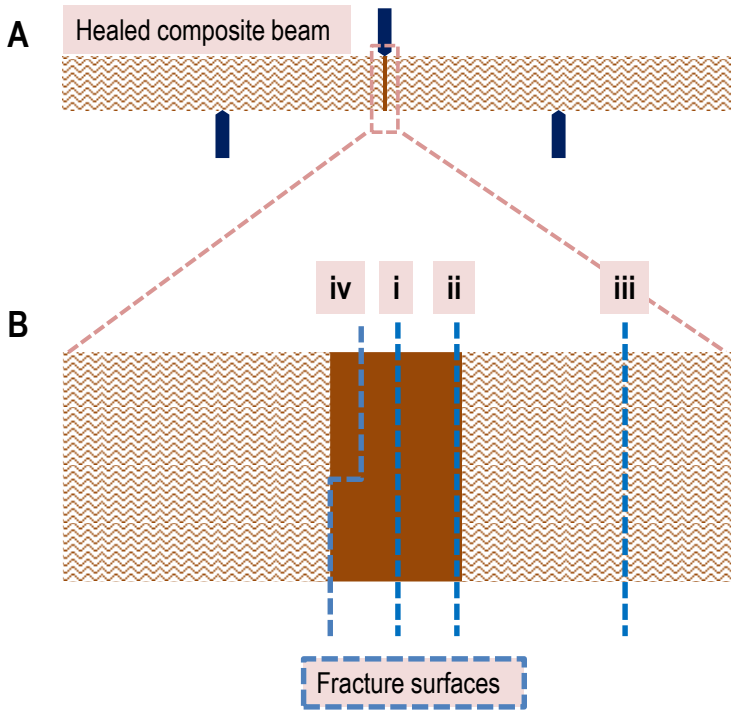

Figure 7-4 A Schematic representation of different scenarios of failure modes of the healed composite beam. (A) shows the beam under three-point bending fixture, (B) A zoomed-in view of the healed region where the failure could occur.

In the healing experiments a total number of seven samples were tested. Several observations were made. SEM images of the fractured surfaces were acquired after the bending experiments to further evaluate the scenarios. None of the samples were failed from the composite part of the beams. This was predictable as the healed region is in the middle of the beam and the maximum bending moment in the bending experiment is applied to the middle section of the beam. This was a good indication that the initial metal infiltration had a relatively good quality.

Figure 7-5 (A), (C) show the SEM images of the fractured surfaces of the two pieces of a healed beam after bending experiment from the cross-section view. The SEM images show that the beam was fractured from the healed material after the bending test. They show that the pieces of the beam have electrodeposited metal-metal interfaces. This case shows that the first scenario can occur. Four samples in the bending experiments of the healed beams had similar scenario. There might be several reasons for this behavior. First, a closer look onto the fractured surfaces was taken and found that several defects were present inside the healed region and on the edges of the healed area. These defects can contribute to the crack formation and propagation (Figure 7-5 B,D). It is speculated that the second possible reason for this performance can be the effect of the maximum bending moment acting at the middle section of the beam, which might cause failure in the middle section of the healed region. However, since the gap between two pieces of the beam, which is the width of the healed region (~0.2 mm), was not particularly large, the bending moment at the exact middle section of the beam and the interface between the metal and the composite was not considerably different to cause

the failure in the middle section of the beam. The other reason could be that the healing process starts with nucleation and growth of copper in the shape of small islands (Figure 7-5). These spherical islands will grow and merge at some point between the two pieces of the beam. It is suspected that there might be void formation where the copper islands reach to each other, which can be another reason for occurrence of this scenario. All three discussed reasons can contribute to the performance of the healed beams. The strength of the healed beams was calculated according to the bending equations provided in Materials and Methods section of this chapter and was 39.01 ± 5.2 MPa.

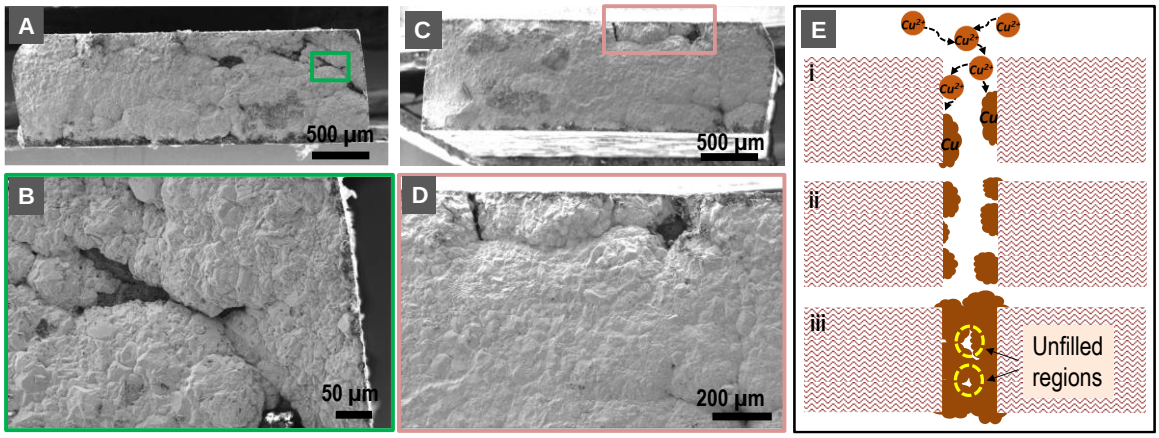

Figure 7-5 SEM images of the fractured surfaces of a representative healed beam after bending experiment. (A), (D) show the crsoss section view of the two pieces of the beam. (B-C) show the underfilled regions in the healed region of the left piece of the beam. (E-F) shows the defects in the healed region of the right piece of the beam.

Another observation was two beams that failed according to the fourth scenario in which the beam failed at a combination of the electrodeposited metal-metal interface, and electrodeposited metal-composite interface. Figure 7-6 show optical images of one such beam. Figure 7-6 (A), and (B) show the side views of the healed beam after bending experiment. Two sides of the beam were still attached together in regions under compression in bending test. The compression and tension surfaces of the beams are labeled in the images. From the side

views of the healed beam, two pores can be observed in the healed region. These pores were not fully filled during the healing process, which can contribute to the failure of the healed beam. Figure 7-6 (C), and (D) show the bottom surface of the beam, which was under tension and the top surface of the beam, which was under compression in the bending experiment. The image of the bottom surface of the beam shows that in the bending experiment dissociation of the healed part from the composite took place, however, the healed part also broke into two parts. This might happen due to the presence of two large voids in the healed region. The strength of the beams was 27.8 ± 8.5 MPa.

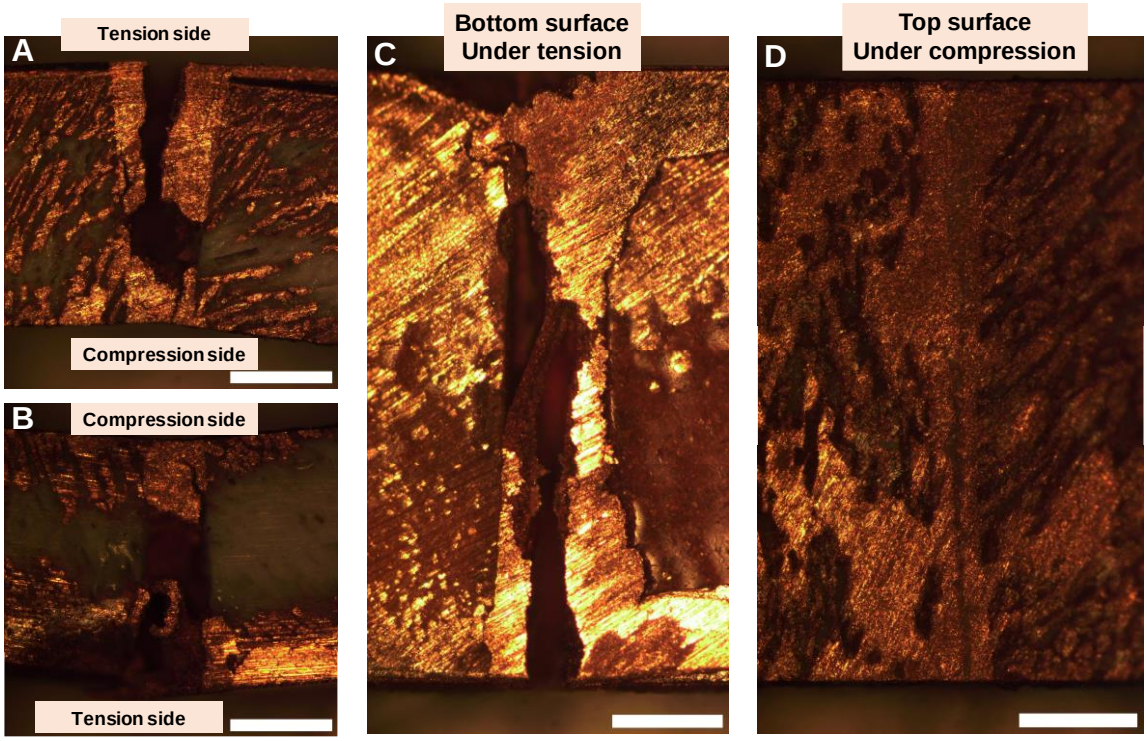

Figure 7-6 Optical images of a healed beam after the three-point bending experiment. The orange regions are copper. (A), (B) Side views of the beam. (C) Bottom surface of the beam, which was under tension in the bending experiment. (D) The top surface of the beam in the bending experiment, which was under compression.

Figure 7-7 (A) and (B) show the side views of a healed beam after bending experiment. The two pieces of the beams were attached to each other from the compression side of the

beam. The side view images show a void in the electrodeposited area, which was not filled completely. The other side view clearly shows the beam failed from the interface between the electrodeposited metal and the composite beam. Figure 7-7 (C) shows the top view of the healed beam after bending test. It shows a uniform deposition in the gap between the two pieces of the beam during the healing process.

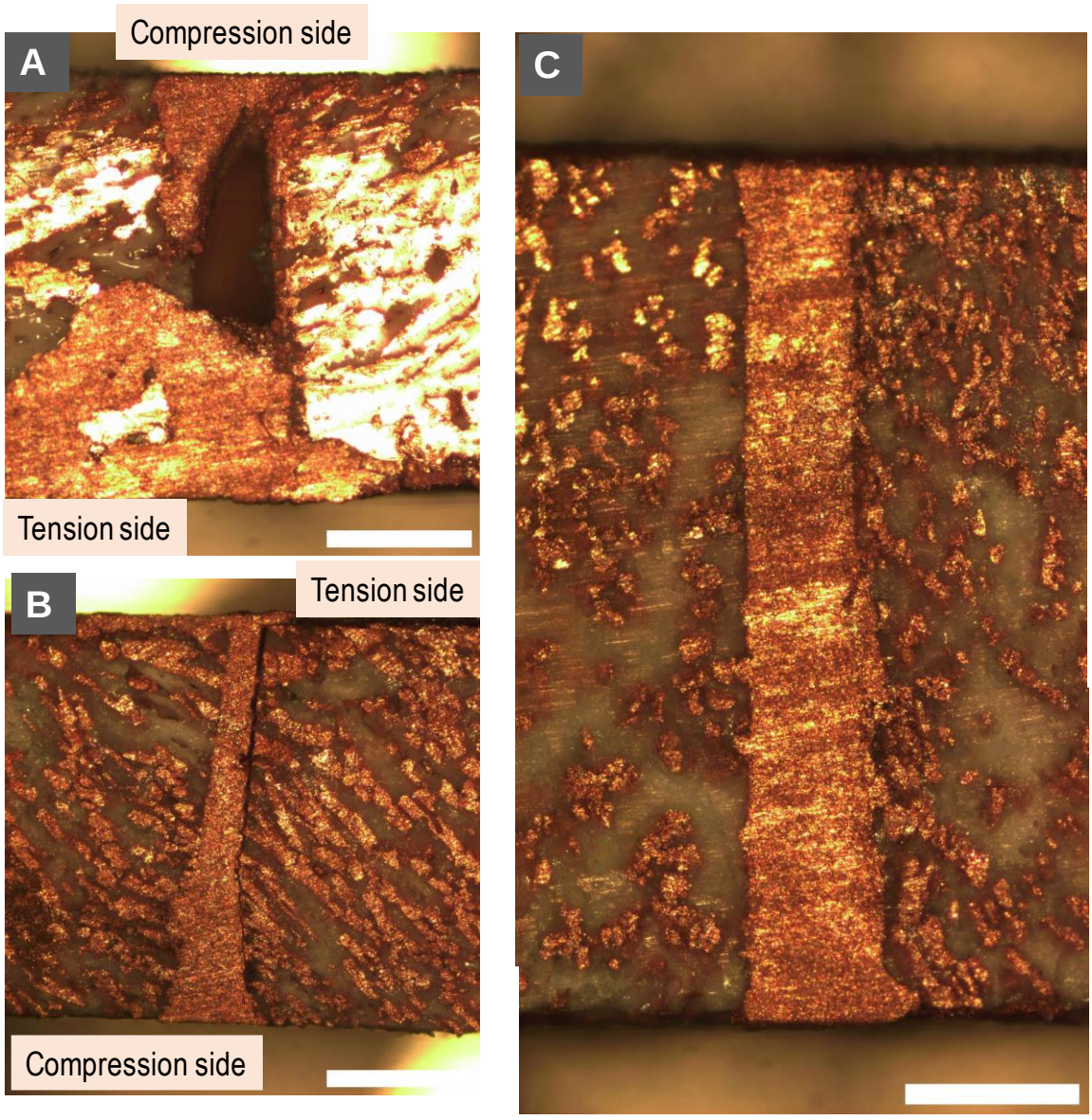

Figure 7-7 Optical images of the healed composite beam after three-point bending experiment. The orange regions are copper and the other regions (white to grey) is alumina. (A), (B) side views of the healed region in the beam. The tension and compression sides in the bending experiment are labeled in the images. (C) The top view of the healed beam after bending experiment. The entire surface is under compression. The scale bars are 500 microns.

To further investigate the failure of this sample, SEM images of the fractured surfaces were acquired. Figure 7-8 (A), (B) show the two pieces of the healed beam after bending test. SEM images show that the fracture happened from the interface between electrodeposited metal and the composite. A large void (the yellow circle in Figure 7-8 (B)) close to the neutral axis of the cross-section view of the fractured surface of the healed beam indicate that the electrodeposition parameters in the healing process should be optimized for a complete healing. The strength of the healed beam was calculated to ~ 10 MPa. Considering void presence in the healed region, it is estimated that the interfacial strength of the healed beam has a lower bound of 10 MPa.

By taking a closer look into the fractured surface of the beam, metal bridges in the composite are visible, which provide a continuous metallic phase in the composite material (Figure 7-8 (C), (D)). This continuous phase makes the composite conductive, which is essential for the healing process.

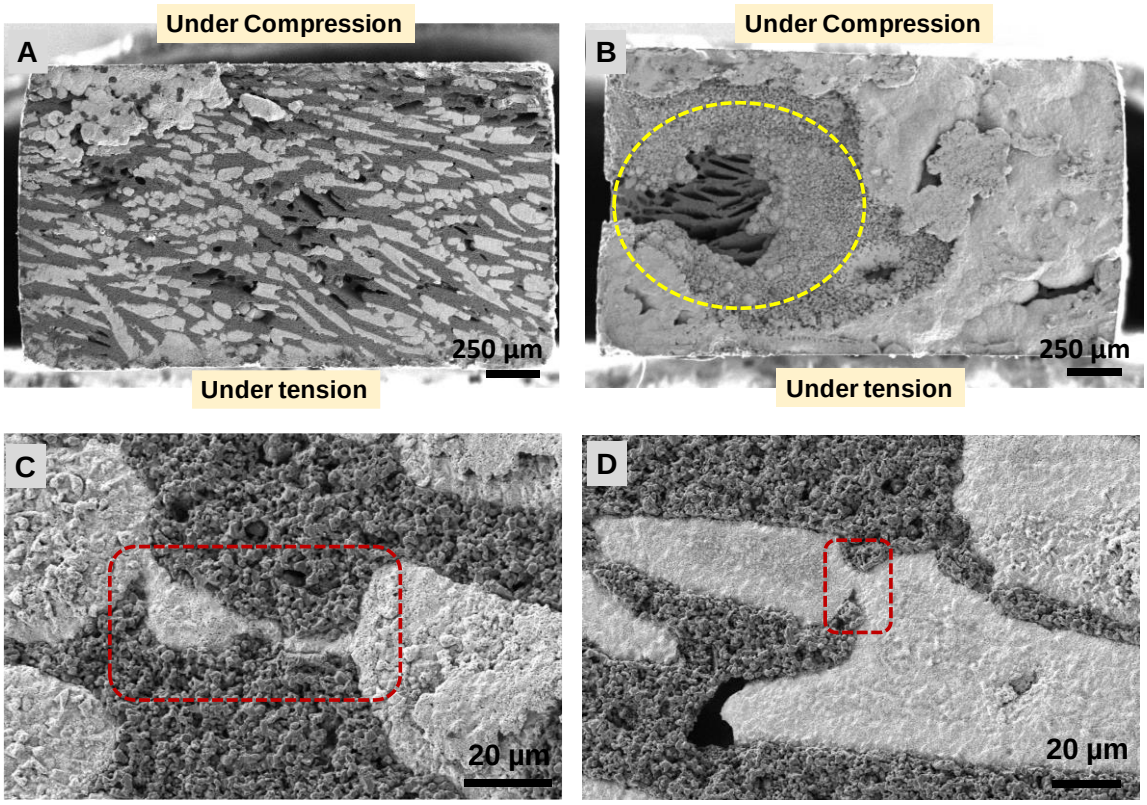

Figure 7-8 SEM images of the fractured surfaces of a healed beam after three-point bending expermint. (A) shows one piece of the beam. The fractured surface clearly shows that the smaple failed at the interface between the deposited copper and the copper in the composite. (B) shows the other piece of the beam after failure. The yellow circle shows a pore that was not filled during the healing experiment.

Another interesting observation in the experiments was the fractured regions in the metal component of the composite. Figure 7-9 (A) shows the metal-ceramic interface in the fractured surface of a healed beam after the bending experiment. Interestingly, the metal phase of the composite stretched in the tension surface of the beam during the bending test as it separated from the ceramic component of the composite and the electrodeposited metal (the healed region). The gap between the metal and ceramic in Figure 7-9 (B) is because of the stretched metal due to plastic deformation during bending. The ridges on the metal phase of the composite material and t the permanent deformation confirm the plastic deformation of the metal part of the composite during the bending experiment.

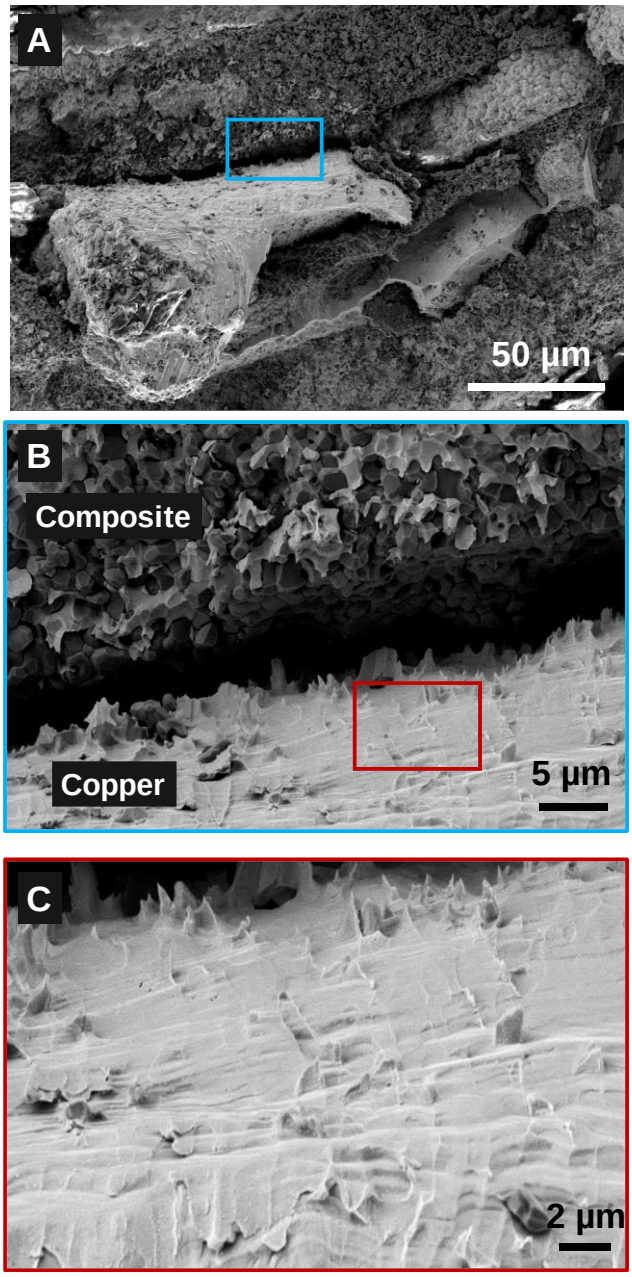

Figure 7-9 SEM images of the fractured surfaces of the healed composite beam after three-point bending experiment. Bright regions are metal and the dark areas are the ceramic phase of the composite material. (A), (B) Show the interface between the metal and the ceramic in the composite in the fractured surface of a beam. (C) The high magnification SEM image of the fractured metal shows the ridges that are caused by plastic deformation during stretching in the bending experiments.

To get more insights on the healed material, high magnification SEM images of the fractured surfaces were acquired. The bright regions in Figure 7-10 (A)-(C) are the

electrodeposited copper and the dark areas are the ceramic phase of the composite. The interface between the copper and the ceramic is mechanical interlocking.

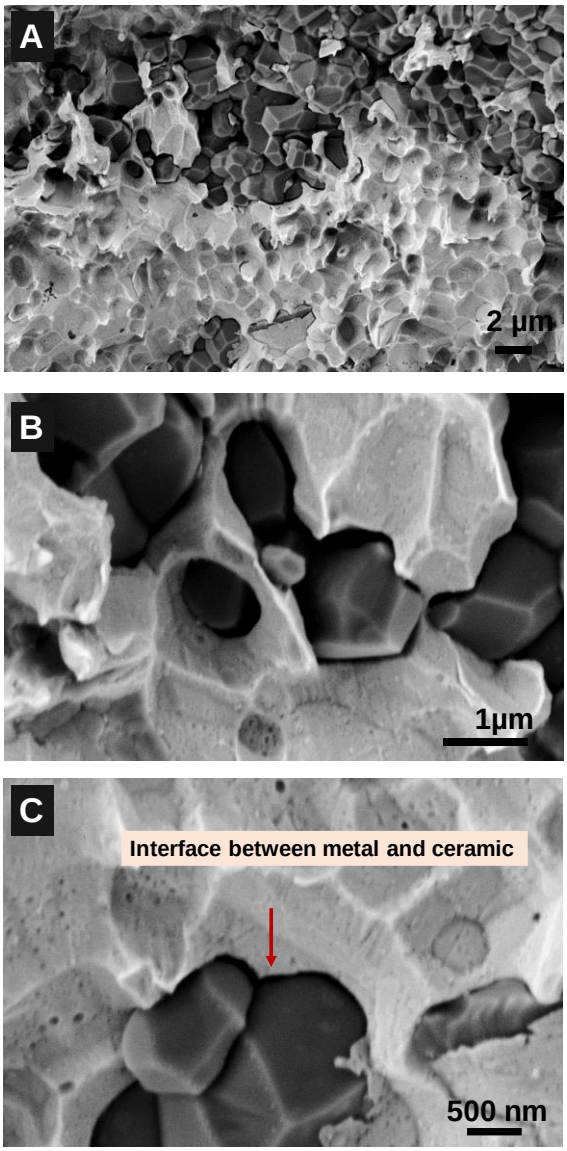

Figure 7-10 High magnification SEM images of the fractured surfaces at the interface of the healed metal and the composite. Dark regions are ceramic and the bright regions are metal. (A) shows the deposited metal in the cross section of the beam. (B) and (C) show the mechanical interlocking interface between metal and ceramic in the composite.

7.3 Conclusion

In this chapter, a systematic study was presented to investigate the interfacial properties of the healed composite using the local healing technique presented in chapter 5. A simplified three-point bending experiment was designed to extract the interfacial strength of the healed beam. Four failure scenarios were speculated and discussed. It can be concluded that although a high current density could lower the healing duration, it could also adversely affect the mechanical properties of the healed material. Additionally, presence of large voids in the healed region lowered the strength of the healed beams. Optimizing the electrodeposition parameters can prevent the formation of large voids in the healed region. To accurately measure the interfacial properties of the healed sample, a uniform electrodeposited material at a current density similar to the initial metal infiltration is needed.

8 OUTLOOK

In the chapters 2 to 4, a new process for additive manufacturing of ceramics using commercial polymer-derived ceramics was introduced and the printed parts were characterized. To better understand the surface quality of the printed ceramics more characterization such as XRD is recommended to examine the amorphous/crystalline interface between the printed ceramic and the thin coating that covers it. New support bath can be designed to ease the part removal from the bath and minimize the coating thickness. The printed part-bath interfacial properties can provide more insight on the overall process and the quality of the prints. By designing and building a larger 3D printer, large scale parts can be printed layer-by-layer. Incorporation of ceramic whiskers or fibres into the polymer derived ceramic can add to the functional properties of the printed part such as electromagnetic shielding.

In chapters 5 to 7, manufacturing of large porous alumina sheets by freeze casting on a thermoelectric cold plate was demonstrated and fabricated ceramic sheets were characterized mechanically. Additionally, a low-cost manufacturing technique was used to electrochemically infiltrate the porous ceramic with a metal. The electrochemical parameters in the metal infiltration process directly affect the quality of the metal. A systematic study on the electrochemical parameters can help in tuning the properties of the composite. A local healing process was introduced to heal the damaged composite by forming a droplet over the damaged region using a syringe mounted on a three-axis positioner. The healing setup can be automated by a syringe pump to continuously supply the electrolyte to the damaged region. This is a very crucial enhancement as the droplet evaporates slowly. The continuous deposition can result

in a more uniform material with less defects. Thus, it can improve mechanical properties of the fabricated composite.

The interfacial strength of the healed composite beams was characterized via bending experiments. However, the preferred method may be the tensile test. Since the process of making the porous ceramic is more scalable than before, larger ceramic sheets can be manufactured. By optimizing the electrochemical parameters, the sheets can be infiltrated in a reasonable time. Having large samples is important for tensile characterization as the small samples are not ideal because of gripping issues.

REFERENCES

[1] Z. Chen *et al.*, "3D printing of ceramics: A review," *J Eur Ceram Soc*, vol. 39, no. 4, pp. 661–687, 2019.

[2] A. Zocca, P. Colombo, C. M. Gomes, and J. Günster, "Additive manufacturing of ceramics: issues, potentialities, and opportunities," *Journal of the American Ceramic Society*, vol. 98, no. 7, pp. 1983–2001, 2015.

[3] M. L. Griffith and J. W. Halloran, "Freeform fabrication of ceramics via stereolithography," *Journal of the American Ceramic Society*, vol. 79, no. 10, pp. 2601–2608, 1996.

[4] T. Chartier, C. Chaput, F. Doreau, and M. Loiseau, "Stereolithography of structural complex ceramic parts," *J Mater Sci*, vol. 37, no. 15, pp. 3141–3147, 2002.

[5] X. Lv, F. Ye, L. Cheng, S. Fan, and Y. Liu, "Binder jetting of ceramics: Powders, binders, printing parameters, equipment, and post-treatment," *Ceram Int*, vol. 45, no. 10, pp. 12609–12624, 2019.

[6] P. Bertrand, F. Bayle, C. Combe, P. Gœuriot, and I. Smurov, "Ceramic components manufacturing by selective laser sintering," *Appl Surf Sci*, vol. 254, no. 4, pp. 989–992, 2007.

[7] K. Shahzad, J. Deckers, J.-P. Kruth, and J. Vleugels, "Additive manufacturing of alumina parts by indirect selective laser sintering and post processing," *J Mater Process Technol*, vol. 213, no. 9, pp. 1484–1494, 2013.

[8] G. Franchin, L. Wahl, and P. Colombo, "Direct ink writing of ceramic matrix composite structures," *Journal of the American Ceramic Society*, vol. 100, no. 10, pp. 4397–4401, 2017.

[9] P. Colombo, G. Mera, R. Riedel, and G. D. Soraru, "Polymer-derived ceramics: 40 years of research and innovation in advanced ceramics," *Journal of the American Ceramic Society*, vol. 93, no. 7, pp. 1805–1837, 2010.

[10] T. A. Pham, D. Kim, T. Lim, S. Park, D. Yang, and K. Lee, "Three-dimensional SiCN ceramic microstructures via nano-stereolithography of inorganic polymer photoresists," *Adv Funct Mater*, vol. 16, no. 9, pp. 1235–1241, 2006.

[11] S. Martínez-Crespiera, E. Ionescu, H.-J. Kleebe, and R. Riedel, "Pressureless synthesis of fully dense and crack-free SiOC bulk ceramics via photo-crosslinking and pyrolysis of a polysiloxane," *J Eur Ceram Soc*, vol. 31, no. 5, pp. 913–919, 2011.

[12] S. R. Shah and R. Raj, "Mechanical properties of a fully dense polymer derived ceramic made by a novel pressure casting process," *Acta Mater*, vol. 50, no. 16, pp. 4093–4103, 2002.

[13] E. Zanchetta *et al.*, "Stereolithography of SiOC ceramic microcomponents," *Advanced Materials*, vol. 28, no. 2, pp. 370–376, 2016.

[14] M. Schwentenwein and J. Homa, "Additive manufacturing of dense alumina ceramics," *Int J Appl Ceram Technol*, vol. 12, no. 1, pp. 1–7, 2015.

[15] Z. C. Eckel, C. Zhou, J. H. Martin, A. J. Jacobsen, W. B. Carter, and T. A. Schaedler, "Additive manufacturing of polymer-derived ceramics," *Science (1979)*, vol. 351, no. 6268, pp. 58–62, 2016.

[16] L. Brigo, J. E. M. Schmidt, A. Gandin, N. Michieli, P. Colombo, and G. Brusatin, "3D nanofabrication of SiOC ceramic structures," *Advanced Science*, vol. 5, no. 12, p. 1800937, 2018.

[17] T. J. Hinton *et al.*, "Three-dimensional printing of complex biological structures by freeform reversible embedding of suspended hydrogels," *Sci Adv*, vol. 1, no. 9, p. e1500758, 2015.

[18] C. S. O'Bryan *et al.*, "Self-assembled micro-organogels for 3D printing silicone structures," *Sci Adv*, vol. 3, no. 5, p. e1602800, 2017.

[19] T. Bhattacharjee *et al.*, "Writing in the granular gel medium," *Sci Adv*, vol. 1, no. 8, p. e1500655, 2015.

[20] D. A. Walker, J. L. Hedrick, and C. A. Mirkin, "Rapid, large-volume, thermally controlled 3D printing using a mobile liquid interface," *Science (1979)*, vol. 366, no. 6463, pp. 360–364, 2019.

[21] B. E. Kelly, I. Bhattacharya, H. Heidari, M. Shusteff, C. M. Spadaccini, and H. K. Taylor, "Volumetric additive manufacturing via tomographic reconstruction," *Science (1979)*, vol. 363, no. 6431, pp. 1075–1079, 2019.

[22] R. L. Truby and J. A. Lewis, "Printing soft matter in three dimensions," *Nature*, vol. 540, no. 7633, pp. 371–378, 2016.

[23] J. R. Tumbleston *et al.*, "Continuous liquid interface production of 3D objects," *Science (1979)*, vol. 347, no. 6228, pp. 1349–1352, 2015.

[24] M. P. de Beer, H. L. van der Laan, M. A. Cole, R. J. Whelan, M. A. Burns, and T. F. Scott, "Rapid, continuous additive manufacturing by volumetric polymerization inhibition patterning," *Sci Adv*, vol. 5, no. 1, p. eaau8723, 2019.

[25] M. Shusteff *et al.*, "One-step volumetric additive manufacturing of complex polymer structures," *Sci Adv*, vol. 3, no. 12, p. eaao5496, 2017.

[26] X. Kuang *et al.*, "Grayscale digital light processing 3D printing for highly functionally graded materials," *Sci Adv*, vol. 5, no. 5, p. eaav5790, 2019.

[27] S. Gantenbein, K. Masania, W. Woigk, J. P. W. Sesseg, T. A. Tervoort, and A. R. Studart, "Three-dimensional printing of hierarchical liquid-crystal-polymer structures," *Nature*, vol. 561, no. 7722, pp. 226–230, 2018.

[28] M. A. Skylar-Scott, J. Mueller, C. W. Visser, and J. A. Lewis, "Voxelated soft matter via multimaterial multinozzle 3D printing," *Nature*, vol. 575, no. 7782, pp. 330–335, 2019.

[29] I. D. Robertson *et al.*, "Rapid energy-efficient manufacturing of polymers and composites via frontal polymerization," *Nature*, vol. 557, no. 7704, pp. 223–227, 2018.

[30] B. G. Compton and J. A. Lewis, "3D-printing of lightweight cellular composites," *Advanced materials*, vol. 26, no. 34, pp. 5930–5935, 2014.

[31] J. U. Lind *et al.*, "Instrumented cardiac microphysiological devices via multimaterial three-dimensional printing," *Nat Mater*, vol. 16, no. 3, pp. 303–308, 2017.

[32] X. Mu *et al.*, "Porous polymeric materials by 3D printing of photocurable resin," *Mater Horiz*, vol. 4, no. 3, pp. 442–449, 2017.

[33] D. K. Patel, A. H. Sakhaei, M. Layani, B. Zhang, Q. Ge, and S. Magdassi, "Highly stretchable and UV curable elastomers for digital light processing based 3D printing," *Advanced Materials*, vol. 29, no. 15, p. 1606000, 2017.

[34] M. Zarek, M. Layani, I. Cooperstein, E. Sachyani, D. Cohn, and S. Magdassi, "3D printing of shape memory polymers for flexible electronic devices," *Advanced Materials*, vol. 28, no. 22, pp. 4449–4454, 2016.

[35] Q. Shi *et al.*, "Recyclable 3D printing of vitrimer epoxy," *Mater Horiz*, vol. 4, no. 4, pp. 598–607, 2017.

[36] H. A. Pierson *et al.*, "Mechanical properties of printed epoxy-carbon fiber composites," *Exp Mech*, vol. 59, no. 6, pp. 843–857, 2019.

[37] Z. Chen *et al.*, "3D printing of ceramics: A review," *J Eur Ceram Soc*, vol. 39, no. 4, pp. 661–687, 2019.

[38] A. Zocca, P. Colombo, C. M. Gomes, and J. Günster, "Additive manufacturing of ceramics: issues, potentialities, and opportunities," *Journal of the American Ceramic Society*, vol. 98, no. 7, pp. 1983–2001, 2015.

[39] M. L. Griffith and J. W. Halloran, "Freeform fabrication of ceramics via stereolithography," *Journal of the American Ceramic Society*, vol. 79, no. 10, pp. 2601–2608, 1996.

[40] T. Chartier, C. Chaput, F. Doreau, and M. Loiseau, "Stereolithography of structural complex ceramic parts," *J Mater Sci*, vol. 37, no. 15, pp. 3141–3147, 2002.

[41] X. Lv, F. Ye, L. Cheng, S. Fan, and Y. Liu, "Binder jetting of ceramics: Powders, binders, printing parameters, equipment, and post-treatment," *Ceram Int*, vol. 45, no. 10, pp. 12609–12624, 2019.

[42] P. Bertrand, F. Bayle, C. Combe, P. Gœuriot, and I. Smurov, "Ceramic components manufacturing by selective laser sintering," *Appl Surf Sci*, vol. 254, no. 4, pp. 989–992, 2007.

[43] K. Shahzad, J. Deckers, J.-P. Kruth, and J. Vleugels, "Additive manufacturing of alumina parts by indirect selective laser sintering and post processing," *J Mater Process Technol*, vol. 213, no. 9, pp. 1484–1494, 2013.

[44] G. Franchin, L. Wahl, and P. Colombo, "Direct ink writing of ceramic matrix composite structures," *Journal of the American Ceramic Society*, vol. 100, no. 10, pp. 4397–4401, 2017.

[45] P. Colombo, G. Mera, R. Riedel, and G. D. Soraru, "Polymer-derived ceramics: 40 years of research and innovation in advanced ceramics," *Journal of the American Ceramic Society*, vol. 93, no. 7, pp. 1805–1837, 2010.

[46] T. A. Pham, D. Kim, T. Lim, S. Park, D. Yang, and K. Lee, "Three-dimensional SiCN ceramic microstructures via nano-stereolithography of inorganic polymer photoresists," *Adv Funct Mater*, vol. 16, no. 9, pp. 1235–1241, 2006.

[47] S. Martínez-Crespiera, E. Ionescu, H.-J. Kleebe, and R. Riedel, "Pressureless synthesis of fully dense and crack-free SiOC bulk ceramics via photo-crosslinking and pyrolysis of a polysiloxane," *J Eur Ceram Soc*, vol. 31, no. 5, pp. 913–919, 2011.

[48] S. R. Shah and R. Raj, "Mechanical properties of a fully dense polymer derived ceramic made by a novel pressure casting process," *Acta Mater*, vol. 50, no. 16, pp. 4093–4103, 2002.

[49] M. Schwentenwein and J. Homa, "Additive manufacturing of dense alumina ceramics," *Int J Appl Ceram Technol*, vol. 12, no. 1, pp. 1–7, 2015.

[50] E. Zanchetta *et al.*, "Stereolithography of SiOC ceramic microcomponents," *Advanced Materials*, vol. 28, no. 2, pp. 370–376, 2016.

[51] Z. C. Eckel, C. Zhou, J. H. Martin, A. J. Jacobsen, W. B. Carter, and T. A. Schaedler, "Additive manufacturing of polymer-derived ceramics," *Science (1979)*, vol. 351, no. 6268, pp. 58–62, 2016.

[52] L. Brigo, J. E. M. Schmidt, A. Gandin, N. Michieli, P. Colombo, and G. Brusatin, "3D nanofabrication of SiOC ceramic structures," *Advanced Science*, vol. 5, no. 12, p. 1800937, 2018.

[53] X. Wang, F. Schmidt, D. Hanaor, P. H. Kamm, S. Li, and A. Gurlo, "Additive manufacturing of ceramics from preceramic polymers: A versatile stereolithographic approach assisted by thiol-ene click chemistry," *Addit Manuf*, vol. 27, pp. 80–90, 2019.

[54] M. Mahmoudi *et al.*, "Three-dimensional printing of ceramics through 'carving' a gel and 'filling in' the precursor polymer," *ACS Appl Mater Interfaces*, vol. 12, no. 28, pp. 31984–31991, 2020.

[55] K. Huang, H. Elsayed, G. Franchin, and P. Colombo, "Embedded direct ink writing of freeform ceramic components," *Appl Mater Today*, vol. 23, p. 101005, 2021.

[56] K. Huang, H. Elsayed, G. Franchin, and P. Colombo, "3D printing of polymer-derived SiOC with hierarchical and tunable porosity," *Addit Manuf*, vol. 36, p. 101549, 2020.

[57] J. W. Kemp, N. S. Hmeidat, and B. G. Compton, "Boron nitride-reinforced polysilazane-derived ceramic composites via direct-ink writing," *Journal of the American Ceramic Society*, vol. 103, no. 8, pp. 4043–4050, 2020.

[58] J. Li, K. Lu, T. Lin, and F. Shen, "Preparation of micro-/mesoporous SiOC bulk ceramics," *Journal of the American Ceramic Society*, vol. 98, no. 6, pp. 1753–1761, 2015.

[59] X. Guo, Y. Feng, X. Lin, Y. Liu, H. Gong, and Y. Zhang, "The dielectric and microwave absorption properties of polymer-derived SiCN ceramics," *J Eur Ceram Soc*, vol. 38, no. 4, pp. 1327–1333, 2018.

[60] Y. Li, Y. Yu, H. San, Y. Wang, and L. An, "Wireless passive polymer-derived SiCN ceramic sensor with integrated resonator/antenna," *Appl Phys Lett*, vol. 103, no. 16, p. 163505, 2013.

[61] R. Zhao, G. Shao, Y. Cao, L. An, and C. Xu, "Temperature sensor made of polymer-derived ceramics for high-temperature applications," *Sens Actuators A Phys*, vol. 219, pp. 58–64, 2014.

[62] G. Liu, J. Kaspar, L. M. Reinold, M. Graczyk-Zajac, and R. Riedel, "Electrochemical performance of DVB-modified SiOC and SiCN polymer-derived negative electrodes for lithium-ion batteries," *Electrochim Acta*, vol. 106, pp. 101–108, 2013.

[63] P. Jana, O. Santoliquido, A. Ortona, P. Colombo, and G. D. Sorarù, "Polymer-derived SiCN cellular structures from replica of 3D printed lattices," *Journal of the American Ceramic Society*, vol. 101, no. 7, pp. 2732–2738, 2018.

[64] R. Riedel, G. Mera, R. Hauser, and A. Klonczynski, "Silicon-based polymer-derived ceramics: synthesis properties and applications-a review dedicated to Prof. Dr. Fritz Aldinger on the occasion of his 65th birthday," *Journal of the Ceramic Society of Japan (日本セラミックス協会学術論文誌)*, vol. 114, no. 1330, pp. 425–444, 2006.

[65] R. J. Mondschein, A. Kanitkar, C. B. Williams, S. S. Verbridge, and T. E. Long, "Polymer structure-property requirements for stereolithographic 3D printing of soft tissue engineering scaffolds," *Biomaterials*, vol. 140, pp. 170–188, 2017.

[66] A. Kulkarni, J. Pearce, Y. Yang, A. Motta, and G. D. Sorarù, "SiOC (N) cellular structures with dense struts by integrating fused filament fabrication 3D printing with polymer-derived ceramics," *Adv Eng Mater*, vol. 23, no. 12, p. 2100535, 2021.

[67] A. Lavedrine *et al.*, "Pyrolysis of polyvinylsilazane precursors to silicon carbonitride," *J Eur Ceram Soc*, vol. 8, no. 4, pp. 221–227, 1991.

[68] E. Ionescu, H.-J. Kleebe, and R. Riedel, "Silicon-containing polymer-derived ceramic nanocomposites (PDC-NCs): Preparative approaches and properties," *Chem Soc Rev*, vol. 41, no. 15, pp. 5032–5052, 2012.

[69] G. S. Barroso, W. Krenkel, and G. Motz, "Low thermal conductivity coating system for application up to 1000 C by simple PDC processing with active and passive fillers," *J Eur Ceram Soc*, vol. 35, no. 12, pp. 3339–3348, 2015.

[70] P. Furtat, M. Lenz-Leite, E. Ionescu, R. A. F. Machado, and G. Motz, "Synthesis of fluorine-modified polysilazanes via Si–H bond activation and their application as protective hydrophobic coatings," *J Mater Chem A Mater*, vol. 5, no. 48, pp. 25509–25521, 2017.

[71] B. Santhosh, C. Vakifahmetoglu, E. Ionescu, A. Reitz, B. Albert, and G. D. Soraru, "Processing and thermal characterization of polymer derived SiCN (O) and SiOC reticulated foams," *Ceram Int*, vol. 46, no. 5, pp. 5594–5601, 2020.

[72] G. D. Sorarù, C. Tavonatti, L. Kundanati, N. Pugno, and M. Biesuz, "Effect of the pyrolysis atmosphere on the mechanical properties of polymer-derived SiOC and SiCN," *Journal of the American Ceramic Society*, vol. 103, no. 11, pp. 6519–6530, 2020.

[73] S. Wang and M. W. Urban, "Self-healing polymers," *Nat Rev Mater*, vol. 5, no. 8, pp. 562–583, 2020.

[74] B. J. Blaiszik, S. L. B. Kramer, S. C. Olugebefola, J. S. Moore, N. R. Sottos, and S. R. White, "Self-healing polymers and composites," *Annu Rev Mater Res*, vol. 40, pp. 179–211, 2010.

[75] F. Herbst, D. Döhler, P. Michael, and W. H. Binder, "Self-healing polymers via supramolecular forces," *Macromol Rapid Commun*, vol. 34, no. 3, pp. 203–220, 2013.

[76] Y.-L. Liu and T.-W. Chuo, "Self-healing polymers based on thermally reversible Diels–Alder chemistry," *Polym Chem*, vol. 4, no. 7, pp. 2194–2205, 2013.

[77] C. Chen *et al.*, "Self-healing of cracks in Ag joining layer for die-attachment in power devices," *Appl Phys Lett*, vol. 109, no. 9, p. 093503, 2016.

[78] I. M. van Meerbeek *et al.*, "Morphing metal and elastomer bicontinuous foams for reversible stiffness, shape memory, and self-healing soft machines," *Advanced Materials*, vol. 28, no. 14, pp. 2801–2806, 2016.

[79] H. Yu, X. Liu, X. Li, and A. Godbole, "Crack healing in a low-carbon steel under hot plastic deformation," *Metallurgical and Materials Transactions A*, vol. 45, no. 2, pp. 1001–1009, 2014.

[80] B. Grabowski and C. C. Tasan, "Self-healing metals," *Self-healing Materials*, pp. 387–407, 2016.

[81] J. B. Ferguson, B. F. Schultz, and P. K. Rohatgi, "Self-healing metals and metal matrix composites," *Jom*, vol. 66, no. 6, pp. 866–871, 2014.

[82] A. Hosoi, T. Nagahama, and Y. Ju, "Fatigue crack healing by a controlled high density electric current field," *Materials Science and Engineering: A*, vol. 533, pp. 38–42, 2012.

[83] Z. Hsain, Z. Jiang, and J. H. Pikul, "Enabling effective electrochemical healing of structural steel," *Multifunctional Materials*, vol. 4, no. 2, p. 024004, 2021.

[84] Z. Hsain and J. H. Pikul, "Low-energy room-temperature healing of cellular metals," *Adv Funct Mater*, vol. 29, no. 43, p. 1905631, 2019.

[85] Z. Xu *et al.*, "Bioinspired Nacre-Like Ceramic with Nickel Inclusions Fabricated by Electroless Plating and Spark Plasma Sintering," *Adv Eng Mater*, vol. 20, no. 5, p. 1700782, 2018.

[86] J. Huang, W. S. Rubink, H. Lide, T. W. Scharf, R. Banerjee, and M. Minary-Jolandan, "Alumina–Nickel Composite Processed via Co-Assembly Using Freeze-Casting and Spark Plasma Sintering," *Adv Eng Mater*, vol. 21, no. 3, p. 1801103, 2019.

[87] A. Gómez-Martín, M. P. Orihuela, J. A. Becerra, J. Martínez-Fernández, and J. Ramírez-Rico, "Permeability and mechanical integrity of porous biomorphic SiC ceramics for application as hot-gas filters," *Mater Des*, vol. 107, pp. 450–460, 2016.

[88] F. Zhang, Z. Li, M. Xu, S. Wang, N. Li, and J. Yang, "A review of 3D printed porous ceramics," *J Eur Ceram Soc*, 2022.

[89] Y. Chen, N. Wang, O. Ola, Y. Xia, and Y. Zhu, "Porous ceramics: Light in weight but heavy in energy and environment technologies," *Materials Science and Engineering: R: Reports*, vol. 143, p. 100589, 2021.

[90] E. C. Hammel, O.-R. Ighodaro, and O. I. Okoli, "Processing and properties of advanced porous ceramics: An application based review," *Ceram Int*, vol. 40, no. 10, pp. 15351–15370, 2014.

[91] J. Huang, S. Daryadel, and M. Minary-Jolandan, "Low-cost manufacturing of metal–ceramic composites through electrodeposition of metal into ceramic scaffold," *ACS Appl Mater Interfaces*, vol. 11, no. 4, pp. 4364–4372, 2019.

[92] S. Burlison and M. Minary-Jolandan, "Multiphysics simulation of microscale copper printing by confined electrodeposition using a nozzle array," *J Appl Phys*, vol. 131, no. 5, p. 055303, 2022.

[93] E. Poloni *et al.*, "Tough metal-ceramic composites with multifunctional nacre-like architecture," *Sci Rep*, vol. 11, no. 1, pp. 1–12, 2021.

[94] S. Morsali, D. Qian, and M. Minary-Jolandan, "Designing bioinspired brick-and-mortar composites using machine learning and statistical learning," *Commun Mater*, vol. 1, no. 1, pp. 1–11, 2020.

[95] H. Wan *et al.*, "Fabrication and characterisation of alumina/aluminium composite materials with a nacre-like micro-layered architecture," *Mater Des*, vol. 223, p. 111190, 2022.

[96] M. Kim, R. A. Franco, and B.-T. Lee, "Synthesis of functional gradient BCP/ZrO2 bone substitutes using ZrO2 and BCP nanopowders," *J Eur Ceram Soc*, vol. 31, no. 9, pp. 1541–1548, 2011.

[97] T. Ohji and M. Fukushima, "Macro-porous ceramics: processing and properties," *International Materials Reviews*, vol. 57, no. 2, pp. 115–131, 2012.

[98] L. Andersson and L. Bergström, "Gas-filled microspheres as an expandable sacrificial template for direct casting of complex-shaped macroporous ceramics," *J Eur Ceram Soc*, vol. 28, no. 15, pp. 2815–2821, 2008.

[99] B. Yuan, G. Wang, H. Li, L. Liu, Y. Liu, and Z. Shen, "Fabrication and microstructure of porous SiC ceramics with Al2O3 and CeO2 as sintering additives," *Ceram Int*, vol. 42, no. 11, pp. 12613–12616, 2016.

[100] A. Shimamura, M. Fukushima, M. Hotta, T. Ohji, and N. Kondo, "Fabrication and characterization of porous alumina with denser surface layer by direct foaming," *Journal of the Ceramic Society of Japan*, vol. 125, no. 1, pp. 7–11, 2017.

[101] S. Barg, C. Soltmann, M. Andrade, D. Koch, and G. Grathwohl, "Cellular ceramics by direct foaming of emulsified ceramic powder suspensions," *Journal of the American Ceramic Society*, vol. 91, no. 9, pp. 2823–2829, 2008.

[102] M. Fukushima and Y. Yoshizawa, "Fabrication and morphology control of highly porous mullite thermal insulators prepared by gelation freezing route," *J Eur Ceram Soc*, vol. 36, no. 12, pp. 2947–2953, 2016.

[103] S. Vijayan, R. Narasimman, and K. Prabhakaran, "Freeze gelcasting of hydrogenated vegetable oil-in-aqueous alumina slurry emulsions for the preparation of macroporous ceramics," *J Eur Ceram Soc*, vol. 34, no. 16, pp. 4347–4354, 2014.

[104] M. Naviroj, S. M. Miller, P. Colombo, and K. T. Faber, "Directionally aligned macroporous SiOC via freeze casting of preceramic polymers," *J Eur Ceram Soc*, vol. 35, no. 8, pp. 2225–2232, 2015.

[105] D. W. Richerson and W. E. Lee, *Modern ceramic engineering: properties, processing, and use in design*. CRC press, 2018.

[106] M. N. Rahaman, *Ceramic processing*. CRC press, 2017.

[107] R. J. Arsenault, S. Fishman, and M. Taya, "Deformation and fracture behavior of metal-ceramic matrix composite materials," *Prog Mater Sci*, vol. 38, pp. 1–157, 1994.

[108] A. Katz-Demyanetz, V. v Popov Jr, A. Kovalevsky, D. Safranchik, and A. Koptioug, "Powder-bed additive manufacturing for aerospace application: Techniques, metallic and metal/ceramic composite materials and trends," *Manuf Rev (Les Ulis)*, vol. 6, 2019.

[109] D. A. Snelling, C. B. Williams, C. T. A. Suchicital, and A. P. Druschitz, "Binder jetting advanced ceramics for metal-ceramic composite structures," *The International Journal of Advanced Manufacturing Technology*, vol. 92, no. 1, pp. 531–545, 2017.

[110] J. B. Ferguson, B. F. Schultz, and P. K. Rohatgi, "Self-healing metals and metal matrix composites," *Jom*, vol. 66, no. 6, pp. 866–871, 2014.

[111] B. Grabowski and C. C. Tasan, "Self-healing metals," *Self-healing materials*, pp. 387–407, 2016.

[112] H. Yu, X. Liu, X. Li, and A. Godbole, "Crack healing in a low-carbon steel under hot plastic deformation," *Metallurgical and Materials Transactions A*, vol. 45, no. 2, pp. 1001–1009, 2014.

[113] C. Chen *et al.*, "Self-healing of cracks in Ag joining layer for die-attachment in power devices," *Appl Phys Lett*, vol. 109, no. 9, p. 093503, 2016.

[114] I. M. van Meerbeek *et al.*, "Morphing metal and elastomer bicontinuous foams for reversible stiffness, shape memory, and self-healing soft machines," *Advanced Materials*, vol. 28, no. 14, pp. 2801–2806, 2016.

[115] Z. Hsain and J. H. Pikul, "Low-energy room-temperature healing of cellular metals," *Adv Funct Mater*, vol. 29, no. 43, p. 1905631, 2019.

[116] Z. Hsain, Z. Jiang, and J. H. Pikul, "Enabling effective electrochemical healing of structural steel," *Multifunctional Materials*, vol. 4, no. 2, p. 024004, 2021.

[117] J. Lindahl *et al.*, "Large-scale additive manufacturing with reactive polymers," Oak Ridge National Lab.(ORNL), Oak Ridge, TN (United States), 2018.

[118] C. S. O'Bryan *et al.*, "Three-dimensional printing with sacrificial materials for soft matter manufacturing," *MRS Bull*, vol. 42, no. 8, pp. 571–577, 2017.

[119] J. Li, K. Lu, T. Lin, and F. Shen, "Preparation of micro-/mesoporous SiOC bulk ceramics," *Journal of the American Ceramic Society*, vol. 98, no. 6, pp. 1753–1761, 2015.

[120] E. Ionescu, H.-J. Kleebe, and R. Riedel, "Silicon-containing polymer-derived ceramic nanocomposites (PDC-NCs): Preparative approaches and properties," *Chem Soc Rev*, vol. 41, no. 15, pp. 5032–5052, 2012.

[121] J. Li, K. Lu, T. Lin, and F. Shen, "Preparation of micro-/mesoporous SiOC bulk ceramics," *Journal of the American Ceramic Society*, vol. 98, no. 6, pp. 1753–1761, 2015.

[122] A. Kulkarni, G. D. Sorarù, and J. M. Pearce, "Polymer-derived SiOC replica of material extrusion-based 3-D printed plastics," *Addit Manuf*, vol. 32, p. 100988, 2020.

[123] H. Jiang, X.-H. Wang, W. Lei, G.-F. Fan, and W.-Z. Lu, "Effects of two-step sintering on thermal and mechanical properties of aluminum nitride ceramics by impedance spectroscopy analysis," *J Eur Ceram Soc*, vol. 39, no. 2–3, pp. 249–254, 2019.

[124] X. Tian, K. Yan, H. Liu, J. Zhao, and J. Yang, "Effect of Co on thermal and mechanical properties of Si3N4 based ceramic tool material," *Ceram Int*, vol. 45, no. 15, pp. 19435–19441, 2019.

[125] Q. Yuan, Z.-F. Chai, Z.-R. Huang, and Q. Huang, "A new precursor of liquid and curable polysiloxane for highly cost-efficient SiOC-based composites," *Ceram Int*, vol. 45, no. 6, pp. 7044–7048, 2019.

[126] American Society of Testing Material., "ASTM Standard Test Method for Flexural Strength of Advanced Ceramics at Ambient Temperature-Cylindrical Rod Strength," 2019.

[127] A. Standard, "C1239-00," *Standard Practice for Reporting Uniaxial Strength Data and Estimating Weibull Distribution Parameters for Advanced Ceramics*, vol. 15, 2002.

[128] A. Khalili and K. Kromp, "Statistical properties of Weibull estimators," *J Mater Sci*, vol. 26, no. 24, pp. 6741–6752, 1991.

[129] J. B. Quinn and G. D. Quinn, "A practical and systematic review of Weibull statistics for reporting strengths of dental materials," *dental materials*, vol. 26, no. 2, pp. 135–147, 2010.

[130] W. Wu, A. DeConinck, and J. A. Lewis, "Omnidirectional printing of 3D microvascular networks," *Advanced materials*, vol. 23, no. 24, pp. H178–H183, 2011.

[131] T. Bhattacharjee *et al.*, "Writing in the granular gel medium," *Sci Adv*, vol. 1, no. 8, p. e1500655, 2015.

[132] T. J. Hinton *et al.*, "Three-dimensional printing of complex biological structures by freeform reversible embedding of suspended hydrogels," *Sci Adv*, vol. 1, no. 9, p. e1500758, 2015.

[133] T. J. Hinton, A. Hudson, K. Pusch, A. Lee, and A. W. Feinberg, "3D printing PDMS elastomer in a hydrophilic support bath via freeform reversible embedding," *ACS Biomater Sci Eng*, vol. 2, no. 10, pp. 1781–1786, 2016.

[134] C. S. O'Bryan *et al.*, "Self-assembled micro-organogels for 3D printing silicone structures," *Sci Adv*, vol. 3, no. 5, p. e1602800, 2017.

[135] F. Afghah, M. Altunbek, C. Dikyol, and B. Koc, "Preparation and characterization of nanoclay-hydrogel composite support-bath for bioprinting of complex structures," *Sci Rep*, vol. 10, no. 1, pp. 1–13, 2020.

[136] K. Yang *et al.*, "Diels–Alder reversible thermoset 3D printing: Isotropic thermoset polymers via fused filament fabrication," *Adv Funct Mater*, vol. 27, no. 24, p. 1700318, 2017.

[137] A. Z. Nelson, B. Kundukad, W. K. Wong, S. A. Khan, and P. S. Doyle, "Embedded droplet printing in yield-stress fluids," *Proceedings of the National Academy of Sciences*, vol. 117, no. 11, pp. 5671–5679, 2020.

[138] J. N. Israelachvili, *Intermolecular and surface forces*. Academic press, 2011.

[139] A. Thom, "The flow past circular cylinders at low speeds," *Proceedings of the Royal Society of London. Series A, Containing Papers of a Mathematical and Physical Character*, vol. 141, no. 845, pp. 651–669, 1933.

[140] C. L. Cramer *et al.*, "Processing and properties of SiC composites made via binder jet 3D printing and infiltration and pyrolysis of preceramic polymer," *International Journal of Ceramic Engineering & Science*, vol. 2, no. 6, pp. 320–331, 2020.

[141] R. d'Elia, G. Dusserre, S. del Confetto, N. Eberling-Fux, C. Descamps, and T. Cutard, "Cure kinetics of a polysilazane system: Experimental characterization and numerical modelling," *Eur Polym J*, vol. 76, pp. 40–52, 2016.

[142] M. Mahmoudi, S. R. Burlison, S. Moreno, and M. Minary-Jolandan, "Additive-free and support-free 3D printing of thermosetting polymers with isotropic mechanical properties," *ACS Appl Mater Interfaces*, vol. 13, no. 4, pp. 5529–5538, 2021.

[143] G. Barroso, T. Kraus, U. Degenhardt, M. Scheffler, and G. Motz, "Functional coatings based on preceramic polymers," *Adv Eng Mater*, vol. 18, no. 5, pp. 746–753, 2016.

[144] A. Zambotti *et al.*, "Synthesis and thermal evolution of polysilazane-derived SiCN (O) aerogels with variable C content stable at 1600 C," *Ceram Int*, vol. 47, no. 6, pp. 8035–8043, 2021.

[145] H. Kleebe, D. Suttor, H. Müller, and G. Ziegler, "decomposition-crystallization of polymer-derived Si-C-N ceramics," *Journal of the American Ceramic Society*, vol. 81, no. 11, pp. 2971–2977, 1998.

[146] J. Huang, S. Daryadel, and M. Minary-Jolandan, "Low-cost manufacturing of metal–ceramic composites through electrodeposition of metal into ceramic scaffold," *ACS Appl Mater Interfaces*, vol. 11, no. 4, pp. 4364–4372, 2019.

[147] J. Hay, P. Agee, and E. Herbert, "Continuous stiffness measurement during instrumented indentation testing," *Exp Tech*, vol. 34, no. 3, pp. 86–94, 2010.

[148] H. Bai, Y. Chen, B. Delattre, A. P. Tomsia, and R. O. Ritchie, "Bioinspired large-scale aligned porous materials assembled with dual temperature gradients," *Sci Adv*, vol. 1, no. 11, p. e1500849, 2015.

[149] S.-Y. Chang and T.-K. Chang, "Grain size effect on nanomechanical properties and deformation behavior of copper under nanoindentation test," *J Appl Phys*, vol. 101, no. 3, p. 033507, 2007.

[150] M. F. Riyad, M. Mahmoudi, and M. Minary-Jolandan, "Manufacturing and Thermal Shock Characterization of Porous Yttria Stabilized Zirconia for Hydrogen Energy Systems," *Ceramics*, vol. 5, no. 3, pp. 472–483, 2022.